2014

Microstructural Analysis and Micromechanical Modeling of Flow Behaviour of Dual Phase Steels Using a Representative Volume Element Method

Maedeh Amirmaleki
University of Windsor

Microstructural Analysis and Micromechanical Modeling of Flow Behaviour of Dual Phase Steels Using a Representative Volume Element Method

By

Maedeh Amirmaleki

A Thesis
Submitted to the Faculty of Graduate Studies
through Mechanical, Automotive and Materials Engineering
in Partial Fulfillment of the Requirements for
the Degree of Master of Applied Science
at the University of Windsor

Windsor, Ontario, Canada
2014

Microstructural Analysis and Micromechanical Modeling of Flow Behaviour of Dual Phase Steels Using a Representative Volume Element Method

By

Maedeh Amirmaleki

APPROVED BY:

_____

Dr. D.O. Northwood
Mechanical, Automotive, & Materials Engineering

_____

Dr. V. Stoilov
Mechanical, Automotive, & Materials Engineering

_____

Dr. D. Green, Advisor
Mechanical, Automotive, & Materials Engineering

December 16, 2014

Author's Declaration of Originality

I hereby certify that I am the sole author of this thesis and that no part of this thesis has been published or submitted for publication.

I certify that, to the best of my knowledge, my thesis does not infringe upon anyone's copyright nor violate any proprietary rights and that any ideas, techniques, quotations, or any other material from the work of other people included in my thesis, published or otherwise, are fully acknowledged in accordance with the standard referencing practices. Furthermore, to the extent that I have included copyrighted material that surpasses the bounds of fair dealing within the meaning of the Canada Copyright Act, I certify that I have obtained a written permission from the copyright owner(s) to include such material(s) in my thesis and have included copies of such copyright clearances to my appendix.

I declare that this is a true copy of my thesis, including any final revisions, as approved by my thesis committee and the Graduate Studies office, and that this thesis has not been submitted for a higher degree to any other University or Institution.

Abstract

Micromechanical modeling of flow curves of DP500 and DP600 steels in uniaxial tension was carried out using the representative volume element (RVE) method. Digimat and ABAQUS software were coupled and used to provide the required RVE model parameters and to perform simulations. Modeling results were validated using the experimental flow curves of the steels. It was found that the flow curve of DP500 steel was accurately predicted from the onset of plastic deformation up to the onset of necking. In case of DP600 steel, the numerical flow curve accurately predicted the experimental flow curve of steel after 0.07 strain up to necking strain. The RVE size of 12.7x12.7x12.7 μm and 7.9x7.9x7.9 μm containing 26 martensite islands were found as the optimum RVE sizes for DP500 and DP600 steel, respectively. A mesh of C3D4 elements having a size of 0.050 μm was found to be the optimum element type and mesh size.

Table of Contents

List of Tables

List of Figures

List of Appendices

Appendix A

Calculation of the flow behaviour of ferrite, martensite and bainite in DP500 and DP600 steels is presented in the following. Results are used in Section 4.1.

List of Symbols

$\%C_{ss}^{f}$	carbon content of ferrite that made solid solution
$\%C_{ss}^{m}$	carbon content of martensite that made solid solution
$\%RA$	Relative Accuracy percent
b	Burgers vector
C	solute concentration in solid
d	grain size
F	Force
F_M	RVE deformation field
k_y	constant in the Hall-Petch equation
L	dislocation mean free path
M	Taylor factor
M_S	martensite start temperature
N	number of measured grains
$\vec{N}$	normal to initial RVE boundaries
$\vec{n}$	normal to current RVE boundaries
P_M	Piola-Kirchhoff stress tensor
s	standard deviation
V_0	volume of undeformed RVE
V_f	volume fraction of ferrite
V_m	volume fraction of martensite
$\vec{X}$	initial position vector of RVE
$\vec{x}$	actual position vector of RVE
Γ	current RVE boundaries
Γ_0	initial RVE boundaries
γ	shear strain
$\Delta\sigma_c$	contribution of carbon solid solution hardening in flow stress
ε	true strain

$\bar{\varepsilon}$	von Mises effective strain
μ	shear modulus
ρ	dislocation density
σ_0	friction stress opposing the movement of dislocations
σ_f	flow stress
σ_m	Cauchy stress
σ_{sss}	flow stress associated with solid solution strengthening
σ_y	yield strength
τ	critical resolved shear stress

1 Introduction

1.1 Motivations for Dual Phase Steels

Most of the current passenger vehicles operate on fossil fuels which tend to create economic and ecological challenges. One way to decrease fuel consumption is to reduce vehicle weight and this can be done by using stronger and thinner sheets in the vehicle body so as not to compromise passenger safety. Reducing the thickness of body parts and simultaneously preserving occupant safety requires a grade of sheet metal with an excellent combination of strength and formability such as dual phase steels.

As is shown in Figure 1-1, dual phase steels cover wide ranges of elongation and strength which means that there are grades of dual phase steels with varying combinations of strength and formability which can be used for different automotive body. The designation of dual phase steels includes a prefix DP as an abbreviation for dual phase and a number which represents the ultimate tensile strength of the steel. For instance, DP600 steel is a type of dual phase steel with an ultimate tensile strength that is at least 600 MPa. DP500, DP600, DP780 and DP980 are the more common industrial grades of dual phase steels.

With their superior and wide range of combination of strength and ductility, dual phase steels have gradually increased in market share. For instance, as is shown in Figure 1-2, According to World Auto Steel's Future Steel Vehicle (FSV) program, more than 30% of the future electric and hybrid vehicle bodies is expected to be made from three grades of dual phase steel.

In addition to a superior combination of strength and ductility, dual phase steels have attracted attention in the sheet metal forming industry due to their specific characteristics such as continuous yielding, low yield to tensile strength ratio, high initial work hardening rate and remarkably high uniform tensile elongation.

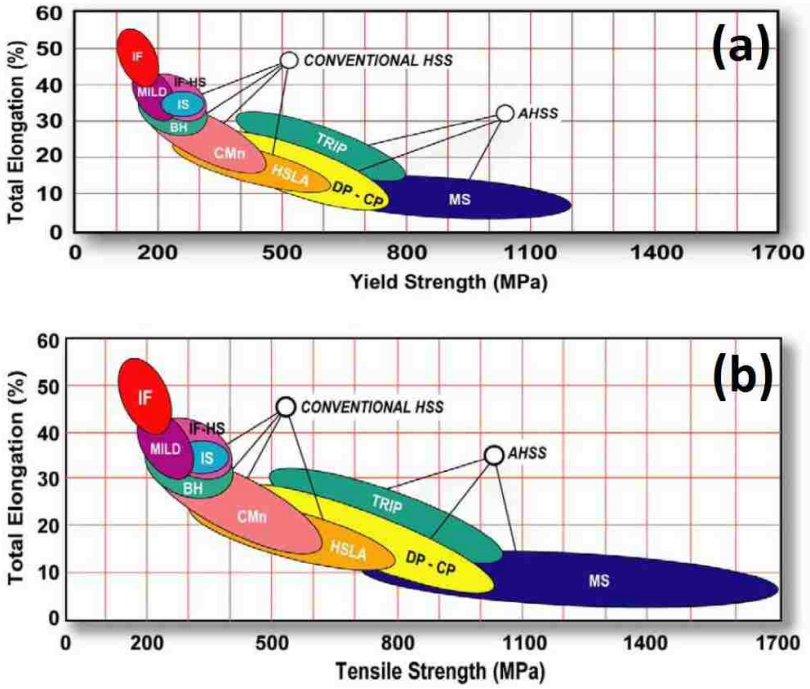

Figure 1-1 Total elongation of different steels as a function of (a) yield strength and (b) ultimate tensile strength. HSS: high strength steel; AHSS: advanced high strength steel; IF: interstitial free; BH: bake hardened; HSLA: high strength low alloy; TRIP: transformation-induced plasticity; DP: dual phase; MS: martensitic steel. [1]

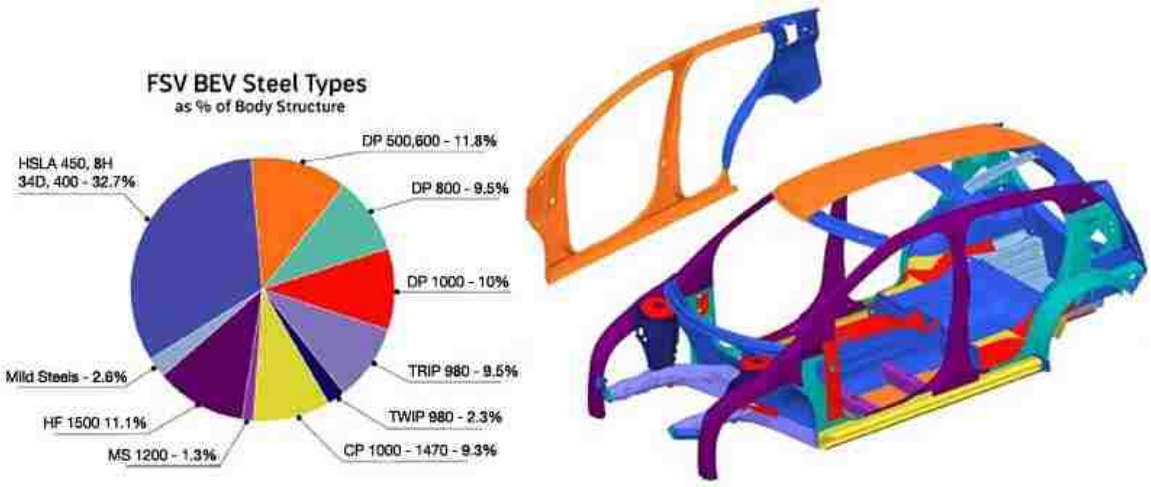

Figure 1-2 Application of different types of steel in the 2015-2020 electric and hybrid vehicles as indicated in the World Auto Steel's Future Steel Vehicle (FSV) program [2]

1.2 Micromechanical Modeling of Flow Behaviour

Microstructural parameters have a significant influence on the flow behaviour of materials; however, microstructural features are not considered in phenomenological finite element (FE) modeling of materials. To investigate the influence of microstructural features on flow behaviour, microstructure-based finite element models are developed. These models are known as micromechanical models.

In all mechanical modeling, elastic and plastic parameters such as Young's modulus, Poisson's ratio, yield stress, hardening modulus and hardening exponent are considered. In micromechanical models, chemical composition and volume fraction of phases, grain size and dislocation-based parameters are also taken into account. Hence, micromechanical models are able to predict the effects of solid solution hardening, grain size refinement and dislocations on the strength and ductility of sheet metal.

As it is shown in Figure 1-3, depending on the goal, modeling can be carried out at different scales. Micromechanical modeling of the flow curve can be carried both at a micro and macro-scale. It means that in micromechanical modeling, there is a bridge to relate the micro and macro scale flow behaviour of material. The micromechanical modeling technique that is used in this research is based on the representative volume element (RVE) method which is described in Section 2.4.

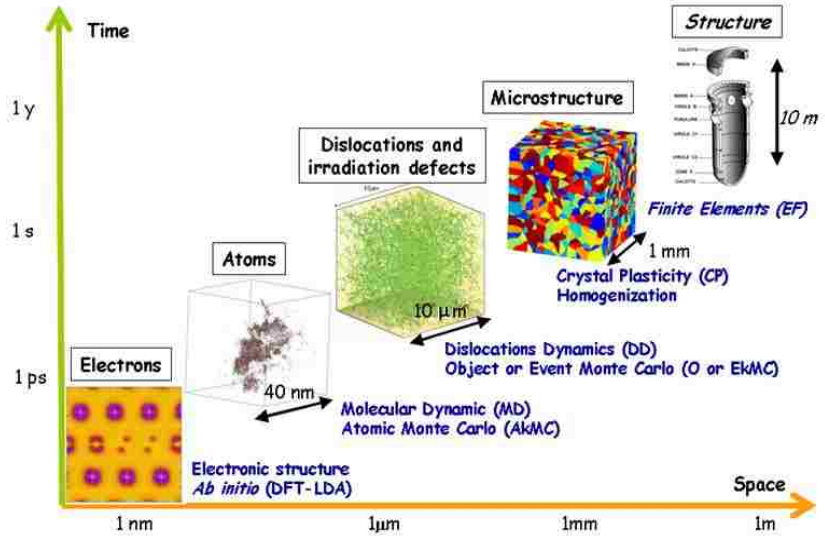

Figure 1-3 Different scales of characterization and modeling of materials [3]

1.3 Objective of the Research

The objective of this research is to predict the flow behaviour of DP500 and DP600 dual phase steels using a micromechanical model. The representative volume element (RVE) method was used for micromechanical modeling. Microstructural materials parameters such as chemical composition, volume fraction and morphology of phases as well as effects of modeling parameters including RVE and mesh size and element type have been investigated in this research.

1.4 Structure of the Dissertation

A brief description of the contents of each chapter is presented in the following:

Chapter 2 presents a literature review on the processing, strengthening mechanisms and flow behaviour of dual phase steels. Also, fundamentals of micromechanical modeling using the RVE method and the key points of micromechanical modeling of dual phase steels are described in this chapter. Finally, there is a brief review of the Digimat software which was used for micromechanical modeling.

Chapter 3 describes characterization of as-received DP500 and DP600 steel sheets including quantitative metallography, chemical analysis, flow behaviour and analysis of voids in the microstructure of deformed specimens.

Chapter 4 exhibits the general procedure that was used in this thesis for micromechanical modeling of dual phase steels using the RVE method.

Chapter 5 includes the results of this research and discusses the merits of this work. The numerical flow curves that were obtained for DP500 and DP600 steels are compared with the corresponding experimental flow curves. Also, influences of the RVE size and mesh size on the numerical results are discussed in this chapter.

Chapter 6 presents the conclusions and recommendations for future work.

2 Literature Survey

2.1 Introduction to Dual Phase Steels

Dual phase steels were introduced in the 1960s [4] and started to be used in the manufacturing industry in the 1970s. Their greater combination of strength and ductility compared to conventional steels encouraged the industries to support research on processing and microstructure-properties relationship of dual phase steels. The microstructure of dual phase steels consists of ferrite as the soft matrix and martensite as the hard phase, and small amounts of bainite may also be present. Ferrite and martensite are responsible for plastic deformation and strengthening of dual phase steels, respectively.

Commercial dual phase steels are produced by an intercritical annealing heat treatment in the (α + Υ) region of the iron-cementite phase diagram followed by rapid quenching to room temperature. Quenching must be sufficiently fast to avoid the diffusion and formation of other structures such as pearlite and bainite. However, in bainite-assisted dual phase steel, the steel is quenched to a certain temperature, an isothermal heat treatment is carried out to form bainite and a second rapid quench cools the steel to room temperature. The martensite volume fraction varies in different grades of dual phase steel. For instance, as it is shown in Figure 2-1, the martensite fraction in a typical DP500 and DP780 steel is approximately 10 vol% and 20 vol%, respectively; however, in a DP980 steel, the volume fraction of martensite is more than 30 vol% in order to provide sufficient strength to the steel. The martensite content in dual phase steels determines the intercritical annealing temperature. According to the lever rule, greater amounts of austenite are formed at higher intercritical annealing temperatures which transforms to martensite by rapid quenching.

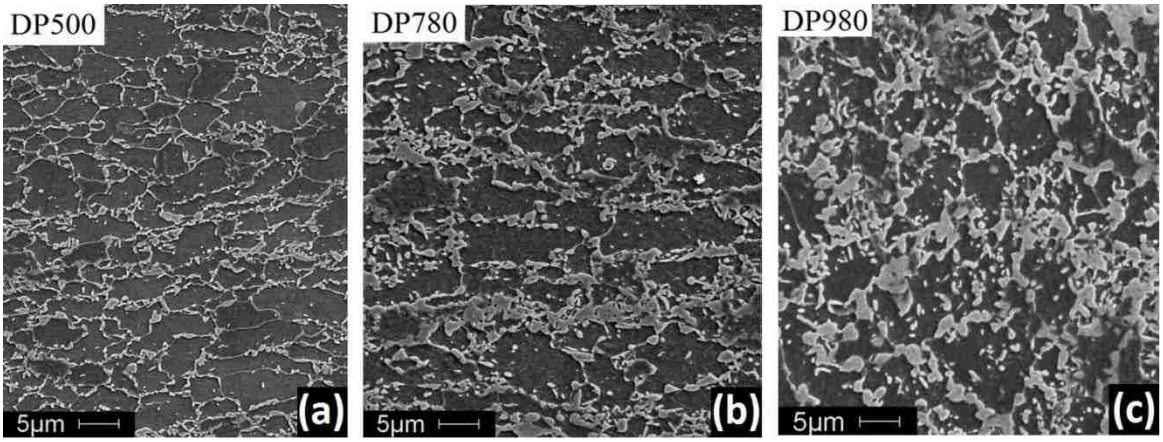

Figure 2-1 Microstructure of (a) DP500, (b) DP780 and (c) DP980 steels including ferrite grains (dark matrix) and martensite (bright phase) [5].

During processing of dual phase steels, different alloying elements are used in solid solution to increase the strength and hardness of the steel. Silicon, manganese, chromium, and molybdenum are the typical alloying elements in dual phase steels. Silicon affects the chemical composition of austenite by accelerating the migration of carbon atoms from the ferrite to the austenite during intercritical annealing [6]. Manganese is used to enhance hardenability of dual phase steels [7]. Chromium and molybdenum reduce the critical cooling rate of austenite for martensitic transformation [8,9]. Other elements such as vanadium and titanium may be added to form carbide and nitride precipitates that can increase the strength of the steel by precipitation hardening [10]. These precipitates limit the movement of the ferrite-austenite interface during quenching and enhance the martensite formation [11].

2.2 Strengthening Mechanisms in Dual Phase Steels

The microstructure of commercial dual phase steels includes ferrite and martensite. Depending on the heat treatment cycle, it may also include same bainite. The influence of strengthening mechanisms in ferrite, martensite and bainite on the flow stress of dual phase steels is discussed in the following.

2.2.1 Ferrite

Ferrite is the interstitial solid solution of carbon in body centered cubic (BCC) iron. It is the predominant phase in most low carbon steels including high strength low alloy steels (HSLA) and dual phase steels (DP). The ferrite grain size has a significant influence on the yield strength of dual phase steels. The influence of grain size on yield strength is described by the Hall-Petch relationship which was successively developed by Hall [12] and then Petch [13]:

$$\sigma_y = \sigma_0 + k_y d^{-1/2} \qquad 2\text{-}1$$

where d is the grain diameter, σ_y is the yield stress, σ_0 is the friction stress opposing the movement of dislocations in the grains and k_y is a constant. The mean ferrite grain size in advanced dual phase steels is reduced to less than 10 μm which remarkably enhances the flow stress.

Solid solution hardening is another strengthening mechanism that enhances the flow stress of ferrite. In dual phase steels, manganese is the dominant alloying element which has a notable influence on strengthening of the steel. Solid solution strengthening depends on the solute concentration as follows [14]:

$$\sigma_{sss} = kc^n \qquad 2\text{-}2$$

where c is the solute concentration, k is a constant, and $0.5<n<0.67$.

2.2.2 Martensite

During processing of dual phase steels, the steel is quenched from the intercritical annealing temperature to room temperature. During this heat treatment, the intercritical austenite transforms to martensite by a diffusionless phase transformation. The mechanical strength of martensite primarily depends on its carbon content [14][15]. The dependence of martensite hardness on the carbon content of the steel is shown in Figure 2-2. Also, Figure 2-3 presents the yield strength of martensite as a function of martensite carbon content. Similar to ferrite, solid solution hardening is a strengthening mechanism in martensite [14].

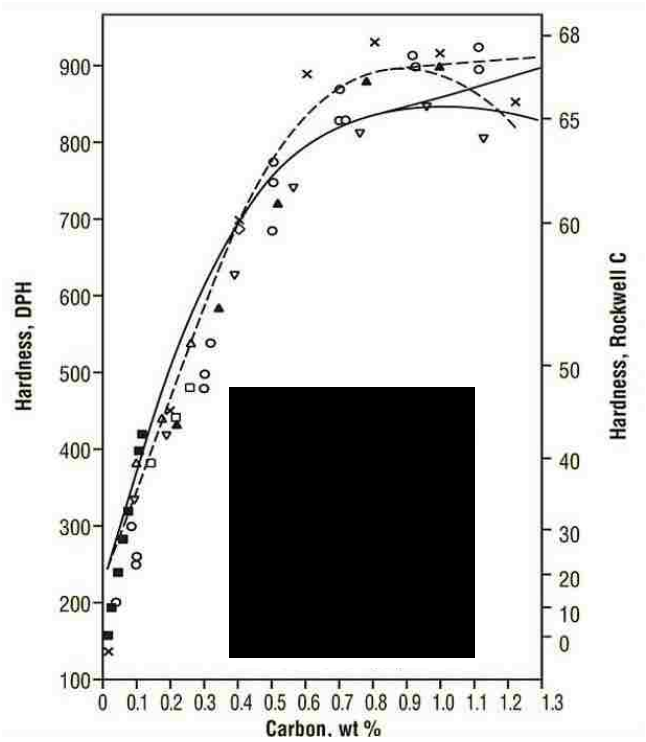

Figure 2-2 Hardness of martensitic steel as a function of carbon content [16]

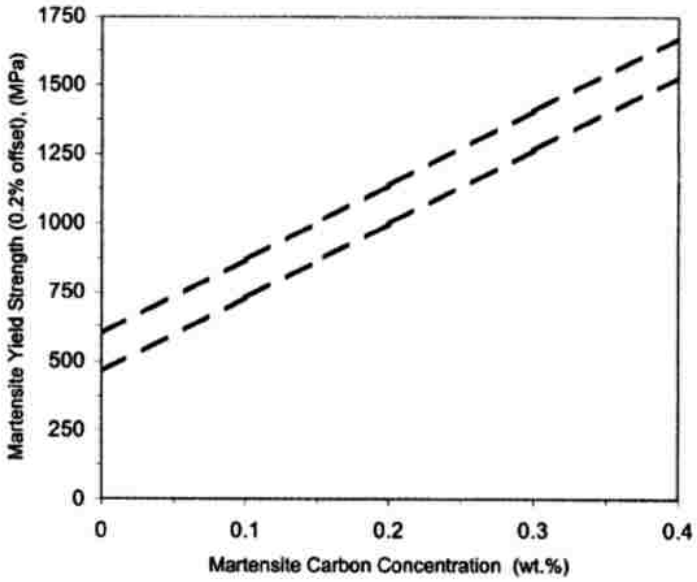

Figure 2-3 Dependence of martensite yield strength on martensite carbon content [17]

The mechanical properties of dual phase steels significantly depend on the volume fraction [18–22] and morphology [20–22] of martensite. The combination of strength and

ductility of dual phase steels improves with a finer dispersion of martensite islands rather than a coarse, banded or laminated martensite in the microstructure [20,23].

Martensite strength has a crucial role in the strengthening of dual phase steels. Since the martensite phase is a hard phase, the external loads are transferred to the martensite from the soft ferrite matrix. Hence, by increasing the volume fraction of martensite the yield and ultimate tensile strengths of dual phase steel increase [24]; however, it was reported that 55 vol% of martensite resulted in the greatest strength but beyond that a strength reduction was observed [20]. This behaviour is explained by the decreasing carbon content of martensite when its volume fraction increases which leads to softening of the martensite. Dependency of martensite strength on the martensite carbon content was described by square-root [25] and cube-root [26] equations; however, it has also been simply described by a linear equation by several authors [17,21,27]. In dual phase steels with a high-carbon martensite phase, under external loading, the martensite remains elastic and only the ferrite phase deforms plastically; therefore, the steel deformation is more comparable to that of alloys that are hardened with ultra-high strength particles [17].

2.2.3 Bainite

As it is shown in Figure 2-4, bainite forms by decomposition of austenite at a temperature above the martensite start temperature (M_s) and below the pearlite formation temperature. As it is presented in Figure 2-5, bainite is a combination of plate-shaped ferrite and carbides. Bainite is presented in two forms: lower-bainite and upper-bainite. Lower-bainite forms at temperatures closer to the M_s while upper-bainite forms at higher temperatures. The difference between upper and lower bainite occurs due to the dependence of the diffusion rate of carbon on the temperature at which bainite is forming. At higher temperatures, carbon diffuses faster from the newly formed ferrite to the residual austenite between the ferritic plates and forms large carbides. At low temperatures, diffusion of carbon is slower; hence, carbides precipitate inside the ferrite grains before they can leave the ferrite. Bainite with a fine non-lamellar structure usually

consists of cementite and dislocation-rich ferrite. The strength of this ferrite with high concentration of dislocations is greater than that of ordinary ferrite. The hardness of bainite is between that of pearlite and martensite [28].

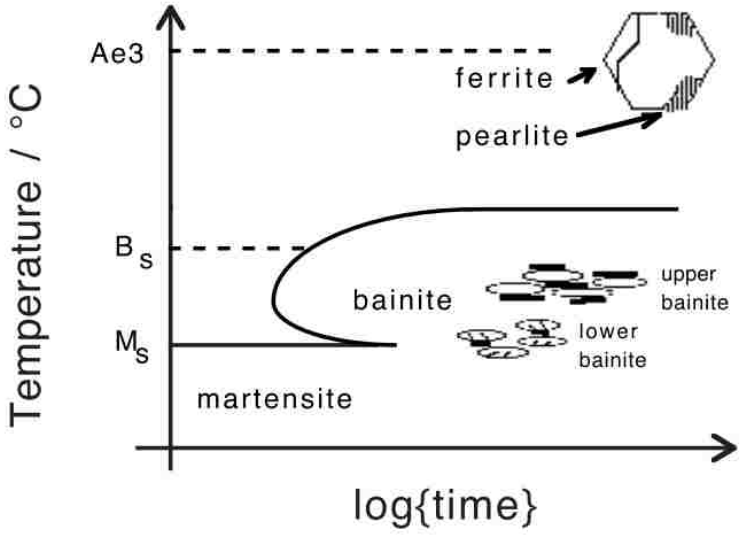

Figure 2-4 Schematic temperature-time-transformation (TTT) diagram showing the different domains of transformations in steel [29]

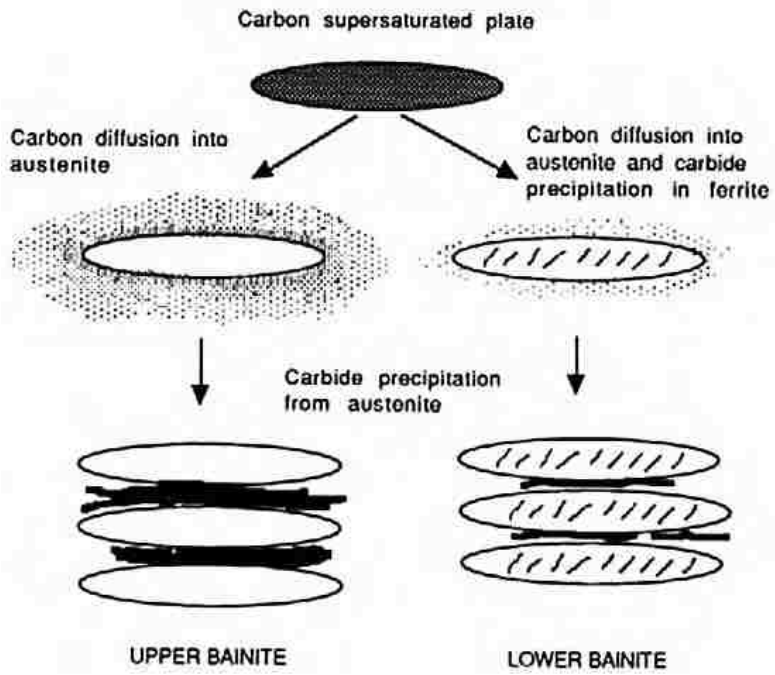

Figure 2-5 Schematic diagram of the formation of upper and lower bainite [30]

2.3 Yielding and Work Hardening Behaviour of Dual Phase Steels

The yield point is the stress at which a material begins to deform plastically. As is shown in Figure 2-6, low carbon steels generally exhibit yield point elongation. The yield point phenomenon includes upper and lower yield points in the tensile stress-strain curve followed with oscillations of the flow stress. In low carbon steels, dislocations are locked by the interstitial carbon atoms. The shear stress required to cause dislocation movement inside the grain is less than the shear stress necessary to unlock them, and this causes a sharp drop in stress at the yield point. The following oscillations, known as Lüders bands, continue until there are sufficient mobile dislocations to start continuous work hardening.

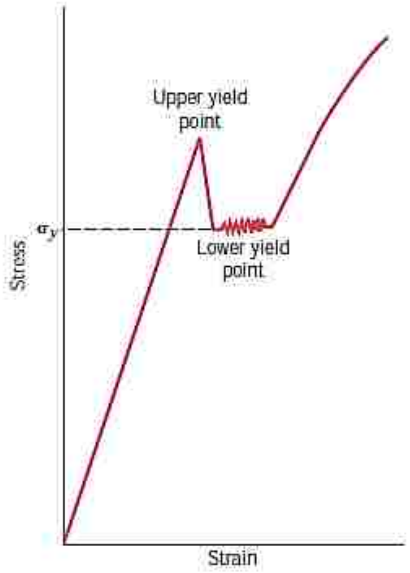

Figure 2-6 Schematic presentation of yield point phenomenon in low carbon steels

As it is shown in Figure 2-7(a), the yield point phenomenon is not usually observed in dual phase steels and the flow curves of dual phase steels exhibit continuous yielding due to the processing of dual phase steels. Austenite and martensite have face centered cubic (FCC) and body centered tetragonal (BCT) crystal structures, respectively. Hence, a volume expansion occurs during the austenite to martensite phase transformation [31]. This volume expansion introduces plastic deformation and therefore, as it is shown in Figure 2-7(b), new dislocations are generated at the ferrite/martensite interface. By

increasing the volume fraction of martensite the number of the newly generated dislocations increases. These dislocations are not locked by the interstitial carbon atoms. Hence, at the yield point, they can move immediately thus producing to make a smooth flow curve.

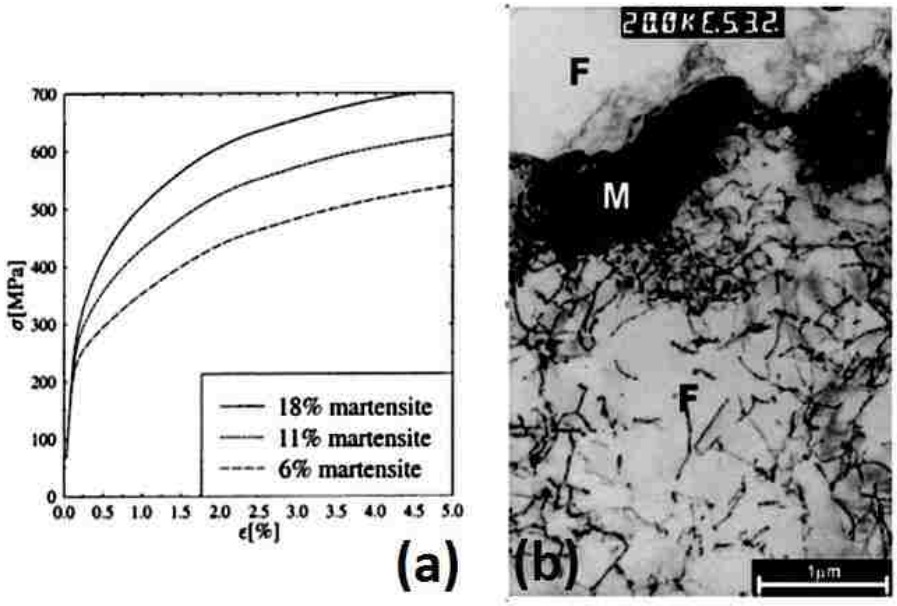

Figure 2-7 (a) Continuous yield behaviour in dual phase steels and (b) mobile dislocations at the ferrite/martensite interface in dual phase steels [32]

Work hardening, also known as strain hardening, is the strengthening of metals by plastic deformation. This strengthening occurs due to the movement and generation of dislocations within the crystal structure. Work hardening starts in materials after yielding occurs. Figure 2-8 shows that work hardening in dual phase steels significantly depends on the volume fraction of martensite. The work hardening rate is reported to be greater in dual phase steels with finer martensite islands [33].

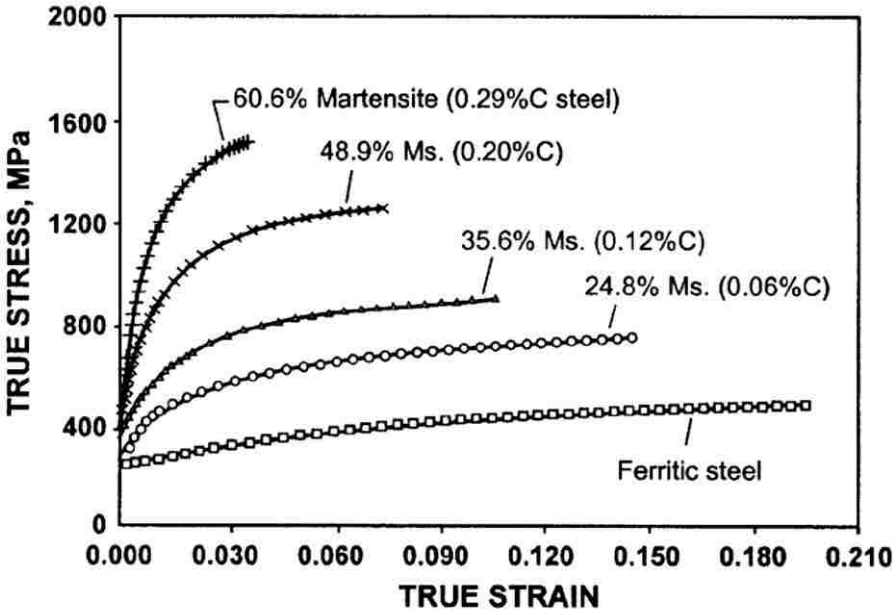

Figure 2-8 True stress-strain curve of a ferrite-martensite steel with 1.5 wt% Mn and different carbon contents annealed at 760 °C [34]

2.4 Micromechanical Modeling Using the Representative Volume Element Method

In the micromechanical modeling, the microstructural features of a material are presented in a finite element (FE) model through a representative volume element (RVE). An RVE is a small volume of microstructure that has the general characteristics of the whole microstructure and over which modeling of specific characteristics is carried out. The results of the RVE modeling investigations should properly describe the characteristics of the whole microstructure. As presented in Figure 2-9, micromechanical modeling of flow behaviour of a material using the RVE method consists of four steps. These steps are described in Sections 2.4.1 to 2.4.4.

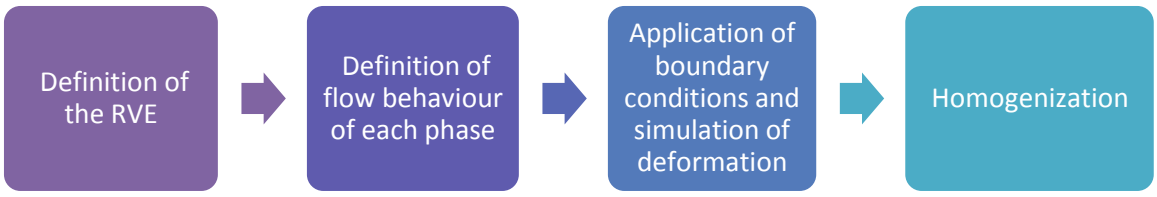

Figure 2-9 Four steps of micromechanical modeling of flow behaviour using the RVE method

2.4.1 Definition of the RVE

The RVE-based micromechanical modeling technique is an approach to predict the mechanical behaviour of materials using their microstructural features. An RVE is a small volume of microstructure which is able to adequately represent the essential features of the whole microstructure. It is expected that the RVE modeling method is able to represent the overall macroscopic behaviour of the material which means that the RVE acts as a bridge between the micro-scale and macro-scale properties of material.

A suitable RVE will have an average the same microstructural parameters as the overall microstructure, such as volume fraction, morphology and randomness of the phases. Hence, an RVE should be sufficiently large to include the essential microstructural characteristics. On the other hand, the RVE size should be as small as possible so that the states of stress and strain can be approximately considered as homogeneous in the whole RVE. Also, a smaller RVE requires less computational resources such as computer memory and calculation time to simulate the deformation. An advantage of micromechanical modeling using the RVE method is that the RVE provides a detailed description of the stress and strain distributions and their evolution in the microstructure during a metal forming process [35–37].

A basic RVE can be defined using a simple cell model or it can be more complicated by using a real microstructure. The RVE can also be defined in two dimensions (2D) or three dimensions (3D). Al-Abbasi carried out micromechanical modeling of dual phase steels using 2D and 3D cell models as the RVEs [38]. Figure 2-10 shows three cell models that were used by Al-Abbasi. He considered the martensite phase as circles and spheres in the 2D and 3D RVEs, respectively. The size of the circles and spheres in each cell was determined according to the martensite volume fraction in the dual phase steel.

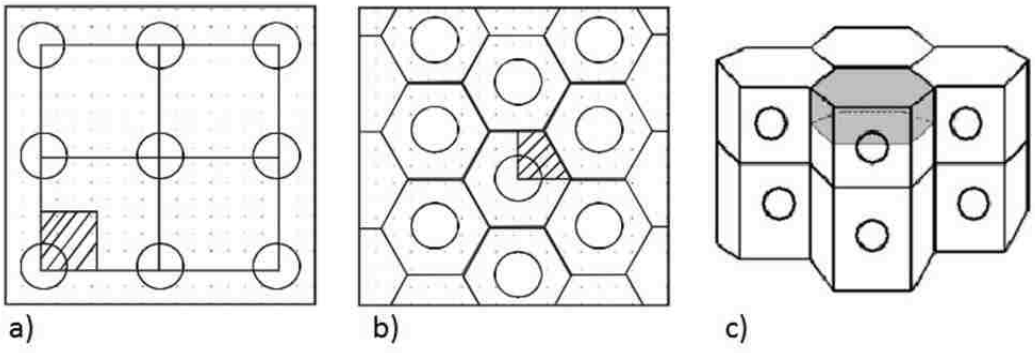

Figure 2-10 Two-dimensional cell models: (a) square array, (b) stacked hexagonal array and (c) three-dimensional array of stacked hexagonal cylinders [38].

2D and 3D RVEs can also be generated based on real microstructures. In the case of dual phase steels, martensite and ferrite can be clearly distinguished due to the color contrast between ferrite grains and martensite islands in a micrograph. The images from the actual microstructure, with two different colors for ferrite and martensite, can be converted to a 2D RVE model using different digitizing techniques. The digitized image is then discretized in preparation for the FE simulation of the deformation process. Some examples of 2D RVEs based on real microstructures that were generated by Uthaisangsuk et al [35], Paul [39] and Ramazani et al [40] are presented in Figure 2-11.

The simplest assumption for generating a 3D RVE of a two phase material is based on Mori–Tanaka's approach [41]. In this approach, the second phase particles are considered as inclusions that are distributed in a matrix representing the first phase. As can be seen in Figure 2-12, Uthaisangsuk et al [35], Paul [39] and Ramazani et al [40] generated cubic RVEs of dual phase steels. They considered ferrite as the matrix and martensite as inclusions. The numbers of ferrite and martensite cubes were determined according to their volume fraction in the dual phase steels.

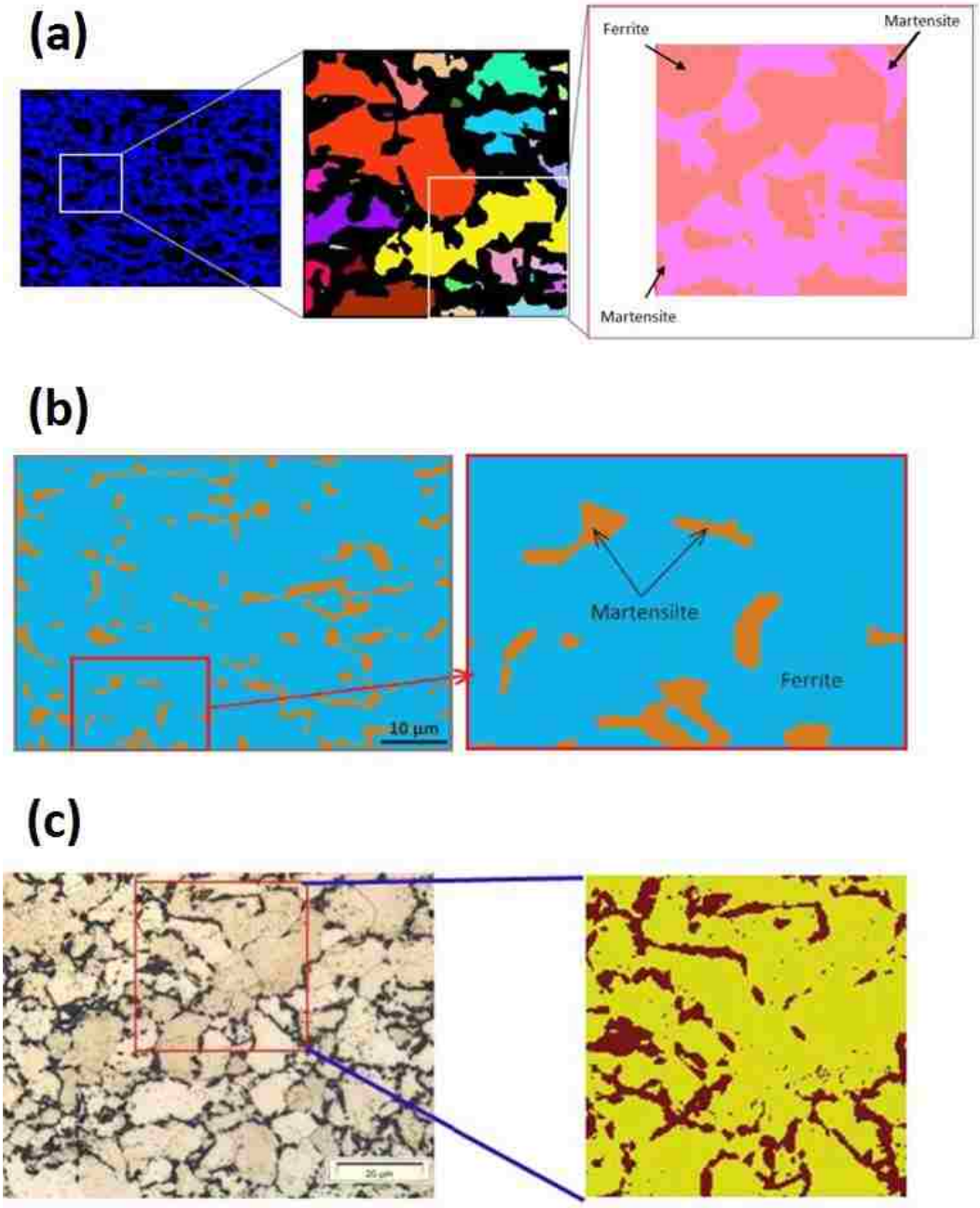

Figure 2-11 2D RVEs based on real microstructures generated by (a) Uthaisangsuk et al [35], (b) Paul [39] and (c) Ramazani et al [40].

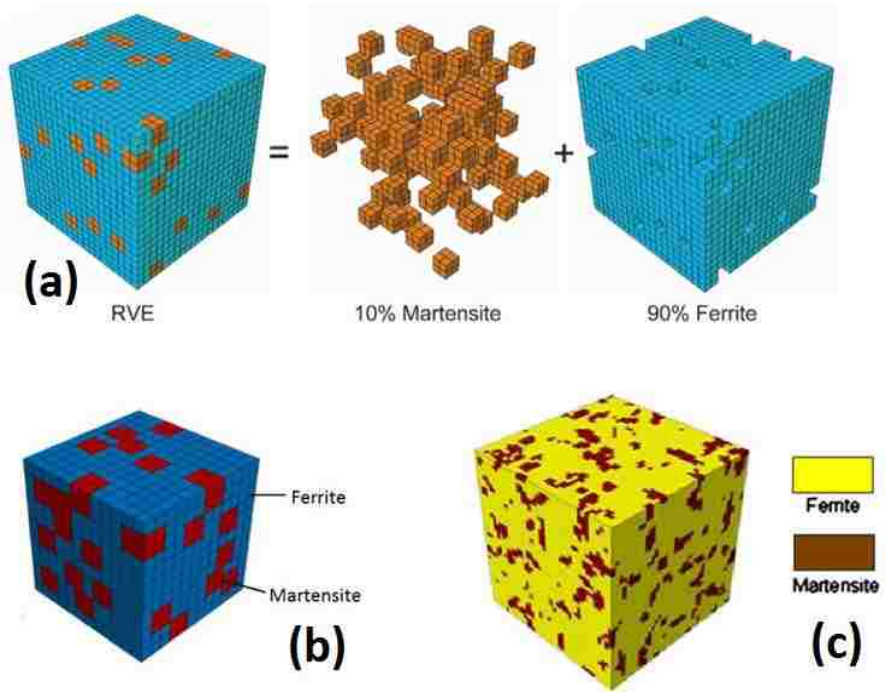

Figure 2-12 3D RVEs based on real microstructures generated by (a) Uthaisangsuk et al [35], (b) Paul [39] and (c) Ramazani et al [40]

The 3D RVEs that were just mentioned were generated by different researchers based on simplified microstructural features; however, Lewis et al [42] and Brands et al [43] produced 3D RVEs using the real microstructures as shown in Figure 2-13. For this purpose the 3D image of the actual microstructure was obtained by assembling multiple 2D images of the microstructure taken at different depths. This can be done by grinding and polishing the sample over and over and taking an image at each step or by doing a 3D reconstruction of microstructure using 3D electron backscatter diffraction (EBSD). Brands et al [43] used the 3D EBSD technique to produce a 3D RVE of a dual phase steel. They put the sample on a tiltable holder inside of a field emission scanning electron microscope (FESEM) equipped with a focused ion beam (FIB) cutting system. During the investigation the sample was tilted between two positions: FIB-cutting and the EBSD positions. After taking the EBSD image, the FIB system milled thin layers (10 nm - 1µm) from the investigated surface of the sample. The 3D RVE of the dual phase steel was generated by assembling the EBSD images.

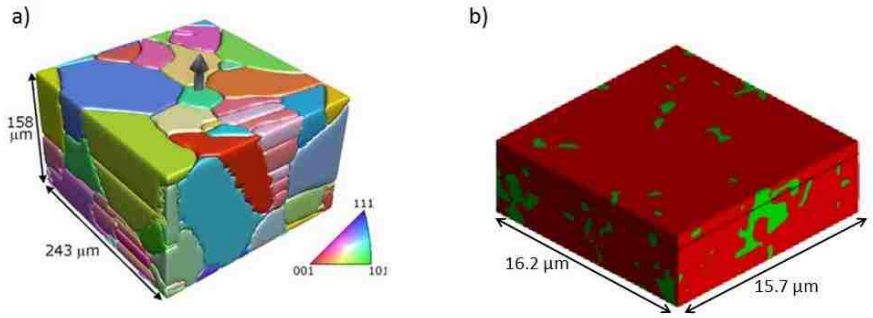

Figure 2-13 3D reconstruction of (a) austenite phase in AL-6XN microstructure [42] and (b) dual phase steel [43] using EBSD.

There are some advantages and disadvantages for both 2D and 3D RVEs:

- It is much easier to generate 2D RVEs from real microstructure than to produce 3D RVEs, and they are able to take into account the microstructural morphology.
- Calculation time for 2D RVEs is less than for 3D RVEs. Ramazani et al reported that the calculation time for a 2D RVE based on a real microstructure took 30 min whereas it took 240 min for a simple cubic 3D RVE [40].
- 2D modeling has less complexity and lower computational cost compared to 3D modeling; however, comparing the experimental and predicted results has shown that 2D modeling underestimates the flow behaviour of dual phase steels but 3D modeling results correlated very well with experimental results [39][40].

2.4.2 Definition of Flow Behaviour of Each Phase

To determine the flow behaviour of ferrite, martensite and bainite in dual phase steels, a dislocation based model was developed by Rodrigues and Gutierrez [44] which has been used by many researchers [35–37,39,40,45–49]. The development of this model is explained in the following.

As illustrated by Gil-Sevillano [50], the orientation factor, M, relates the macroscopic flow stress, σ, and the critical resolved shear stress, τ, and the plastic strain, ε, to the amount of crystallographic slip, ϒ, as shown below:

$$\sigma = M\tau$$
$$M \cdot d\varepsilon = d\gamma \qquad 2\text{-}3$$

From Equation 2-3, the macroscopic work hardening rate relates to the microscopic material parameters by:

$$\frac{d\sigma}{d\varepsilon} = M^2 \frac{d\tau}{d\gamma} + \tau \frac{dM}{d\varepsilon} \qquad 2\text{-}4$$

where $d\tau/d\gamma$ represents the microscopic hardening rate of the crystalline element. The effect of strain on orientation variation is presented by the second term in Equation 2-4.

The classic relationship between the flow stress and dislocation density is:

$$\sigma_f = \sigma_0 + \Delta\sigma = \sigma_0 + \alpha M \mu b \sqrt{p} \qquad 2\text{-}5$$

where α is a constant, M is the Taylor factor, μ [MPa] is the shear modulus, b [m] is the Burger's vector, and p is the dislocation density.

The first term in Equation 2-5 takes into account the contribution of the lattice friction and the elements in solid solution. For a series of different steels with microstructures containing ferrite, pearlite, bainite and martensite with different levels of carbon content, the following expression for σ_0 was suggested by Buessler [51]:

$$\sigma_0 = 77 + 80\%Mn + 750\%P + 60\%Si + 80\%Cu + 45\%Ni + 60\%Cr + 11\%Mo + 5000N_{ss} \qquad 2\text{-}6$$

All the elements are assumed to be homogeneously distributed in each phase.

The second term in Equation 2-5 is expanded based on dislocation density. Evolution of the dislocation density with strain during the deformation can be expressed as [52]:

$$\frac{dp}{d\gamma} = \frac{dp}{d\gamma}\Big|_{stored} - \left.\frac{dp}{d\gamma}\right|_{recovery} = \frac{1}{bL} - k_r p \qquad 2\text{-}7$$

where k_r is a constant and L is the dislocation mean free path. From Equation **2-7** and considering p_0 as the initial dislocation density and assuming that L is constant, the equation for Δσ will be:

$$\Delta\sigma = \alpha M \mu b \sqrt{\frac{k}{k_r}\left[1 - \exp(-k_r M \varepsilon)\right] + p_0 \exp(-k_r M \varepsilon)} \quad \text{with } k = \frac{1}{bL} \qquad 2\text{-}8$$

So the equation for Δσ can be written as:

$$\Delta\sigma = \alpha M \mu \sqrt{b} \sqrt{\frac{1 - \exp(-M k_r \varepsilon)}{k_r L}} \qquad 2\text{-}9$$

Since the two terms in the Equation 2-5 are defined, the total approach for determination of the flow curve of each phase is [44]:

$$\sigma = \sigma_0 + \Delta\sigma_c + \alpha \times M \times \mu \times \sqrt{b} \times \sqrt{\frac{1 - \exp(-M k_r \varepsilon)}{k_r \times L}} \qquad 2\text{-}10$$

where σ is the true flow stress for a true strain of ε.

The first term σ_0 takes care of the effects of substitutional alloying elements as presented in Equation **2-6**. The second term, $\Delta\sigma_c$, describes the strengthening due to interstitial carbon; however the strengthening effect of carbon in ferrite is not the same as in martensite. Therefore $\Delta\sigma_c$ is calculated differently for ferrite and martensite [44]:

$$\Delta\sigma_c^f = 5000 \times (\%C_{SS}^f) \qquad 2\text{-}11$$

$$\Delta\sigma_c^m = 3065 \times (\%C_{SS}^m) - 161 \qquad 2\text{-}12$$

where $\%C_{SS}^f$ and $\%C_{SS}^m$ are the carbon wt% in ferrite and martensite, respectively.

The values of the parameters in the third term of Equation **2-10** are presented in Table 2-1.

Table 2-1 The values of the parameters in the third term of Equation **2-10**

M: Taylor Factor	*M=3*
μ: Shear Modulus	*μ= 80000 MPa*
b: Burger's vector	*b=2.5×10^{-10}m*
α: constant	α*=0.33*
K_r: Recovery Rate	For ferrite ($k_r = 10^{-5}/d\alpha$), where dα is the ferrite grain size [53] For martensite (k_r=41) [53] For bainite, ($k_r = 10^{-5}/d\gamma$), where d_γ is the prior austenite grain size [46]
L: dislocation mean free path	For ferrite (L= dα) [53] For martensite (*L= 3.8×10^{-8} m*) [53] For bainite (L= 2 × 10^{-7}) [46]

For bainite the factor L is assumed to be the average distance between low angle grain boundaries measured in random directions. Bainite laths are generally 0.2 μm wide and therefore L is considered as the value presented in Table 2-1. K_r for bainite is considered to relate to the prior austenite grain size as shown in Table 2-1. Using the prior austenite grain size seems to give a better estimation since using the bainitic ferrite lath width in the Hall-Petch equation results in an excessively high strength contribution [46]. Hence, the prior austenite grain size needs to be identified to determine the flow behaviour of bainite.

For bainite, the effect of dislocation strengthening is more significant than the strengthening effect by carbon solid solution [29]. $\Delta\sigma_c$ for bainite is considered to be a function of the prior austenite grain size and transformation temperature. The transformation temperature dependency comes from the fact that $\Delta\sigma_c$ depends on transformation dislocations. By decreasing the bainite transformation temperature, the

amount of dislocation increases. Prior austenite grain size also affects the $\Delta\sigma_c$ of bainite as it can affect the bainitic transformation temperature and kinetics [29][46].

The hardness of bainite grains was reported to be equal to the hardness of ferrite and martensite according to the mixture rule [37]:

$$\Delta\sigma_c^b = \Delta\sigma_c^f V_f + \Delta\sigma_c^m V_m \qquad 2\text{-}13$$

where V is the volume fraction of phases in the dual phase steel microstructure.

2.4.3 Application of Boundary Conditions and Solving the Problem

Kouznetsova [54] described the theory of boundary conditions for micromechanical modeling of multi-phase materials in her PhD thesis. A summary of this theory is presented in the following.

Appropriate boundary conditions such as loading and constraints should be applied to an RVE to investigate the flow behaviour of RVE in a specific condition. This will define a problem in continuum solid mechanics which will be solved by the finite element method.

The RVE deformation field in a point with initial position vector $\vec{X}$ (in the reference domain of V_0) and the actual position vector $\vec{x}$ (in the current domain V) is described by the deformation gradient tensor:

$$F_m = (\nabla_{0m}\vec{x})^c \qquad 2\text{-}14$$

where the gradient operator ∇_{0m} is taken with respect to the reference microstructural configuration. Also the RVE is in a state of equilibrium, which mathematically is reflected by an equilibrium equation in terms of the Cauchy stress tensor σ_m. It can be described in terms of the first Piola-Kirchhoff stress tensor of P_m which is presented below:

$$\nabla_m \cdot \sigma_m = \vec{0} \text{ in V}, \quad \text{or} \qquad 2\text{-}15$$

$$\nabla_{0m} \cdot P_m^c = \vec{0} \text{ in } V_0$$

$$P_m = \det(F_m)\sigma_m \cdot (F_m^c)^{-1} \qquad 2\text{-}16$$

where ∇_m is the gradient operator with respect to the current deformation of the microstructure. By imposing the macroscopic deformation gradient tensor F_M on the microstructural RVE through a specific approach, the actual macro-to-micro transition is possible. The simplest is to use the Taylor (or Voigt) assumption which assumes that all of the microstructure constituents are subject to a constant deformation which is the same as the macroscopic deformation. Another assumption is that of Sachs (or Russ) which assumed that an identical constant stress is applied to all the components. These simplified assumptions do not really reflect the actual deformation of the microstructure. Many of the accurate averaging strategies require the solution of the detailed microstructural boundary value problem to transfer the given macroscopic variables to the microstructural RVE via the boundary conditions. Classically, three types of RVE boundary conditions are used, i.e. prescribed displacements, prescribed forces and prescribed periodicity.

In prescribing displacement boundary conditions, the position vector of a point on the RVE boundary in the deformed state is defined as:

$$\vec{x} = F_M \cdot \vec{X} \quad \text{with } \vec{X} \text{ on } \Gamma_0 \qquad 2\text{-}17$$

where Γ_0 denotes the undeformed boundary of the RVE and F_M the macroscopic deformation gradient tensor on the microstructural RVE. This kind of condition prescribes a linear mapping of the RVE boundary.

The traction boundary conditions, are described as:

$$\vec{t} = \vec{n}.\sigma_m \text{ on } \Gamma, \text{ or} \qquad 2\text{-}18$$
$$\vec{p} = \vec{N}.P_M^c \text{ on } \Gamma_0$$

where $\vec{n}$ and $\vec{N}$ are the normal to the current (Γ) and initial (Γ_0) RVE boundaries, respectively.

Periodic boundary conditions were introduced based on the assumption of microstructural periodicity [54]. The periodicity conditions of the RVE are presented in a general form in Equation 2-19 which represents a periodic deformation:

$$\vec{x}^{+} - \vec{x}^{-} = F_M \cdot (\vec{X}^{+} - \vec{X}^{-}) \qquad 2\text{-}19$$

From Equation 2-19 and Figure 2-14, the parts of RVE boundary Γ_0^- and Γ_0^+ are defined in such a way that $\vec{N}^{-} = -\vec{N}^{+}$ at corresponding points on Γ_0^- and Γ_0^+.

The periodic boundary condition can be expressed as:

$$\begin{aligned} \vec{x}_T &= \vec{x}_B + \vec{x}_4 - \vec{x}_1 \\ \vec{x}_R &= \vec{x}_L + \vec{x}_2 - \vec{x}_1 \\ \vec{x}_3 &= \vec{x}_2 + \vec{x}_4 - \vec{x}_1 \end{aligned} \qquad 2\text{-}20$$

Where $\vec{x}_T$, $\vec{x}_B$, $\vec{x}_L$, and $\vec{x}_R$, are the position vector at the top, bottom, left, and right, boundary of the RVE, respectively. $\vec{x}_i$ (i= 1, 2, 3, 4) are position vectors of the corner points 1, 2, 3, and 4, in the deformed state, respectively. These position vectors are described according to:

$$\vec{x}_i = F_M \cdot \vec{X}_i \quad \text{and i=1,2,3,4} \qquad 2\text{-}21$$

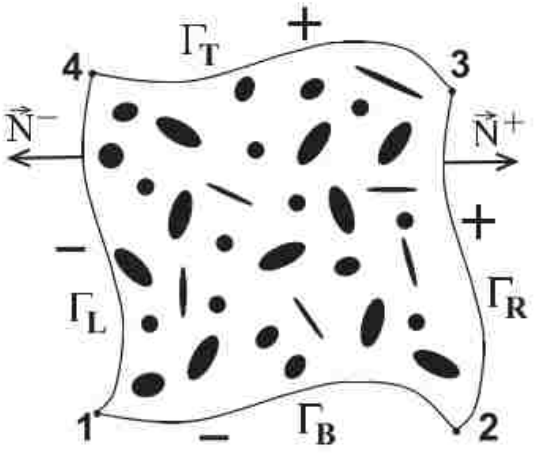

Figure 2-14 Schematic of a typical 2D RVE.

It has been reported [55][56] that the periodic boundary condition provides a better estimation of the overall properties of the microstructure compared to the prescribed displacement and prescribed traction boundary conditions.

2.4.4 Homogenization

Kouznetsova [54] also described the theory of homogenization for micromechanical modeling of multi-phase materials. A summary of this theory is provided in the following.

Homogenization is a technique that relates the micro-scale behaviour of a material to its macroscopic behaviour. Computational homogenization technique has proven to be a valuable tool to establish non-linear micro-macro structure-property relations. In homogenization, the material is assumed to be sufficiently homogeneous at the macro-scale, but heterogeneous at the micro-scale due to the existence of inclusions, grains, interfaces, cavities, etc.

Two approaches are proposed to describe the periodicity of the inhomogeneity in the microstructure: global periodicity and local periodicity which are schematically shown in Figure 2-15. In the global periodicity approach, the same inhomogeneity is assumed to repeat itself throughout the whole microstructure. The local periodicity approach is preferred since it allows a microstructure to include a variety of inhomogeneities with different morphologies that are repeated at individual macroscopic points. Hence, it allows the modeling of the effects of a non-uniform distribution of the microstructure on the macroscopic response which is more realistic [54].

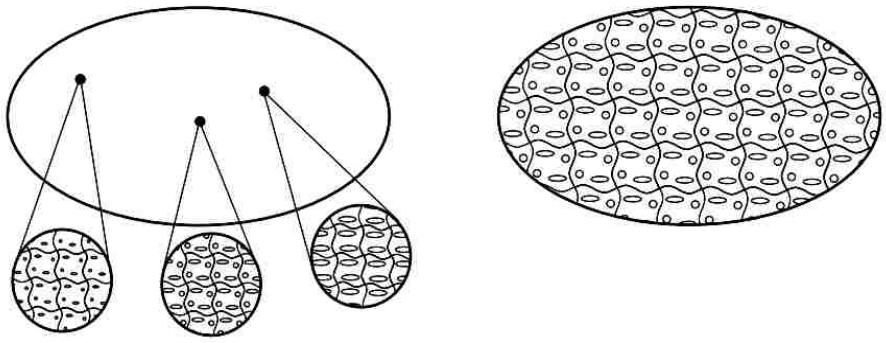

Figure 2-15 Schematic representation of a macrostructure with (a) a locally and (b) a globally periodic microstructure [54].

It has been reported that a first order computational homogenization technique can be used for RVE problems [40][54][57]. In a homogenization procedure macroscopic and microscopic quantities are shown by "M" and "m", respectively. As it is designated in Figure 2-16, the first-order homogenization is carried out in three steps:

- The deformation tensor, F_M, is calculated for every material point, i.e. the integration points of the macroscopic mesh in a FE model.
- F_M of a macroscopic point is used to formulate the boundary conditions which are imposed on the RVE located on that point which results in the deformation of the RVE.
- The stress tensor, P_M, of the initial macroscopic point is obtained by averaging the resulting RVE stress field over the volume of the RVE.

The numerical stress-deformation relationship at the macroscopic point is the result of this procedure. Furthermore, the local macroscopic consistent tangent is obtained based on the microstructural stiffness and response.

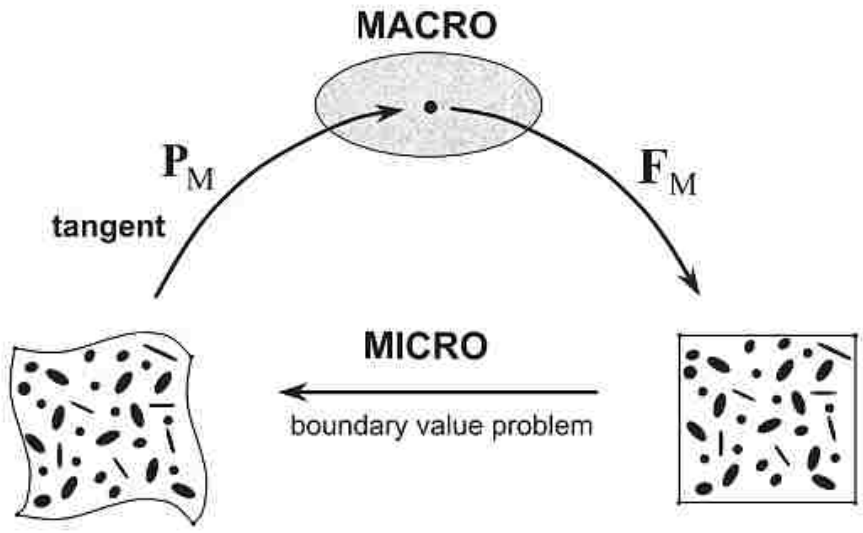

Figure 2-16 Schematic representation of first-order homogenization [54]

In first order homogenization, coupling of the macroscopic and microscopic deformation and stress is carried out by application of integral averaging theorems. The integral averaging expressions were first proposed by Hill (1963) [58] for small deformations and developed for large deformation by Hill (1984) [59] and Nemat-Nasser (1999) [60] as follows:

Deformation It is assumed that the macroscopic deformation gradient tensor F_M is the volume average of the microstructural deformation gradient tensor F_m:

$$F_M = \frac{1}{V_0}\int_{V_0} F_m dV_0 = \frac{1}{V_0}\int_{\Gamma_0} \vec{x}\vec{N}d\Gamma_0 \qquad 2\text{-}22$$

where V_0 is the undeformed volume of the RVE. The divergence theorem is used to transform the volume integral over V_0 of the RVE to a surface integral. The validation of Equation **2-22** for the periodic boundary condition (Equation **2-20**) is:

$$F_M = \frac{1}{V_0}\left\{\int_{\Gamma_0^+} \vec{x}^+\vec{N}^+ d\Gamma_0 + \int_{\Gamma_0^-} \vec{x}_0\vec{N}^- d\Gamma_0\right\} = \frac{1}{V_0}\int_{\Gamma_0^+} (\vec{x}^+ - \vec{x}^-)\vec{N}^+ d\Gamma_0 \qquad 2\text{-}23$$

$$= \frac{1}{V_0}F_M \cdot \int_{\Gamma_0^+} (\vec{X}^+ - \vec{X}^-)\vec{N}^+ d\Gamma_0 = \frac{1}{V_0}F_M \cdot \int_{\Gamma_0} \vec{X}\vec{N} d\Gamma_0 = F_M$$

where $\bar{x}$ is position vector of nodes in deformed state and $\bar{X}$ is position vector of nodes in undeformed state. $\vec{n}$ and $\vec{N}$ are the normal to the current (Γ) and initial (Γ_0) RVE boundaries, respectively.

Stress The averaging relation for the first Piola-Kirchhoff stress tensor is:

$$P_M = \frac{1}{V_0}\int_{V_0} P_m dV_0 \qquad 2\text{-}24$$

The macroscopic Piola-Kirchhoff stress tensor P_M in the microstructural quantities defined on RVE surface is:

$\nabla_{0m} \cdot P_m^c = \vec{0}$ for microscopic equilibrium 2-25

$\nabla_{0m}\vec{X} = I$ for microstructure equality

$$P_m = (\nabla_{0m} \cdot P_m^c)\vec{X} + P_m \cdot (\nabla_{0m}\vec{X}) = \nabla_{0m} \cdot (P_m^c\vec{X})$$

By substitution of Equation **2-25** into Equation **2-24** and applying the divergence theorem and definition of the first Piola-Kirchhoff stress vector according to Equation 2.14, P_M of RVE is obtained over the surface:

$$\vec{p} = \vec{N} \cdot P_m^c \qquad 2\text{-}26$$

$$P_M = \frac{1}{V_0}\int_{V_0} \nabla_{0m} \cdot (P_m^c\vec{X}) dV_0 = \frac{1}{V_0}\int_{\Gamma_0} \vec{N} \cdot P_m^c\vec{X} d\Gamma_0 = \frac{1}{V_0}\int_{\Gamma_0} \vec{p}\vec{X} d\Gamma_0 \qquad 2\text{-}27$$

By considering the periodicity conditions (Equations **2-20** and **2-21**) for the RVE shown in Figure 2-14, it can be verified that the external forces are the only applied boundary condition which contributes to the boundary integral (Equation **2-27**) as defined by the following expression at the three prescribed corner nodes:

$$P_M = \frac{1}{V_0} \sum_{i=1,2,4} \vec{f}_i \vec{X}_i \qquad 2\text{-}28$$

where $\vec{f}_i$ are the resulting external forces at the boundary nodes and $\vec{X}_i$ are the position vectors of these nodes in the undeformed state.

2.5 Key Points in RVE-based Modeling of Dual Phase Steels

Several researchers have developed RVE-based micromechanical models to predict the flow behaviour of dual phase steels. In 1999, Huper et al [61] modeled the flow behaviour of dual phase steel based using an FE model. They found that flow behaviour of dual phase steels depended on volume fraction of phases and the shape of the grains. In 2000, Ishikawa et al [62] used a body centered cubic (BCC) cell model to investigate the effects of volume fraction and morphology of second-phase particles on deformation behaviour of ferritic steels. The cell model proposed by Ishikawa et al accurately estimated the tensile behaviour of ferrite-pearlite steels. In 2003, Al-Abbasi and Nemes [63,64] studied the effects of martensite volume fraction and martensite size on strength and ductility of dual phase steel using a cell model. After 2010, the number of publications on micromechanical modeling of flow curves of dual phase steels notably increased. Uthaisangsuk et al [35] suggested a 3D RVE-based micromechanical model of randomly distributed martensite in a ferrite matrix to predict flow curves of a dual phase steel and a TRIP steel. Marvi-Mashhadi et al [65] predicted flow curves of dual phase steels with 18-44 vol% of martensite by development of an RVE-based FE model using the actual microstructure of dual phase steels. Sodjit et al [66] modeled the flow curves of dual phase steel with 25-90 vol% of martensite by proposing a 2D RVE-based FE model using actual microstructures. They also studied the effect of martensite volume fraction on the behaviour of the flow curves of dual phase steels. Paul et al [45,67] developed 2D and 3D RVE-based models to predict flow behaviour of a dual phase steel. Plastic strain localization under tensile loading was studied as a pre-stage of failure. Finally, Ramazani et al [40,49] studied the flow behaviour of dual phase steels using 2D and 3D RVE-based models. The optimum RVE size was reported. Also, 2D plane strain modeling was found to

result in underestimation of flow curve of dual phase steels while 3D modeling provided a better description.

During micromechanical modeling of flow behaviour of dual phase steels using the RVE method several parameters must be considered in order to optimize the results. The effects of some of the modeling parameters such as RVE size, martensite morphology, mesh size and dimension of modeling, i.e. 2D versus 3D, are discussed in the following.

RVE Size It was mentioned before that the size of the RVE should be carefully selected. A too small RVE cannot represent the average characteristics of the whole microstructure and a too large RVE significantly increases the complexity and time of calculations. Ramazani et al [49] modeled the flow behaviour of a DP600 steel with 35 vol% of martensite. They reported that selection of the optimum RVE size in 2D modeling of real microstructure image is crucial. To find the optimum RVE size for convergence of results; nine different volume elements (VE) were selected and investigated. The VEs sizes which were created from the optical micrographs varied between 5x5 and 30x30 μm^2. The number of martensite islands inside each RVE was quantified. A similar element type with the same mesh size was applied in all cases. Figure 2-17 shows the volume elements and the corresponding modeling results. Although the predictions of VE6, VE7, VE8 and VE9 converge VE6 with a size of 24×24 μm^2 size was chosen as the best RVE size since it could predict the proper flow behaviour and also needed less calculation time. Convergence was achieved when the RVE included at least 19 martensite particles.

Morphology of Martensite Determination of the precise morphology and distribution of martensite in the microstructure affects the accuracy of the modeling results. The morphology of each phase affects the stress and strain partitioning between ferrite and martensite in the microstructure which in turn influence the flow behaviour of the dual phase steel. Thomser et al [36] studied the effects of distribution of martensite in a 2D RVE on flow behaviour of dual phase steels with 42% of martensite. They considered fine and coarse distributions of martensite in the microstructure, and the ferrite grain size was similar in both microstructures. Figure 2-18 presents the numerical and experimental flow curves for both fine and coarse microstructures. As can be seen, the stress-strain response

of the fine microstructure is higher than that of the coarse microstructure. The microstructure with a fine martensite distribution has a narrow martensite phase with sharp edges at the martensite-ferrite interface which increases stress concentrations and plastic deformation [36].

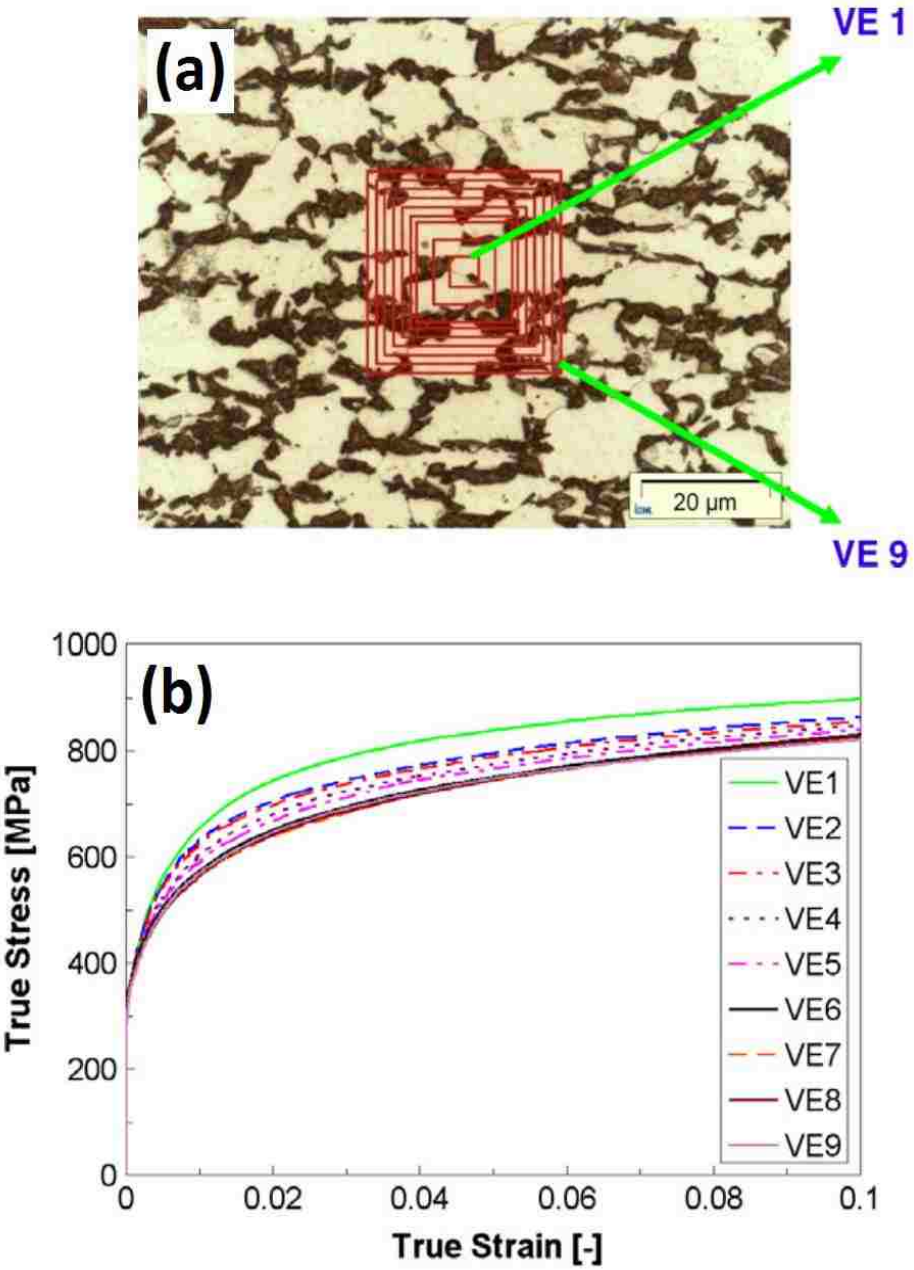

Figure 2-17 (a) Volume elements VE 1–VE9 in a DP600 with 35% martensite and (b) predicted corresponding flow curves from numerical tensile tests [49]

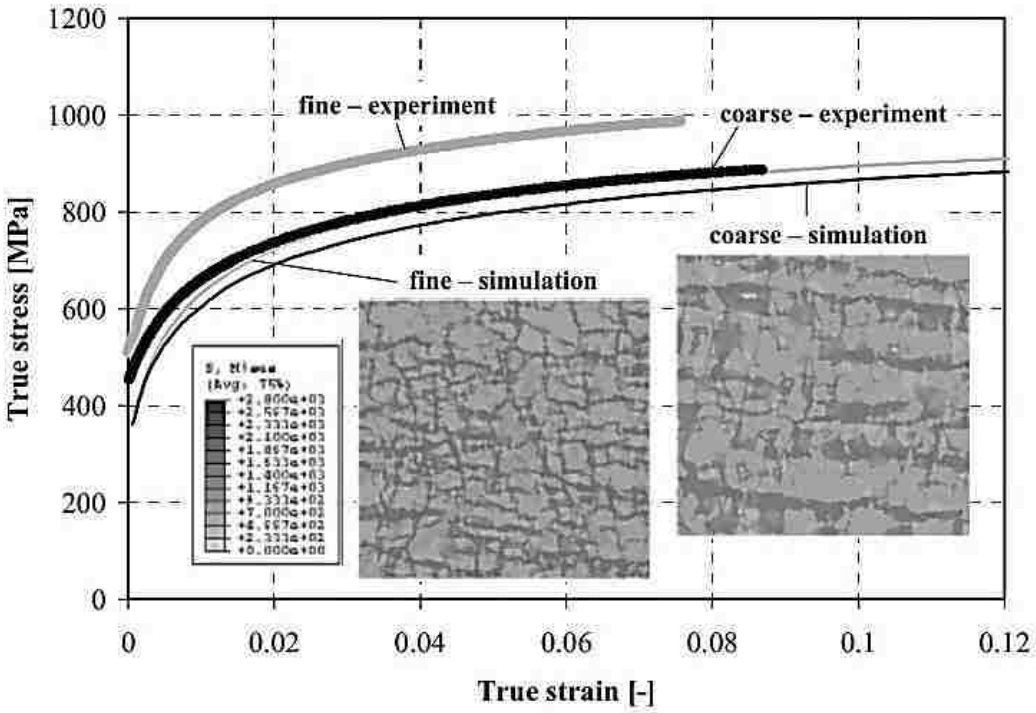

Figure 2-18 Comparison between experimental and numerical flow curves of a dual phase steel with fine and coarse distribution of martensite in the microstructure [36]

Mesh Size The effect of mesh refinement on the stress-strain partitioning in the RVE was studied by Uthaisangsuk et al [35]. Different mesh sizes from 100×100 to 260×260 elements were applied to a 2D RVE of the real microstructure of DP600 steel with 27 vol% of martensite. Figure 2-19 shows small discrepancies in flow behaviour of the RVEs with different mesh sizes. It was also found that the 2D RVE simulation with a mesh size finer than 260×260 did not provide different results. Uthaisangsuk et al [35] also investigated the influence of mesh size on a 3D RVE of a dual phase steel with 13 vol% of martensite. As it is shown in Figure 2-20, a coarse mesh and a fine mesh, with double the number of elements as the coarse mesh along each side of the RVE, were applied. The martensite distribution was similar in both cases. The true stress-strain responses were calculated for both RVEs, and as can be seen in Figure 2-20, no remarkable discrepancy was observed in the flow curves due to the variation in mesh size.

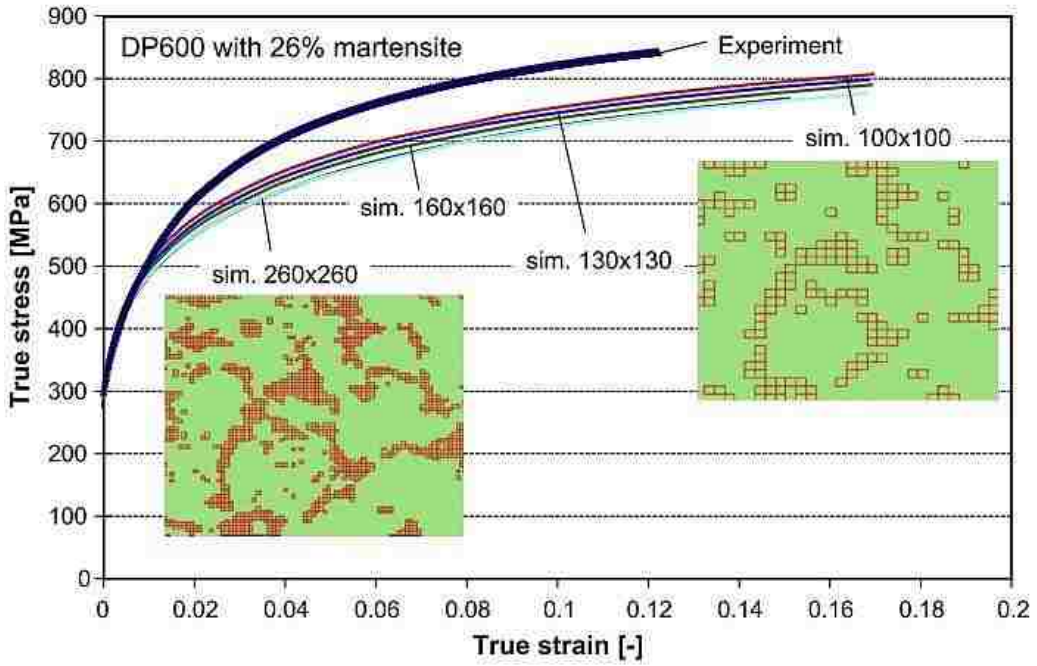

Figure 2-19 Influence of the mesh size on true stress-strain response of a 2D RVE for DP600 steel with 27 vol% of martensite [35]

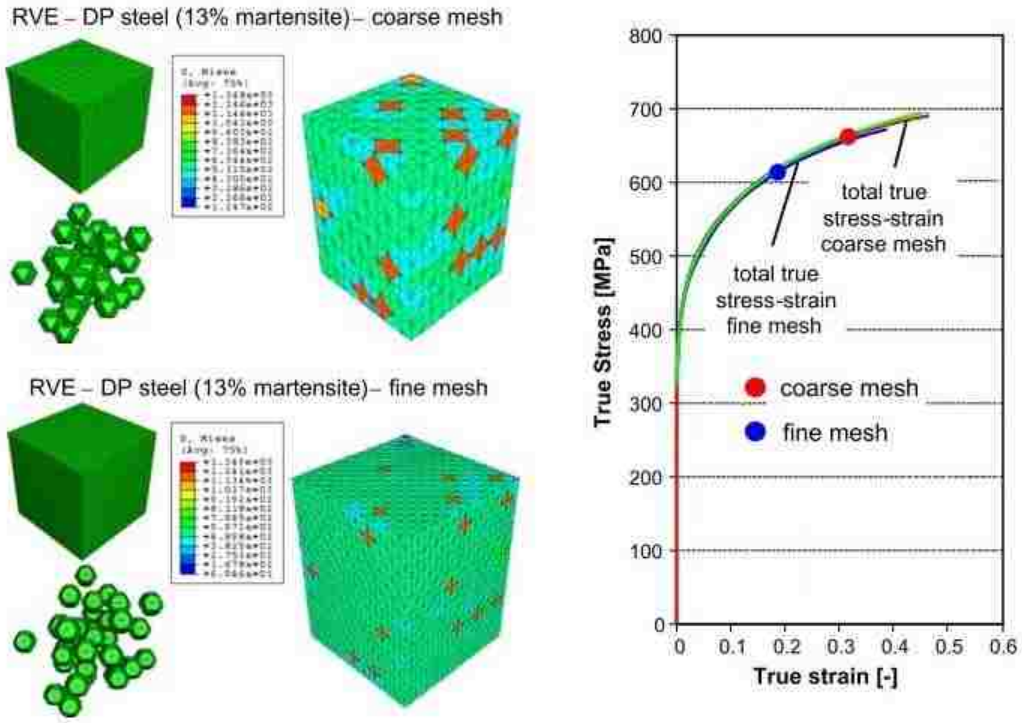

Figure 2-20 Influence of mesh size on flow behaviour of a 3D RVE of a dual phase [35]

2D versus 3D Modeling 2D and 3D RVEs can be used for micromechanical modeling of flow behaviour of dual phase steels. Application of 3D RVEs significantly increases the time of calculations and the level of required computational resources. Uthaisangsuk et al [35] compared the results of 2D and 3D modeling results for two dual phase steels with 20 and 45 vol% of martensite, and their results are presented in Figure 2-21. As can be seen, in both cases, the stress-strain response of the 3D RVEs are closer to the experimental flow curves. As it was shown in Figure 2-18, Thomser et al [36] reported underestimation for all flow curves predicted from the 2D RVEs. Although the flow curves were underestimated, the rates of strain hardening were correctly predicted in both cases. The underestimation was explained to occur because 2D RVEs were assumed to deform in a mode of plane strain. Al Abbasi and Nemes [63] modeled the flow curves of dual phase steels with 32-36 vol% of martensite using different cell models. They also indicated that the 2D plane strain model appeared to underestimate the strain hardening compared to axisymmetric 3D model.

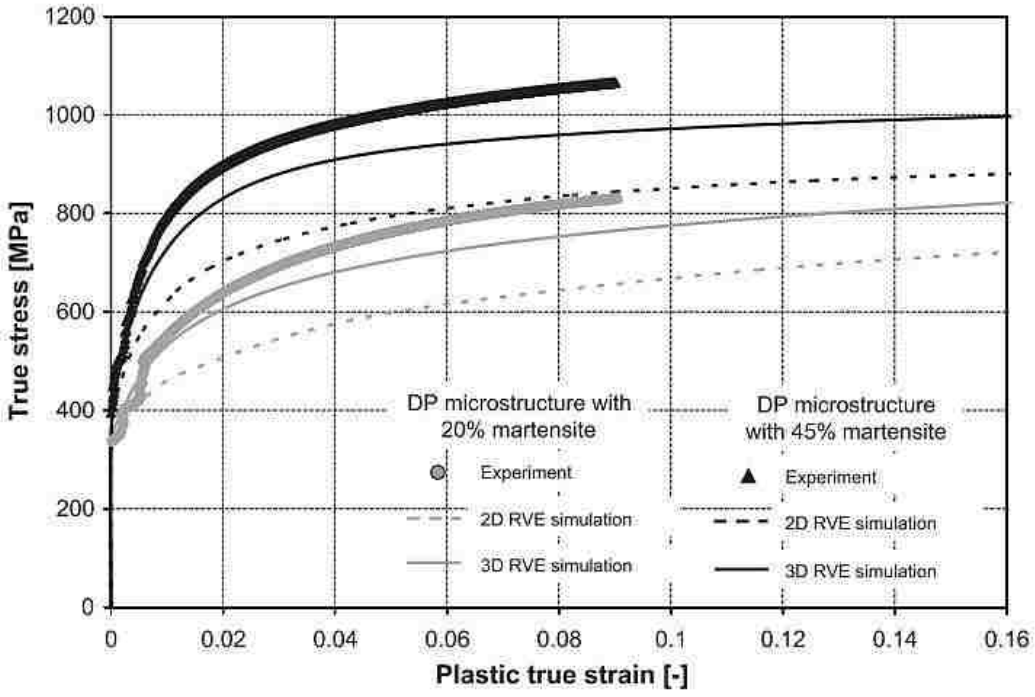

Figure 2-21 True stress-strain curves of 2D and 3D RVE of two dual phase steels with 20 and 45 vol% of martensite [35]

3 Materials Characterization

In this research, micromechanical models were developed to predict the flow behaviour of commercial DP500 and DP600 dual phase steel sheets in uniaxial tensile test prior to necking. The thickness of the DP500 and DP600 steel was 0.65 and 1 mm, respectively. Table 3-1 shows the chemistry of the as-received steels. The elements found in quantities greater than 0.01 wt% are shown in the table. The effects of carbon and the alloying elements with amounts greater than 0.1 wt% are considered in the model.

Table 3-1 Chemistry of DP500 and DP600 steels

	C	Mn	Mo	Cr	Si	Cu	Al	Ti	Ni
DP500	0.063	1.83	0.01	0.03	0.02	-	-	-	0.01
DP600	0.107	1.497	0.214	0.181	0.175	0.057	0.038	0.025	0.015

Chemical and mechanical characterizations were accomplished to obtain the required parameters for the model. The experimental procedures and results are presented in the following.

3.1 Quantitative Metallography of As-received Dual Phase Steels

For metallography of the as-received DP500 and DP600 steel sheet, samples were cut and mounted as shown in Figure 3-1. Diallyl Phthalate thermosetting resin powder was used as the mounting powder which was cured at 150 °C and 20 MPa for 90 s. BuehlerMet® II Abrasive Discs C with a Grit ANSI of 60 to 600 were used to grind the mounted samples. A three-step polishing was carried out including: MetaDi® Polycrystalline Diamond Suspension of 9 µm, followed by Micropolish® II Deagglomerated Alpha Alumina powders of 1.0 and 0.05 µm suspended in water.

The microstructure of DP500 steel contained ferrite and martensite. The entire quantitative metallography procedure for DP500 samples was carried out at the University of Windsor. Nital 2% was used for etching of the samples.

Sample preparation of DP600 steel was carried out at the University of Windsor. Etching and quantitative analysis of the samples were performed at Metallography Lab at ArcelorMittal Dofasco. The microstructure of DP600 steel, contained ferrite, bainite and martensite. Generally, Nital 2% is used for etching dual phase steels which reveals ferrite grains in white and grain boundaries, martensite islands, bainite grain and carbide particles in black; however, micromechanical modeling requires accurate quantitative metallography data of each constituent. Hence, etching should be performed in a way that high contrast exists between the constituents. Consequently, each individual constituent can be chosen in the image analysis software to obtain accurate quantitative metallography. For this purpose, as it is shown in Table 3-2, three different etchant were used: Nital 2%, Picral 4% and LePera for observation of ferrite, bainite and martensite, respectively. Figure 3-3, Figure 3-4 and Figure 3-5 show the microstructures of DP600 steels etched by Nital 2%, Picral 4% and LePera, respectively.

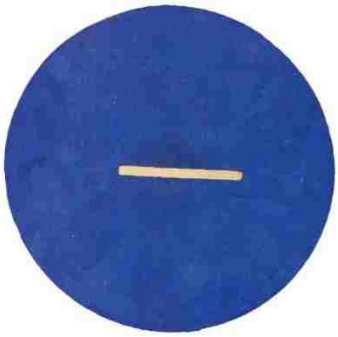

Figure 3-1 The mounted through-thickness sample of as-received DP600 steel

Table 3-2 Etchants used to etch DP600 steel

Nital 2%	nitric acid + Ethanol	ferrite: light gray others: dark gray/black
Picral 4%	picric acid (2,4,6-trinitophenol) + ethanol	bainite: black others: gray
LePera	50 ml $Na_2S_2O_5$ 1% in aqueous dilution, 50 ml picric acid 4% in ethanol	martensite: white others: gray/black

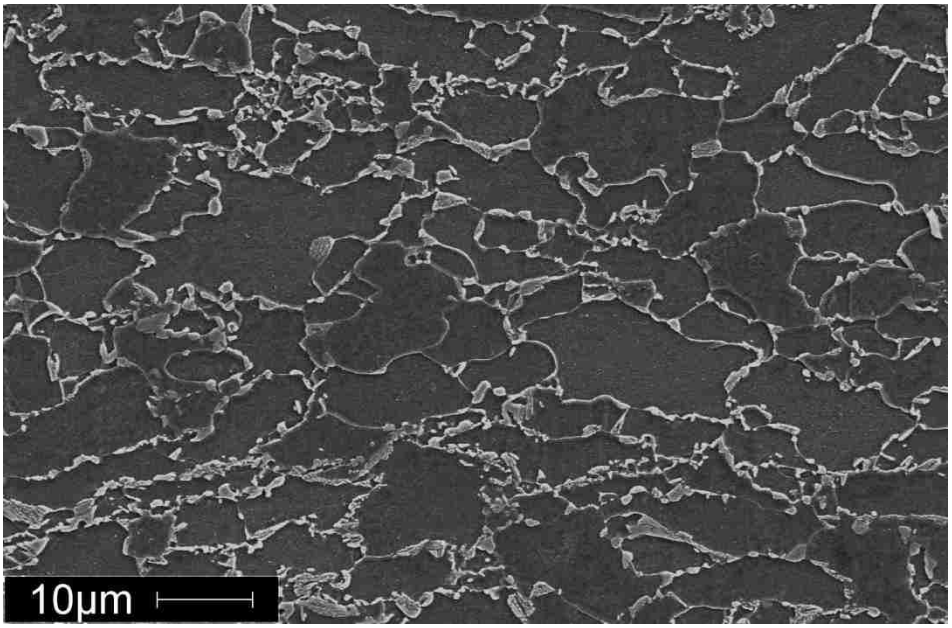

Figure 3-2 Scanning electron microscope through-thickness microstructure of as-received DP500 etched by Nital 2%; ferrite is dark gray and martensite is light gray.

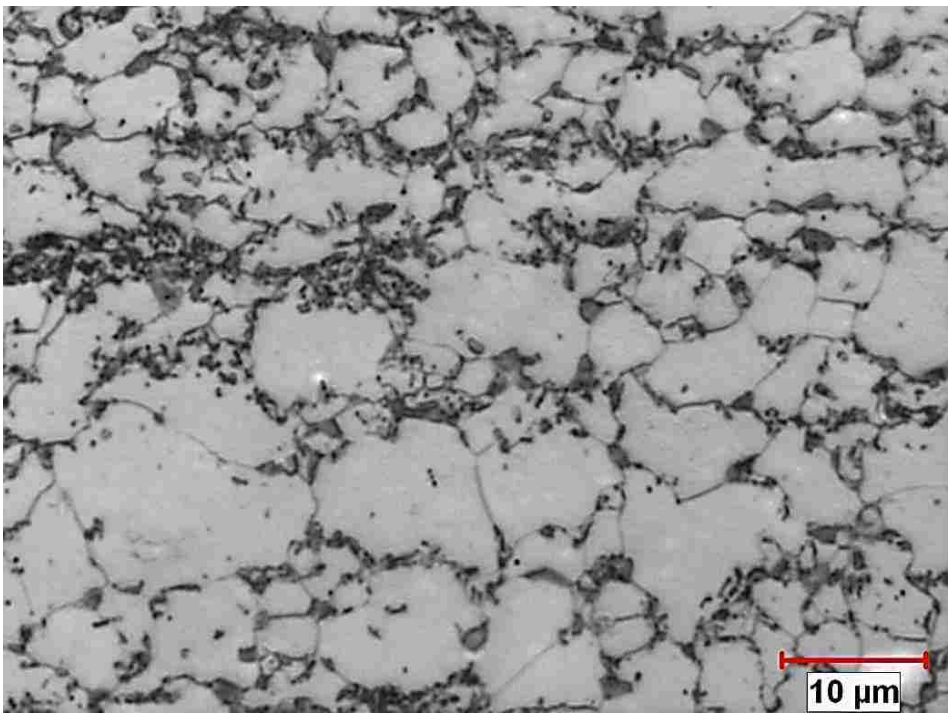

Figure 3-3 Optical through-thickness microstructure of as-received DP600 etched by Nital 2%; ferrite is etched in light gray and the other constituents are in dark gray/black.

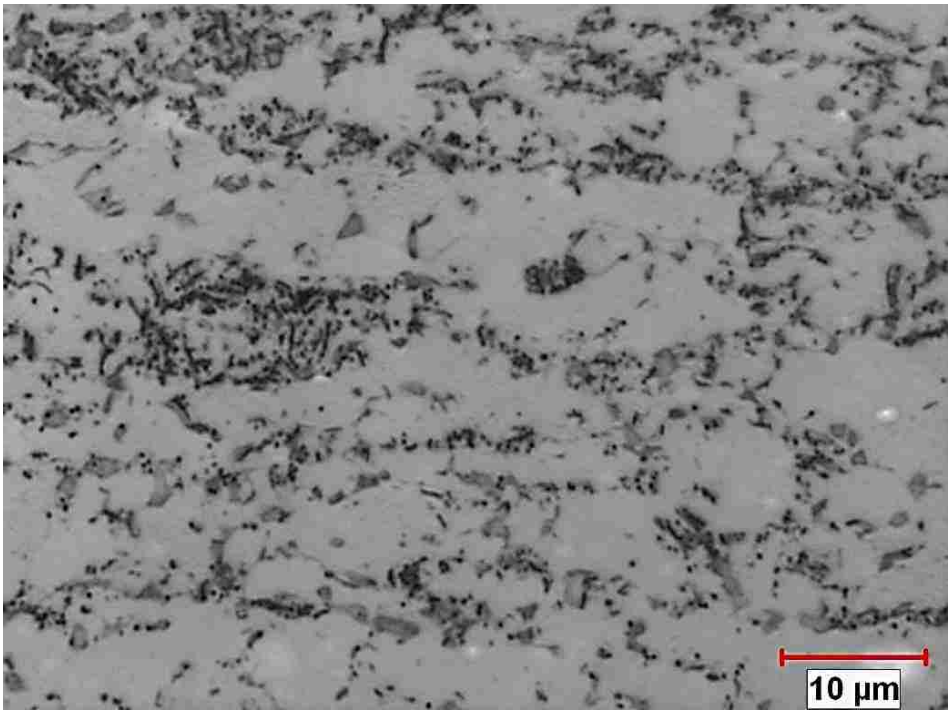

Figure 3-4 Optical through-thickness microstructure of as-received DP600 etched by Picral 4%; bainite is etched in black and the other constituents are in gray.

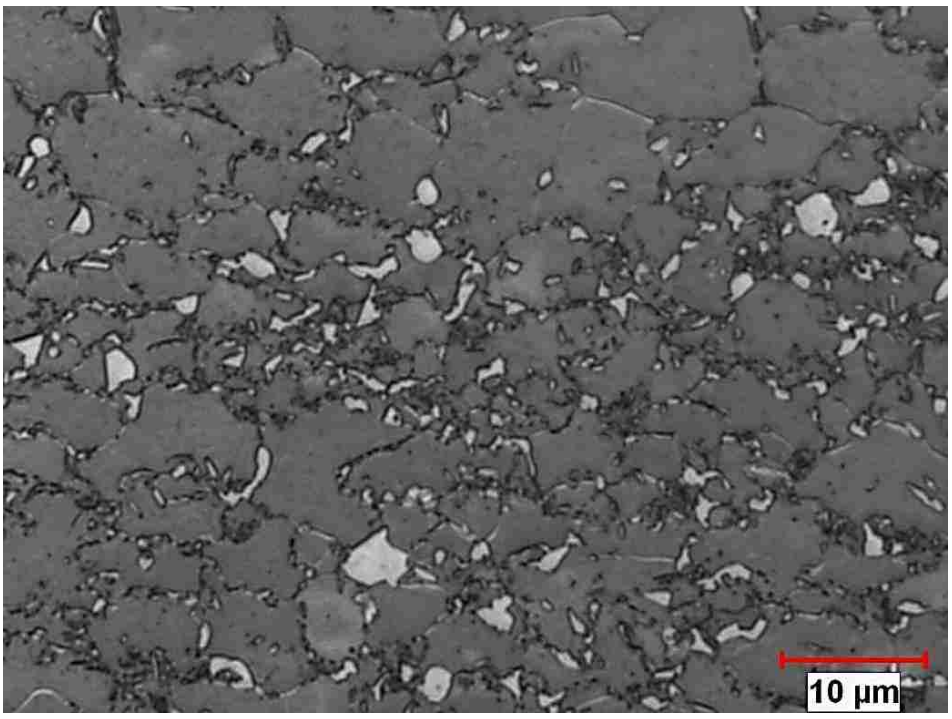

Figure 3-5 Optical through-thickness microstructure of as-received DP600 etched by LePera; martensite is etched in white and the other constituents are in gray/black.

For quantitative metallography, through-thickness micrographs were analyzed using Clemex Vision software. In the image analysis procedure, a colour is assigned to the constituent which is being analyzed. Also, a different colour is assigned to the other areas of the micrograph. For instance, as it is shown in Figure 3-6, martensite is coloured in red and the other phases in yellow. The volume fraction of martensite will be the ratio of red pixels to the total number of pixels (red and yellow).

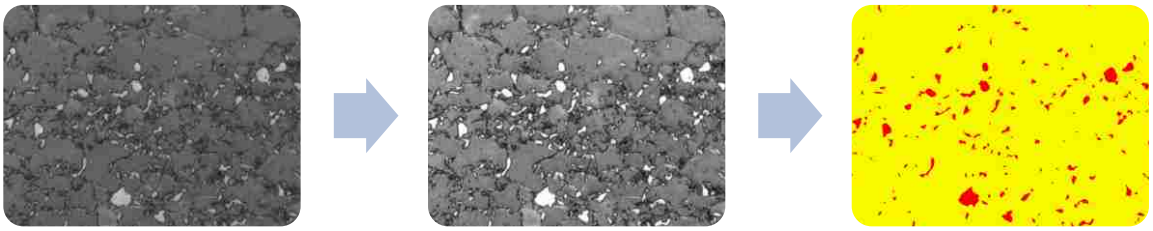

Figure 3-6 Analysis of a micrograph in image analysis software
original micrograph➔enhancement of contrast➔image analyzer

The results of the quantitative metallography which are required for micromechanical modeling are presented in Table 3-3. These data are obtained from the analysis of more than 1200 ferrite grains and 1900 martensite islands in DP500 steel and from 1500 ferrite grains, 1100 martensite islands and 300 bainite grains in DP600 steel. To evaluate the results, the 95% Confidence Intervals (95% CI) and Relative Accuracy percent (%RA) were calculated according to ASTM E112 [68]:

$$95\%CI = \pm \frac{t.s}{\sqrt{N}} \qquad 3\text{-}1$$

$$\%RA = \frac{95\%CI}{\bar{X}}.100 \qquad 3\text{-}2$$

where s is the standard deviation, N is the number of measured grains, $\bar{X}$ is the mean grain size, and t is a multiplier that is a function of N, in this case t = 1.960 for N>60. According to the standard, a %RA equal to or less than 10 is considered to be an acceptable precision for most purposes. The %RA is also reported for the quantitative data presented in Table 3-3. As it can be seen, all the %RA values are below 10% which guarantees the accuracy of the quantitative data.

Table 3-3 Statistical results of quantitative metallography of through-thickness microstructures of as-received DP500 and DP600

Steel	Parameter	Ferrite	Martensite	Bainite
DP500	Volume Fraction %	91.0	9.0	-
	Mean Aspect Ratio	-	1.85 (%RA=±1.8%)	
	Mean Grain Size [μm]	5.45 (%RA=±4.5%)	0.90 (%RA=±4.8%)	
DP600	Volume Fraction %	92.0	4.7	3.3
	Mean Aspect Ratio	-	1.78 (%RA=±1.6%)	1.87 (%RA=±1.1%)
	Mean Grain Size [μm]	4.0 (%RA=±8.0%)	0.56 (%RA=±3.4%)	2.42 (%RA=±4.3%)

In addition to the "mean grain size" of martensite islands in DP500 and DP600 steels, the "distribution of grain size" is required in micromechanical model to produce an appropriate RVE. These data are presented in Figure 3-7 and Figure 3-8 for martensite islands in DP500 and DP600 steels, respectively.

As it was mentioned in Section 2.4.2, the prior austenite mean grain size (austenite at the intercritical temperature), is needed to determine the flow behaviour of bainite in DP600 steel. The austenite mean grain size was provided for this research by ArcelorMittal Dofasco to be 2.56 μm. To determine the austenite mean grain size, the steel was quenched in an icy water bath from the intercritical annealing temperature; thus almost the entire austenite grains transformed into martensite. The mean grain size of martensite islands was determined according to ASTM E112 [68]. Since there is ≈4% volume increase in transformation of austenite to martensite [69], the mean grain size of martensite was reduced for 1.59% ($\sqrt[3]{4}$) to obtain the approximate austenite mean grain size.

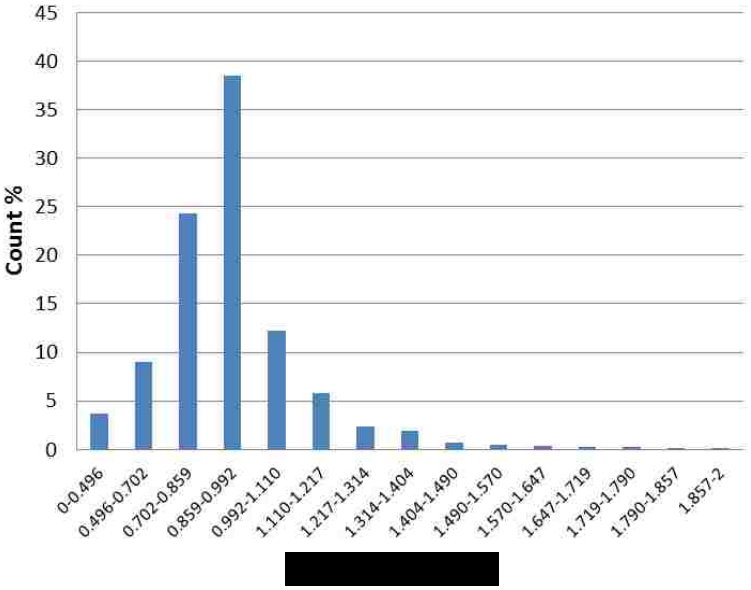

Size (µm)	%
0-0.496	0.0367
0.496-0.702	0.0905
0.702-0.859	0.2431
0.859-0.992	0.3854
0.992-1.110	0.1225
1.110-1.217	0.0579
1.217-1.314	0.0236
1.314-1.404	0.0193
1.404-1.490	0.0064
1.490-1.570	0.0047
1.570-1.647	0.0034
1.647-1.719	0.002
1.719-1.790	0.002
1.790-1.857	0.0017
1.857-2	0.0017

Figure 3-7 Distribution of grain size for martensite islands in the DP500 steel

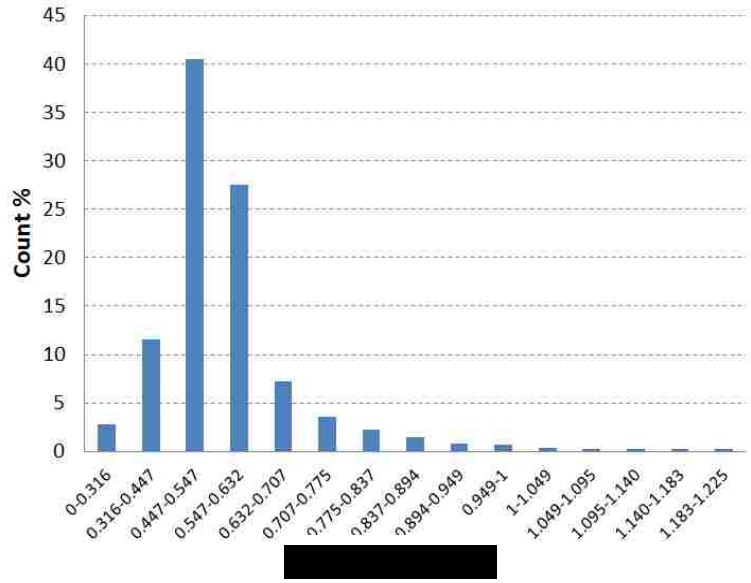

Size (µm)	%
0-0.316	0.028
0.316-0.447	0.1159
0.447-0.547	0.4051
0.547-0.632	0.2754
0.632-0.707	0.0725
0.707-0.775	0.035
0.775-0.837	0.0226
0.837-0.894	0.0143
0.894-0.949	0.0084
0.949-1	0.0067
1-1.049	0.0034
1.049-1.095	0.003
1.095-1.140	0.003
1.140-1.183	0.003
1.183-1.225	0.003

Figure 3-8 Distribution of grain size for martensite islands in the DP600 steel

3.2 Distribution of Alloying Elements in the Microstructure

Substitutional solid solution hardening has an important role in micromechanical behaviour of materials. As it was mentioned in Section 2.4.2, σ_0 (solid solution hardening in the microstructure) can be calculated using Equation **2-6**, only if alloying elements are distributed homogeneously in the microstructure.

As it indicated in Table 3-1, Mn for DP500 steel and Mn, Mo, Cr, and Si for DP600 steel are the main alloying elements with amounts greater than 0.1 wt%. Distribution of the main alloying elements in the through-thickness microstructures were investigated using Energy Dispersive Spectroscopy (EDS) analysis to understand if there was a notable elemental segregation inside the ferrite grains, bainite grains or martensite islands. A field emission scanning electron microscope FEI Quanta 200 FEG equipped with an EDAX energy dispersive spectrometer was utilized for the EDS analysis. A voltage of 30 kV and a dwell time of 800 μs was applied.

Results are presented in Figure 3-9 to Figure 3-13. According to these results, no notable segregation is observable inside each individual constituent. Hence, it can be concluded that the main substitutional alloying elements are distributed approximately homogeneously within the ferrite grains, bainite grains and martensite islands. This means that the mechanical properties of each individual grain can be considered uniform throughout the whole grain and Equation **2-6** can be used to determine the flow stress of each of the ferrite, martensite and bainite phases.

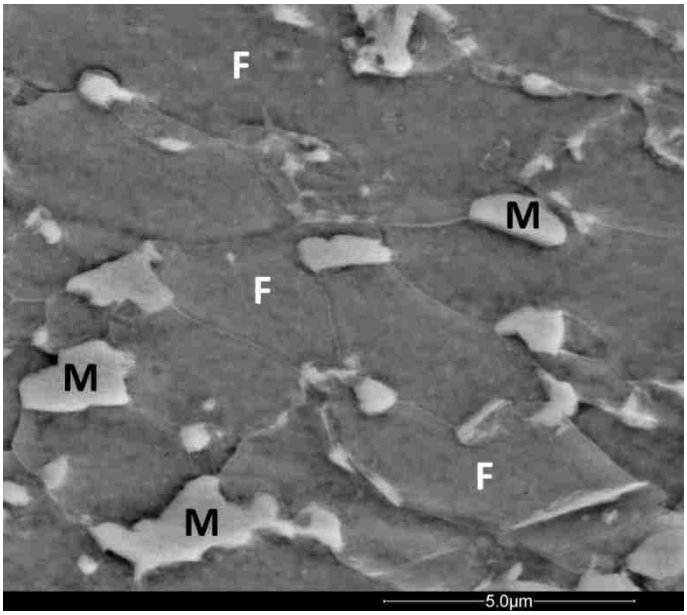

F: ferrite, M: martensite

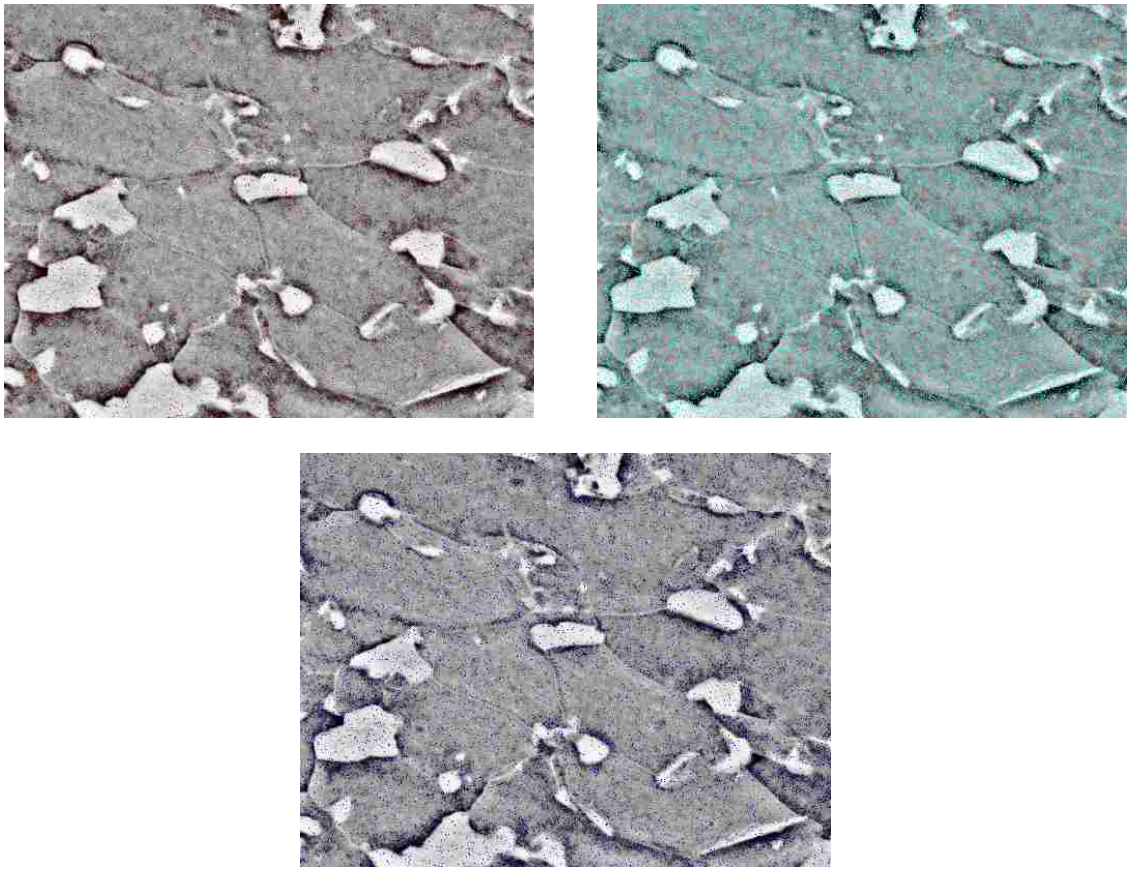

Figure 3-9 EDS maps and distribution of Mn (red), Cr (turquoise) and Si (blue) in a through-thickness microstructure of DP500 steel.

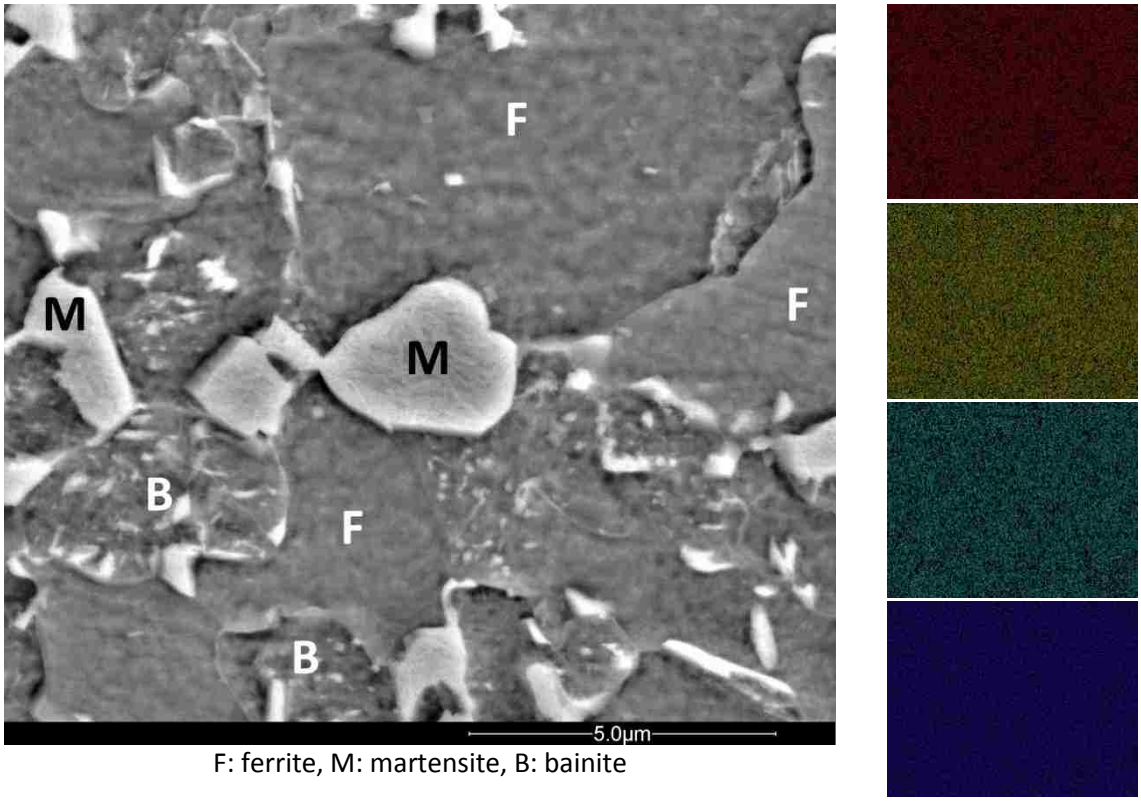

F: ferrite, M: martensite, B: bainite

Figure 3-10 EDS maps and distribution of Mn (red), Mo (yellow), Cr (turquoise) and Si (blue) in a through-thickness microstructure of DP600 steel close to the surface of the sheet.

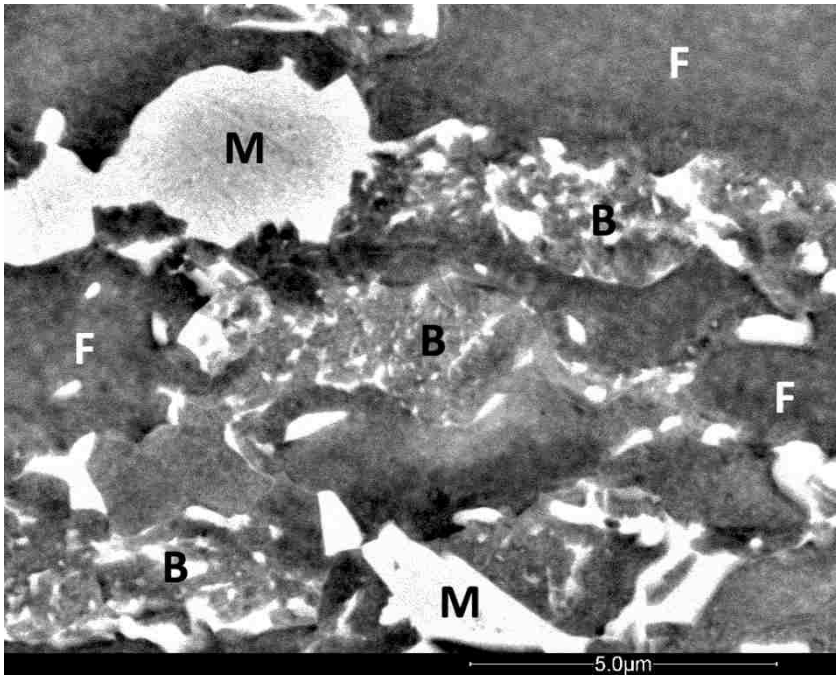

F: ferrite, M: martensite, B: bainite

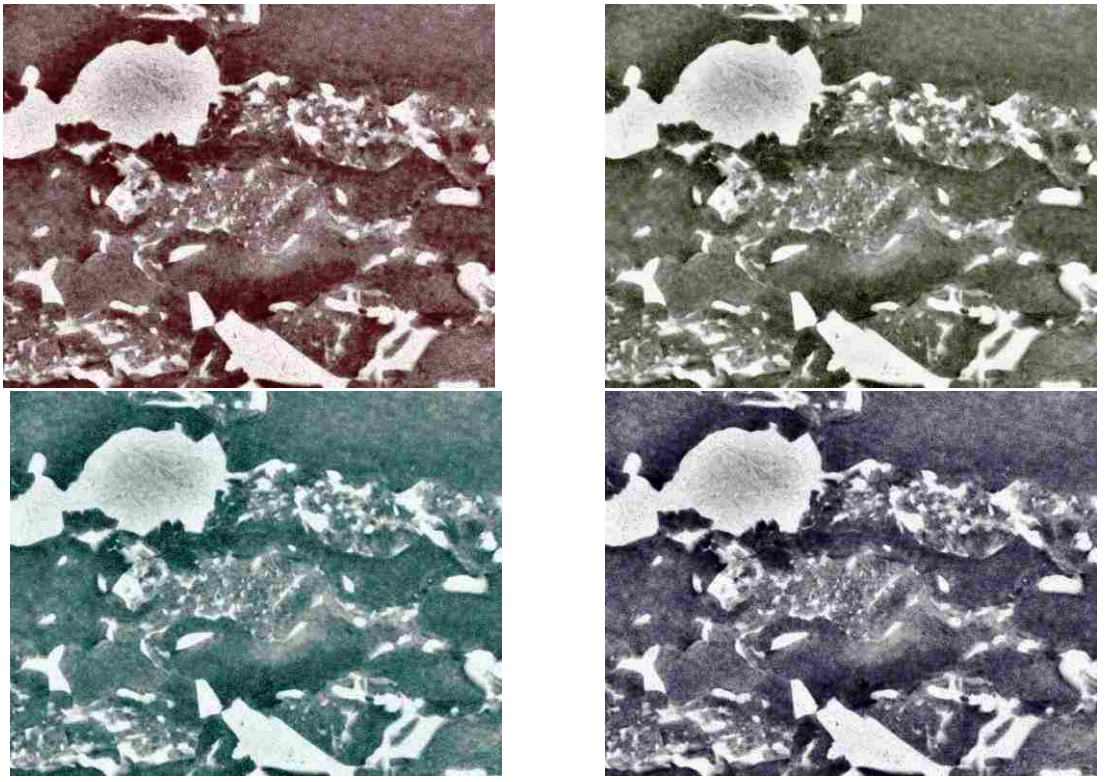

Figure 3-11 EDS maps and distribution of Mn (red), Mo (yellow), Cr (turquoise) and Si (blue) in a through-thickness microstructure of DP600 steel near the centre of the sheet.

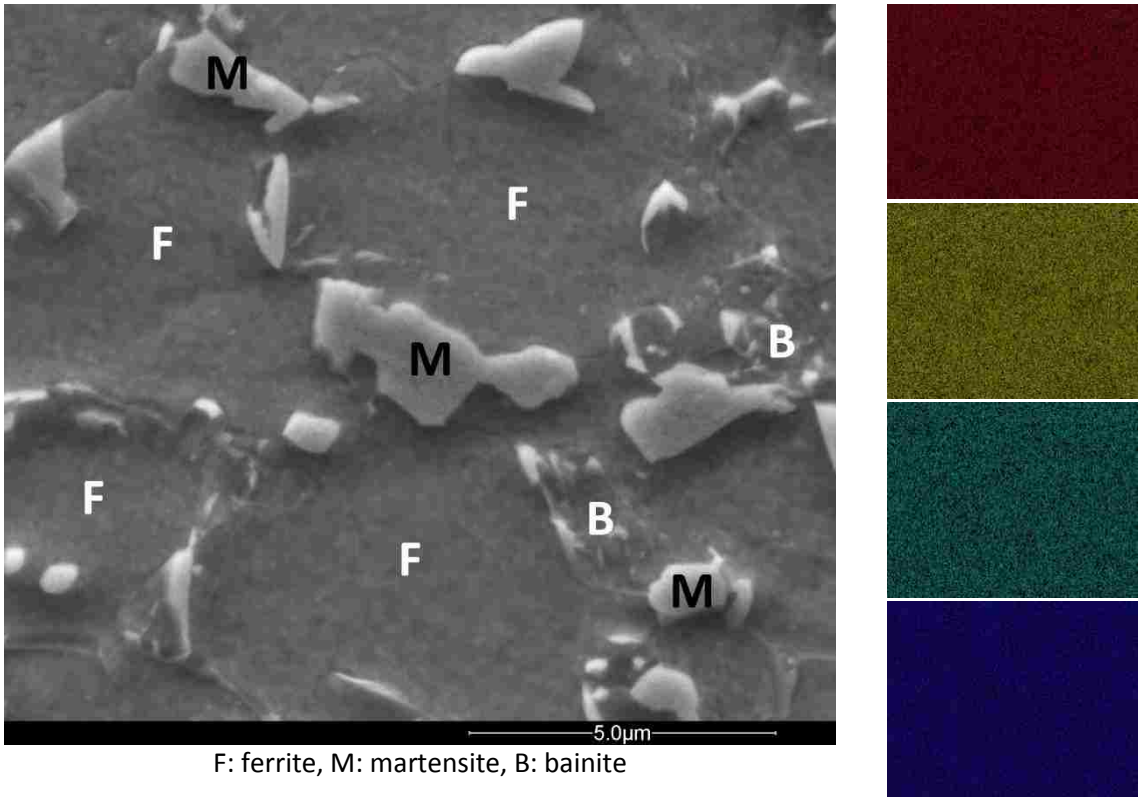

F: ferrite, M: martensite, B: bainite

Figure 3-12 EDS maps and distribution of Mn (red), Mo (yellow), Cr (turquoise) and Si (blue) in a through-thickness microstructure of DP600 steel near the centre of the sheet.

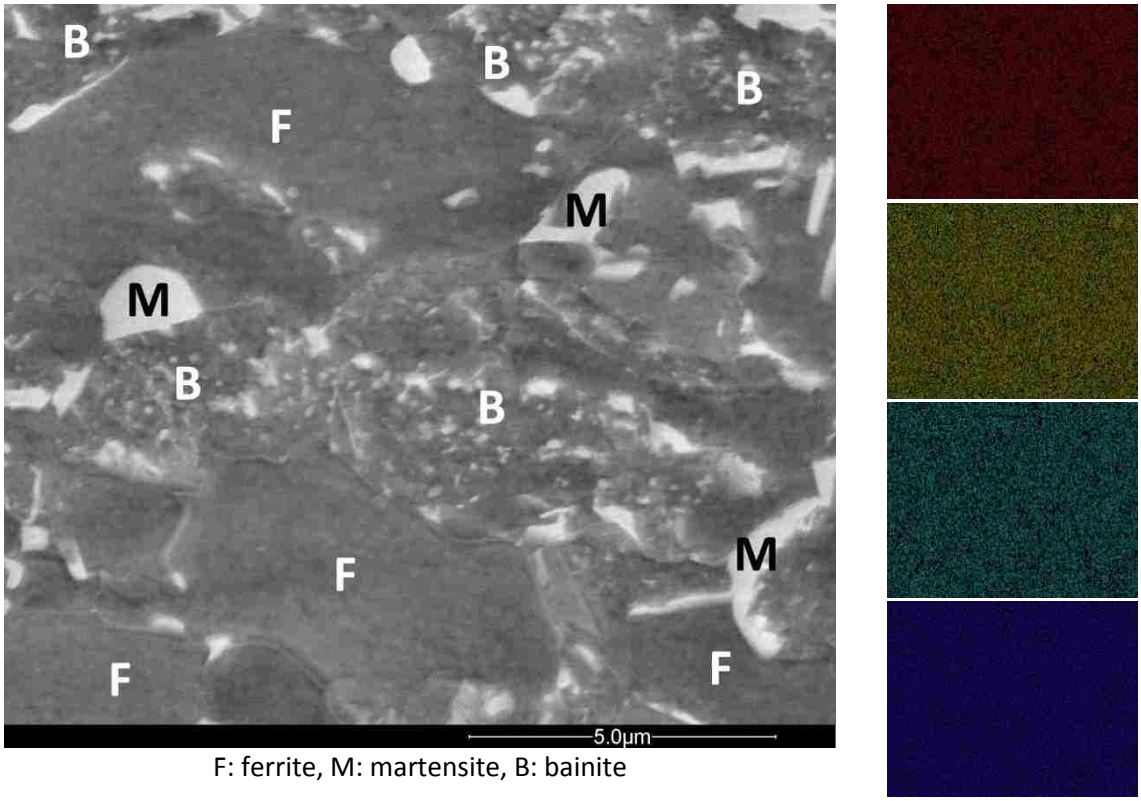

F: ferrite, M: martensite, B: bainite

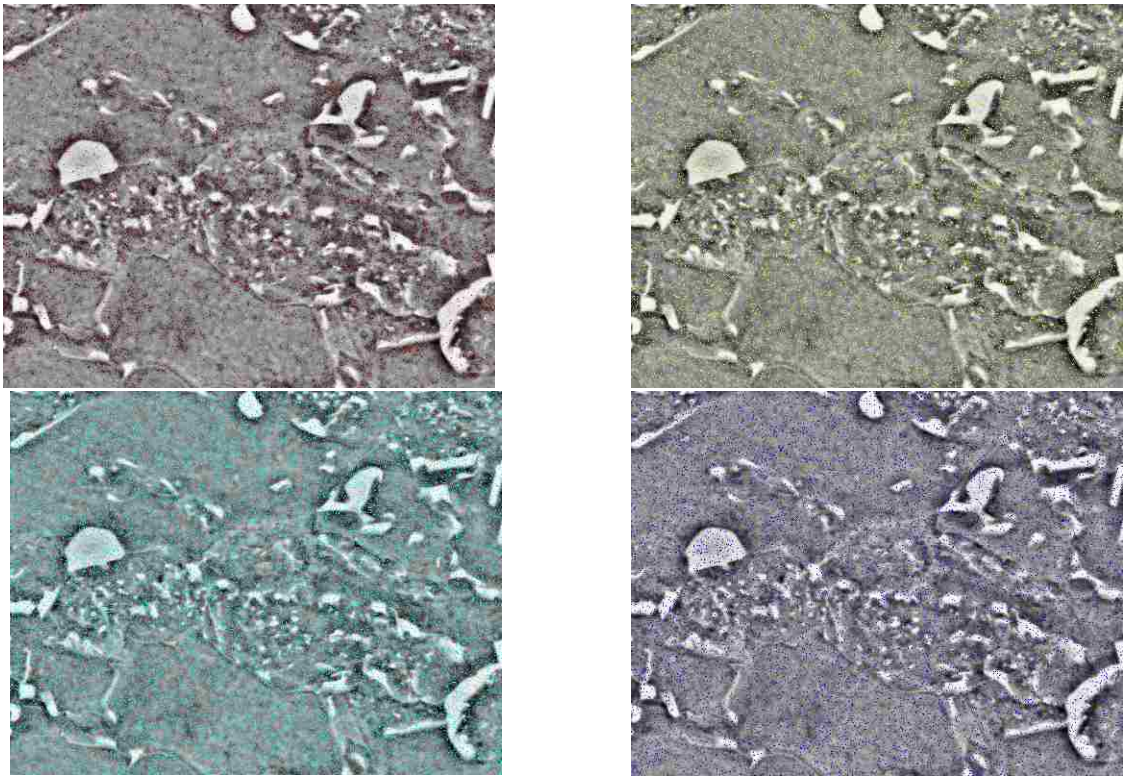

Figure 3-13 EDS maps and distribution of Mn (red), Mo (yellow), Cr (turquoise) and Si (blue) in a through-thickness microstructure of DP600 steel near the centre of the sheet.

3.3 Distribution of Carbon in Ferrite, Bainite and Martensite

Carbon interstitial solid solution hardening has a significant role in strengthening steels. As it was mentioned in Section 2.4.2, $\Delta\sigma_c$ (carbon solution hardening in the microstructure) for ferrite, martensite, and bainite can be calculated using Equations **2-11**, **2-12** and **2-13**. For this purpose, the carbon content wt% in the constituents should be determined.

Due to the small amounts of carbon in both DP500 and DP600 steels, quantitative EDS could not accurately measure the amounts of carbon in ferrite grains, bainite grains and martensite islands. Hence, a thermodynamic simulation was carried out at CANMET Materials, Hamilton, ON, using the Thermo-Calc software. The database TCFE7 was used for simulation. The amounts of carbon in ferrite, martensite and bainite phases at the intercritical annealing temperature were obtained and are shown in Table 3-4.

Table 3-4 Carbon wt% in ferrite, martensite and bainite in DP500 and DP600 steels

	Ferrite	**Martensite**	**Bainite**
DP500	0.007	0.265	-
DP600	0.006	0.116	0.087

3.4 Strengthening Mechanisms and Flow Curves of DP500 and DP600 Steels

Standard tensile tests were carried out according to ASTM E8/E8M [70]. The corresponding true flow curves of DP500 and DP600 steels are presented in Figure 3-14 and Figure 3-15, respectively. As it was mentioned in Section 2.3, dual phase steels present continuous yielding due to the existence of mobile dislocations near the ferrite and martensite interface. However, there is only 4.7 vol% of martensite in the microstructure of this DP600 steel. Hence, the amount of existing mobile dislocations is not sufficient to see a smooth transition from elastic to plastic deformation and prevent the yielding phenomenon.

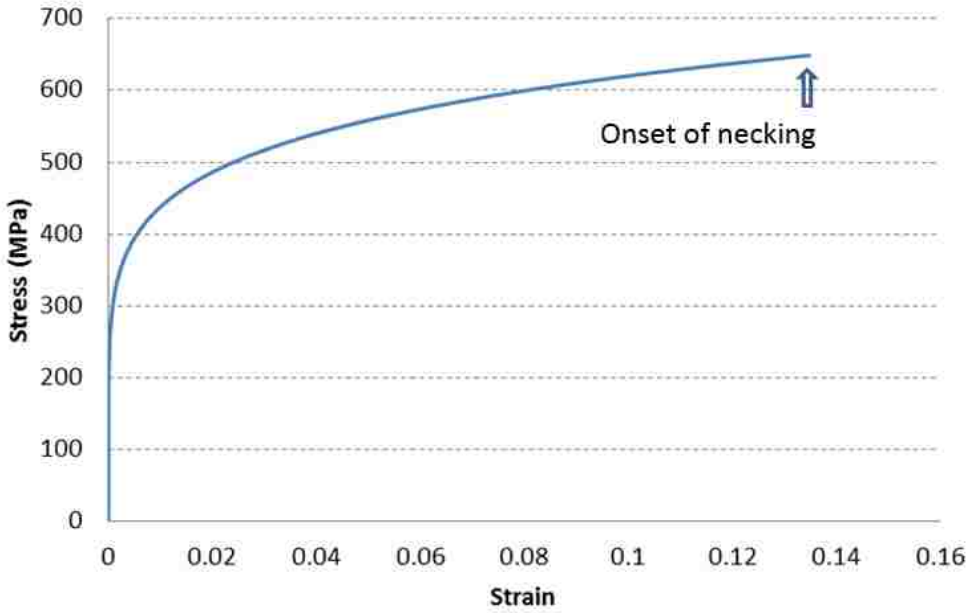

Figure 3-14 The true flow curve of DP500 steel

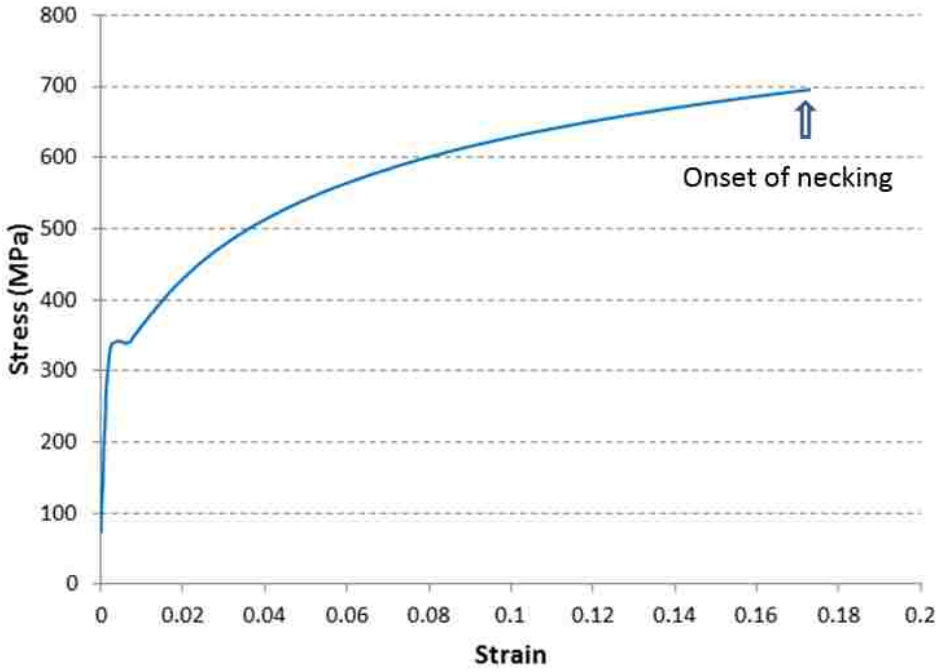

Figure 3-15 The true flow curve of DP600 steel

The strengthening parameters in DP500 and DP600 steels are indicated in Table 3-5. As can be seen, strengthening of DP500 steel compared to DP600 steel is based on the martensite strengthening. Although the required ultimate tensile stress in DP600 steel is greater than that in DP500 steel, it only includes 4.7 vol% of martensite. However, solid solution hardening in DP600 steel is stronger than DP500 steel due to the presence of more carbon and alloying elements in the microstructure of DP600 steel. Also, the mean ferrite grain size in the DP600 steel is smaller than that of the DP500 steel which provides more grain size strengthening in the DP600 steel according to the Hall-Petch equation (Equation 2-1). Furthermore, the existence of bainite in the microstructure of DP600 steel increases the strength of the steel; however, it cannot be considered as a major strengthening mechanism. The major effect of bainite is to enhance the combination of strength-ductility in dual phase steels [71]. The combinations of strengthening mechanisms in the DP500 and DP600 steels result in a better combination of strength-ductility in the DP600 steel; this can also be seen by comparing the flow curves of DP500 and DP600 steels in Figure 3-14 and Figure 3-15. The martensite strengthening used in DP500 steel is the most influential strengthening mechanism in dual phase steels; however, it notably reduces the elongation of the steel. On the other hand, the small amount of martensite in DP600 steel results in yield point phenomenon followed by Lüders bands which undesirably affects the surface quality of sheet metal after yielding.

Table 3-5 Strengthening parameters in DP500 and DP600 steels

	Carbon	**Alloying Elements**	**Mean Ferrite Grain Size (Through-thickness)**	**Martensite Content**	**Bainite Content**
DP500	0.063 wt%	≈1.90 wt%	5.45 µm	9.0 vol%	-
DP600	0.107 wt%	≈2.21 wt%	4.0 µm	4.7 vol%	3.3 vol%

3.5 Void Analysis

The focus of this research is the micromechanical modeling of flow curves of DP500 and DP600 steels in the range of uniform deformation before the onset of necking. However, localization of plastic deformation occurs in the microstructure even at low macroscopic plastic strains. As a result, microstructural damage such as nucleation of void does occur in the microstructure.

Equation **2-10** considers ferrite, martensite and bainite as continuum media and determines their flow behaviour. However, the nucleation and growth of voids in the microstructure specifically in the martensite phase lead to discontinuities in the microstructure. Hence, the nucleation and growth of voids was quantitatively investigated in order to estimate the possible level error in the modeling results.

In order to determine the content of voids in the microstructures of DP500 and DP600 steels, as-polished samples were slightly etched for 2-3 s just to remove the polished layer but not to etch the microstructure. Hence, voids were identified as dark spots in a white matrix. Figure 3-16 shows the voids in the through-thickness microstructures of the steels deformed by the standard uniaxial tensile test close to the necking area. Void area fraction was determined in the microstructures according to:

$$Void\,Area\,Fraction\% = \frac{Number\,of\,Black\,Pixels}{Total\,Number\,of\,Pixels} \times 100 \qquad 3\text{-}3$$

As it was shown in Figure 3-14 and Figure 3-15 necking occurred in DP500 and DP600 steels at effective strains of ≈0.14 and ≈0.16, respectively. Quantitative analysis of voids was carried out close to the necking points where the greatest amounts of voids were found. Results showed that the void area fractions in DP500 and DP600 steels were only 0.18 and 0.12%. Hence, the effect of voids on the flow behaviour of ferrite, martensite and bainite was ignored.

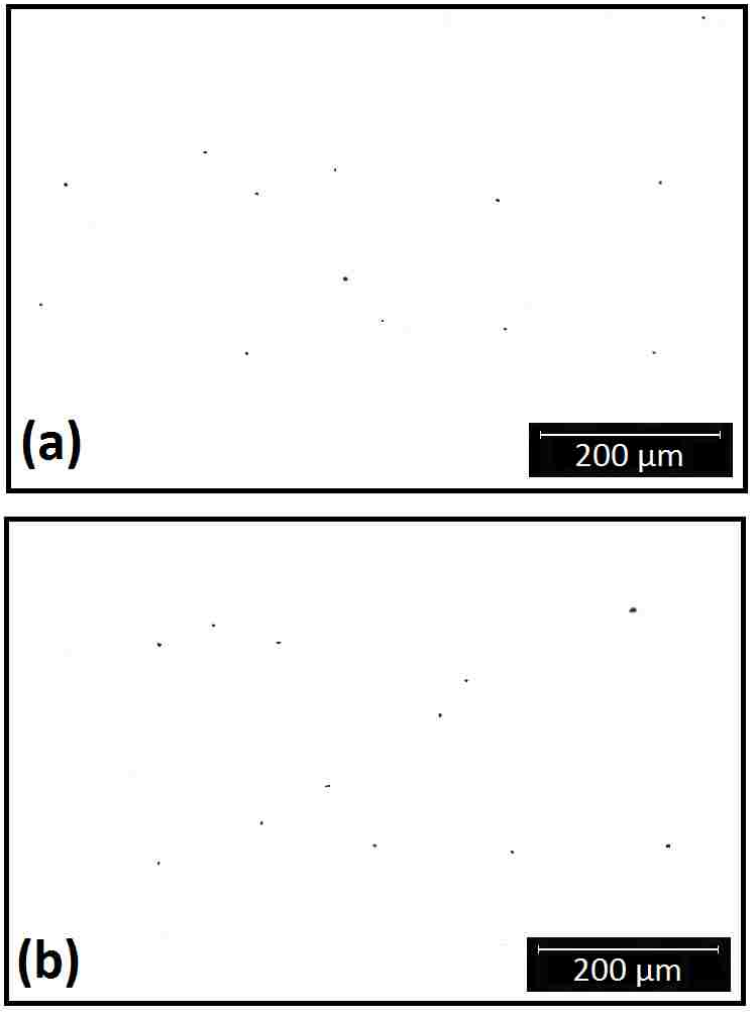

Figure 3-16 Voids in the through-thickness microstructures of (a) DP500 and (b) DP600 steels close to the necking area deformed by the standard uniaxial tensile test.

4 Modeling Procedure and Methodology

In this research, micromechanical modeling of flow behaviour of DP500 and DP600 steels was carried out using the RVE method. The dual phase steels were considered as composite materials: ferrite as the matrix and martensite islands as hard particles (inclusions). As mentioned in Section 2.5, Uthaisangsuk et al [35], Thomser et al [36], Ramazani et al [40] and Al Abbasi et al [63] reported that 2D micromechanical models underestimate the flow behaviour of dual phase steels. Hence, in this research, 3D modeling was carried out to obtain more accurate results. The effects of RVE size and mesh refinement were also investigated and are reported in this research.

The entire modeling procedure was performed using MATLAB, Digimat and ABAQUS software. MATLAB and ABAQUS are well-known commercial software. Digimat software is described in Sections 4.2 to 4.6. Micromechanical modeling of flow behaviour of DP500 and DP600 steels was carried out in six steps:

Step 1 Calculation of flow curves of constituents in MATLAB

Step 2 Introducing the flow behaviour of constituents to Digimat-FE

Step 3 RVE generation in Digimat-FE

Step 4 Definition of loading and boundary conditions in Digimat-FE

Step 5 Simulating the loading in ABAQUS and obtaining the flow curve of the RVE in Digimat-FE

Step 6 Homogenization in Digimat-MF

These steps are illustrated in the following.

4.1 Calculation of Flow Behaviour of Constituents

The flow behaviour of ferrite, martensite and bainite were determined according to:

$$\sigma_0 = 77 + 80\%Mn + 750\%P + 60\%Si + 80\%Cu + 45\%Ni + 60\%Cr + 11\%Mo + 5000N_{ss} \quad \text{2-6 (repeated)}$$

$$\sigma = \sigma_0 + \Delta\sigma_c + \alpha \times M \times \mu \times \sqrt{b} \times \sqrt{\frac{1-\exp(-Mk_r\varepsilon)}{k_r \times L}} \quad \text{2-10 (repeated)}$$

$$\Delta\sigma_c^f = 5000 \times (\%C_{SS}^f) \quad \text{2-11 (repeated)}$$

$$\Delta\sigma_c^m = 3065 \times (\%C_{SS}^m) - 161 \quad \text{42-12 (repeated)}$$

$$\Delta\sigma_c^b = \Delta\sigma_c^f V_f + \Delta\sigma_c^m V_m \quad \text{2-13 (repeated)}$$

The required parameters in the above equations for ferrite, martensite and bainite in DP500 and DP600 steels were presented in Table 2-1, Table 3-1, Table 3-3 and Table 3-4. Calculations are presented in Appendices A1-A5. Hence, the constitutive equations of the constituents are:

Ferrite in DP500 Steel

$$\sigma = 261.96 + 1.25\sqrt{\frac{1-\exp(-5.41\varepsilon)}{10^{-5}}} \quad \text{4-1}$$

Martensite in DP500 Steel

$$\sigma = 878.19 + 1.25\sqrt{\frac{1-\exp(-123\varepsilon)}{10^{-5}}} \quad \text{4-2}$$

Ferrite in DP600 Steel

$$\sigma = 225.71 + 1.25\sqrt{\frac{1-\exp(-7.5\varepsilon)}{10^{-5}}} \quad \text{4-3}$$

Martensite in DP600 Steel

$$\sigma = 420.25 + 1.25\sqrt{\frac{1-\exp(-123\varepsilon)}{1.56\times10^{-6}}} \quad \text{4-4}$$

Bainite in DP600 Steel

$$\sigma = 262.45 + 1.25\sqrt{\frac{1-\exp(-11.72\varepsilon)}{7.81\times10^{-7}}} \quad \text{4-5}$$

Since necking occurred in DP500 and DP600 steels approximately at strains of 0.14 and 0.16, respectively, flow curves of the softer constituents were considered up to strains of 0.15 and 0.20 in DP500 and DP600 steels, respectively. Martensite is reported to behave elastically before necking [72]; however, martensite plasticity is possible in case of strain localization in the microstructure. Hence, the flow curves of martensite in DP500 and DP600 steels were considered up to a strain of 0.015.

It is assumed that the work hardening behaviour of ferrite, martensite and bainite follow the Holloman power-law equation [73]:

$$\sigma = K\varepsilon^{n} \qquad 4\text{-}6$$

where K and n are the hardening modulus and hardening exponent, respectively. Hence, the Curve Fitting application in MATLAB software was used to fit power-law equations to the predicted σ(ε) curves of the constituents to determine the hardening modulus and hardening exponent of the ferrite, martensite and bainite in the DP500 and DP600 steels. Figure 4-1 and Figure 4-2 show the analytical and fitted flow curves obtained for the constituents of DP500 and DP600 steels, respectively. In these figures, coefficients a and b are the values of K and n, respectively.

In case of DP600 steel, if the combination of ferrite (92.0%) and bainite (3.3%) is considered as the matrix and only martensite islands (4.7%) as inclusions, the flow curve of the matrix can be determined by the mixture rule:

$$\sigma(\varepsilon) = \frac{92\times\sigma_f(\varepsilon_f) + 3.3\times\sigma_b(\varepsilon_b)}{92+3.3} = 0.965\times\sigma_f(\varepsilon_f) + 0.035\times\sigma_b(\varepsilon_b) \qquad 4\text{-}7$$

The analytical and fitted flow curve of the new matrix is shown in Figure 4-3.

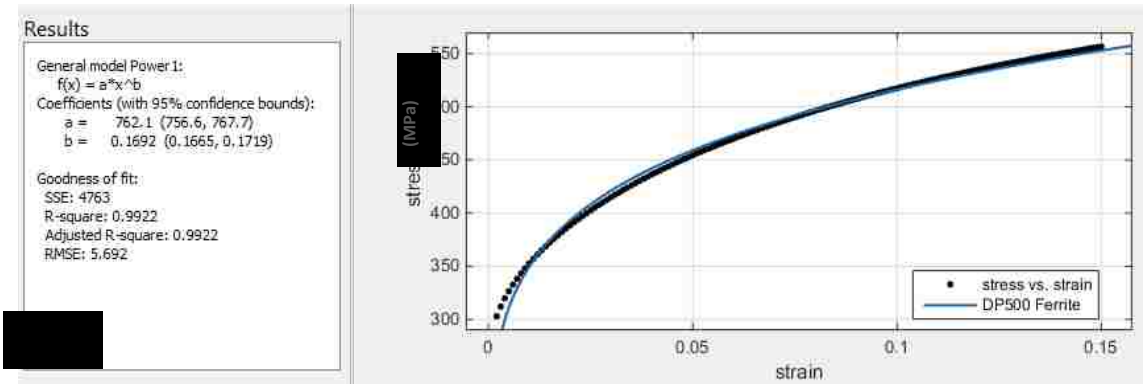

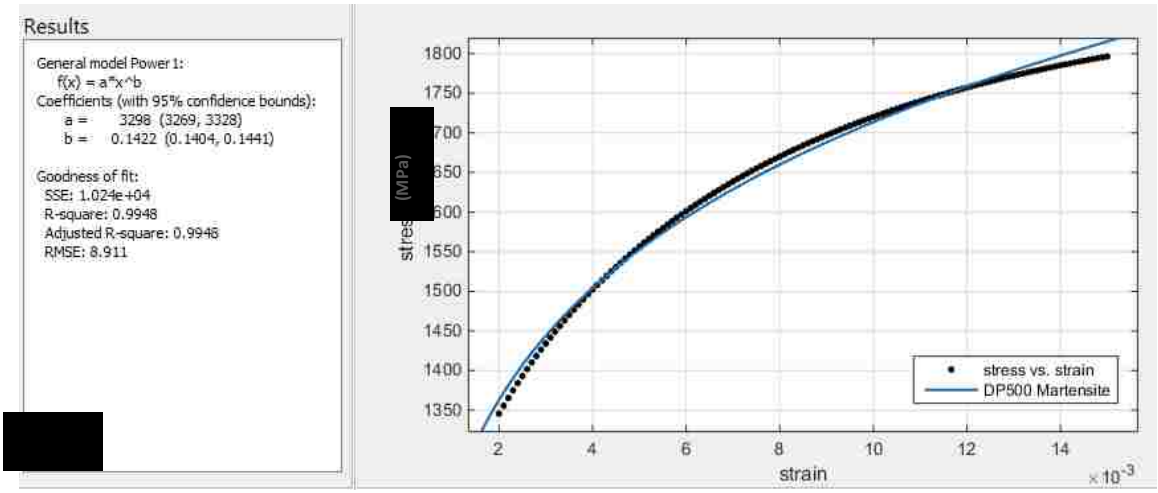

Figure 4-1 Analytical flow curves of (a) ferrite and (b) martensite in DP500 steel

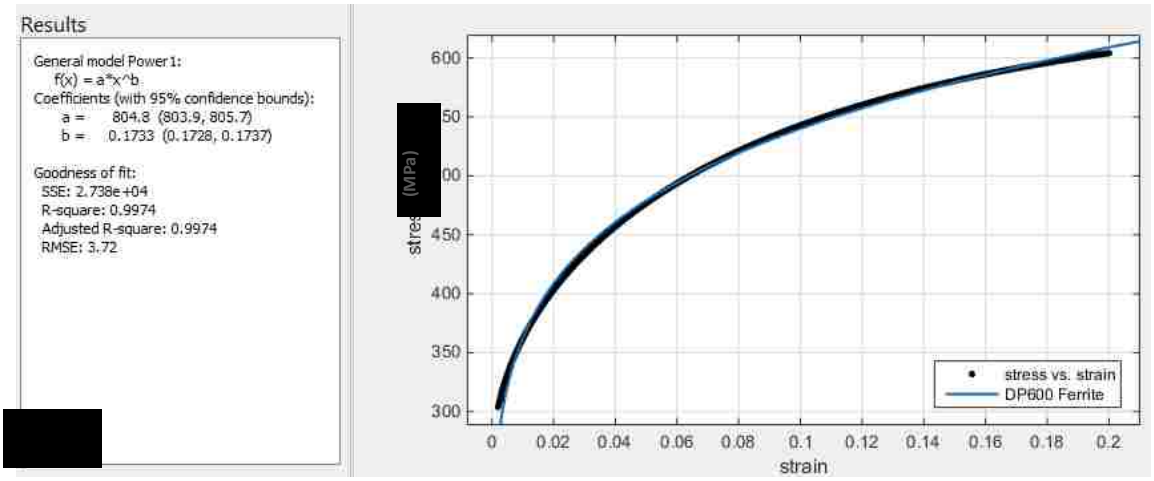

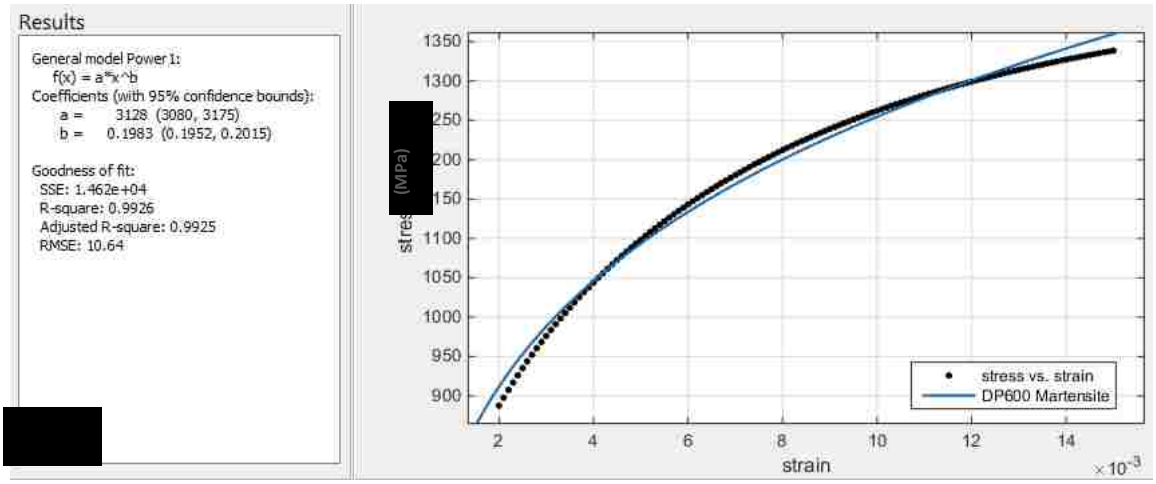

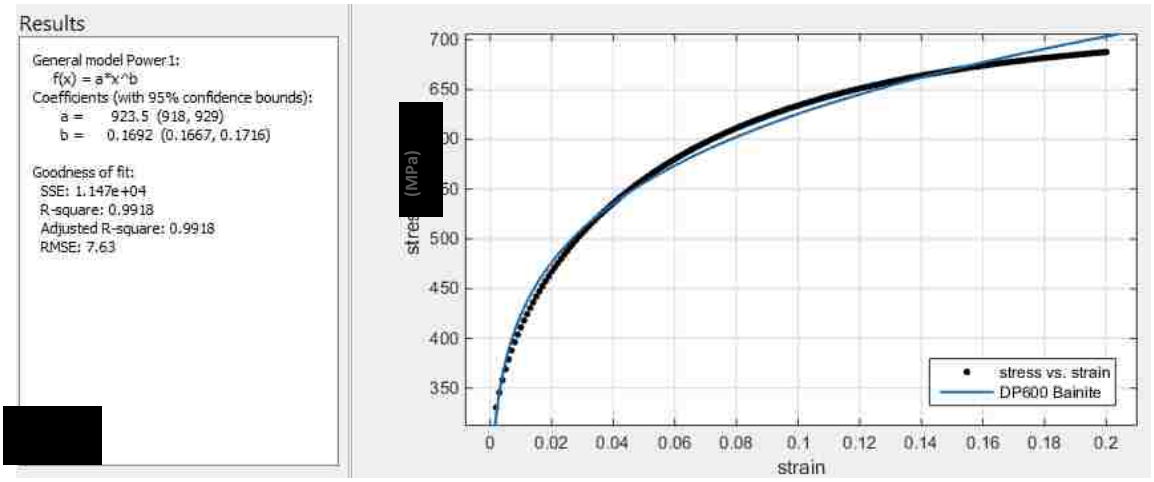

Figure 4-2 Analytical flow curves of (a) ferrite, (b) martensite and (c) bainite in DP600 steel

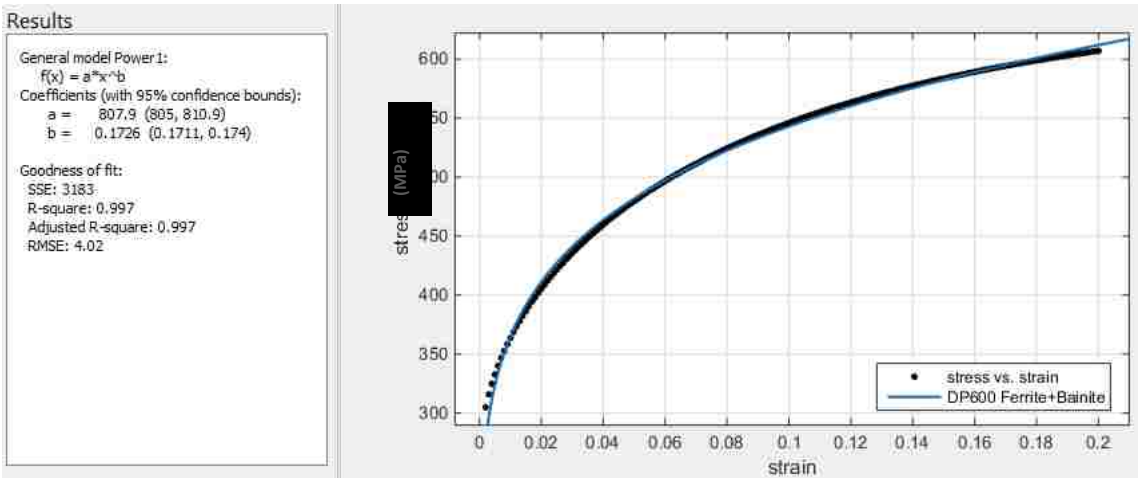

Figure 4-3 Analytical flow curve of combination of ferrite and bainite

4.2 Introducing the flow behaviour of constituents to Digimat-FE

Micromechanical modeling of materials in Digimat software starts from the Digimat-FE module. As it is shown in Figure 4-4, this module includes five steps: Materials, Microstructures, RVE, Loadings and Results.

In the first step (i-e. the “Materials” step) the mechanical properties of ferrite, martensite and bainite including Young’s modulus, Poisson’s ratio, yield stress, hardening modulus and hardening exponent are introduced to the software. Young’s modulus and Poisson’s ratio for all the constituents were considered to be 210 GPa and 0.33, respectively. The flow stress at ε=0.002 was introduced as the yield stress. The hardening modulus and hardening exponent were taken from Section 4.1.

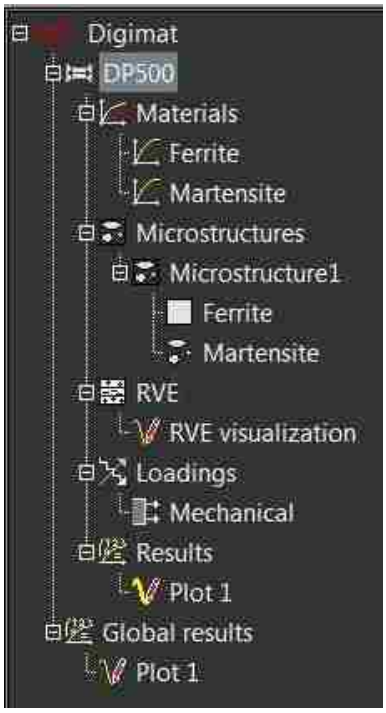

Figure 4-4 Digimat-FE analysis tree

4.3 RVE Generation in Digimat-FE

In this step, for DP500 steel, the ferrite alone is designated as the “matrix” and martensite as “inclusions”. For DP600 ferrite and bainite together are designated as the “matrix” and martensite as “inclusions”. Also, the combination of ferrite and bainite can be introduced as matrix. Since this research does not model the microstructural damage, the interface between the matrix and inclusion are defined as “perfectly bonded”. As is shown in Figure 4-5, after determining the “phase fraction” of each inclusion, there are three options for “phase definition” in the RVE:

(1) “number of inclusions” and “aspect ratio”,

(2) “inclusion size” and “aspect ratio” and

(3) “inclusion size” and “diameter”.

The “inclusion size” can be defined as constant or according to uniform distribution (min and max size), normal distribution (mean and variance) or user defined. In case of user defined, a histogram of the size distributions can be supplied in a text file with a certain format and introduced to the Digimat software. Furthermore, the shape of the inclusions can be determined as ellipsoid, cylinder and prism.

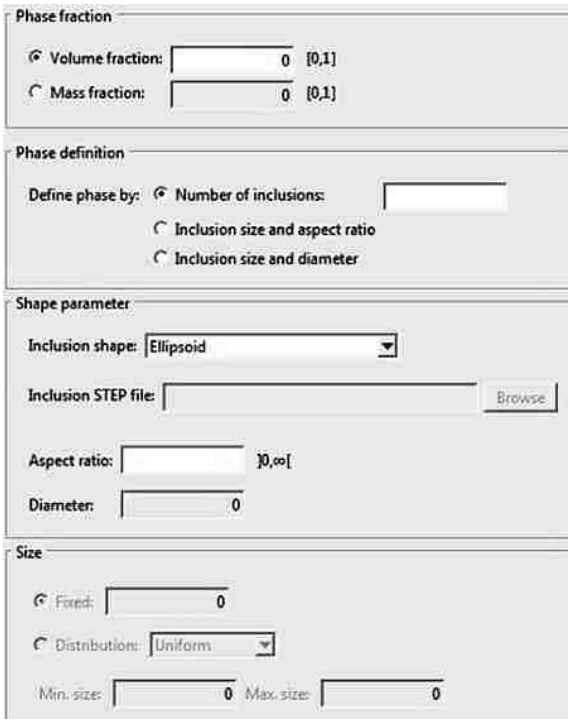

Figure 4-5 Determination of morphological parameters of the inclusion phases in Digimat-FE.

In this work, inclusions were introduced to the Digimat-FE using the “inclusion size” and “aspect ratio” method. The actual inclusion size was uploaded in the Digimat-FE using a text file including the size distribution histogram of martensite islands which were shown in Figure 3-7 and Figure 3-8. According to the quantitative metallography results presented in Section 3.1, the closest inclusion shape to the martensite shape is the ellipsoid. Hence, as indicated in Table 3-3, martensite islands in the microstructures of DP500 and DP600 steels were considered as ellipsoids with aspect ratios of 1.87 and 1.78, respectively.

After defining the morphological features of the microstructure, a random 2D or 3D RVE can be generated. As it is shown in Figure 4-6, the generated RVE is visualized under the “RVE visualization" tab. The information regarding the calculation time and phase information, e.g. inclusion numbers in the RVE and effective volume fraction of the inclusion(s), is presented under the “RVE global data” tab shown in Figure 4-7. More details about generated RVE are found in the “RVE phase data” tab which is presented in Figure 4-8. The RVE size should be sufficiently large to include a sufficient number of inclusions inside the RVE otherwise their size distribution will not correspond with that of the inclusions in the real microstructure.

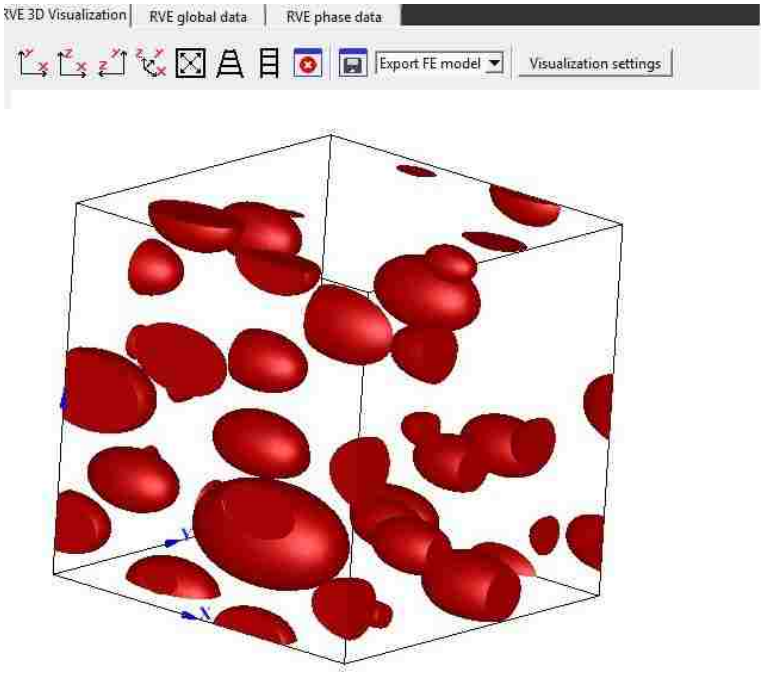

Figure 4-6 RVE generation in Digimat-FE: “RVE visualization” tab

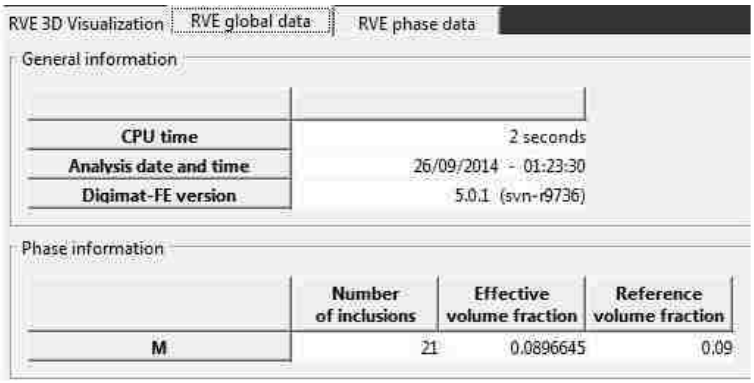

Figure 4-7 RVE information in Digimat-FE: “RVE global data” tab

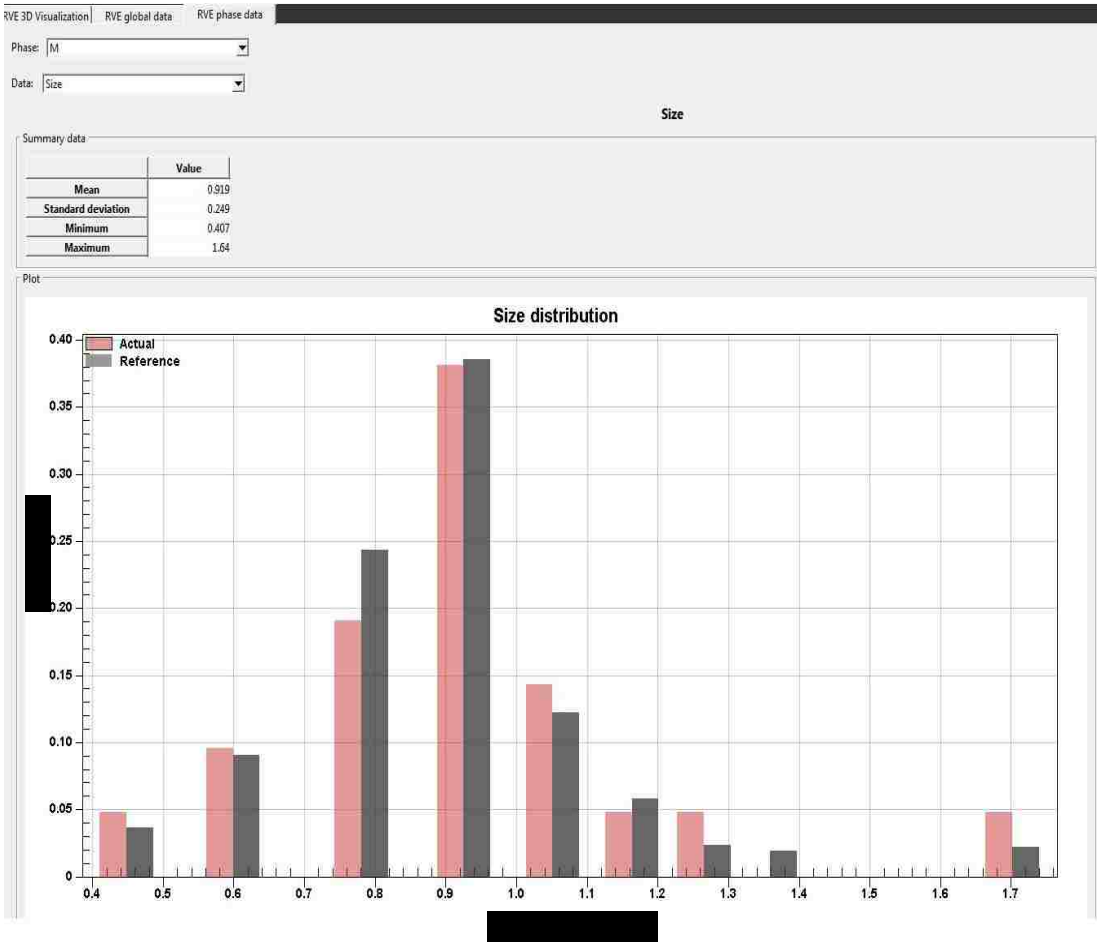

Figure 4-8 RVE information in Digimat-FE: “RVE phase data” tab

4.4 Definition of Loadings and Boundary Conditions in the Digimat-FE

The type of loadings and applied boundary condition should be defined in this step. As is shown in Figure 4-9(a), the type of boundary condition and loading can be defined in the "Mechanical loading" tab. Uniaxial tension, biaxial tension and shear in different directions can be selected. Also, it is possible to define cyclic or user-defined loadings. As can be seen in Figure 4-9(b), the initial and peak strain values of strain can be determined in the "Parameters" tab. Furthermore, it is possible to define a quasi-static loading or to select a strain rate for the applied load.

In this research, the periodic boundary condition was chosen as indicated in Section 2.4.3. Quasi-static uniaxial loading was applied and the peak strain value was determined as that at the onset of necking in DP500 and DP600 steels.

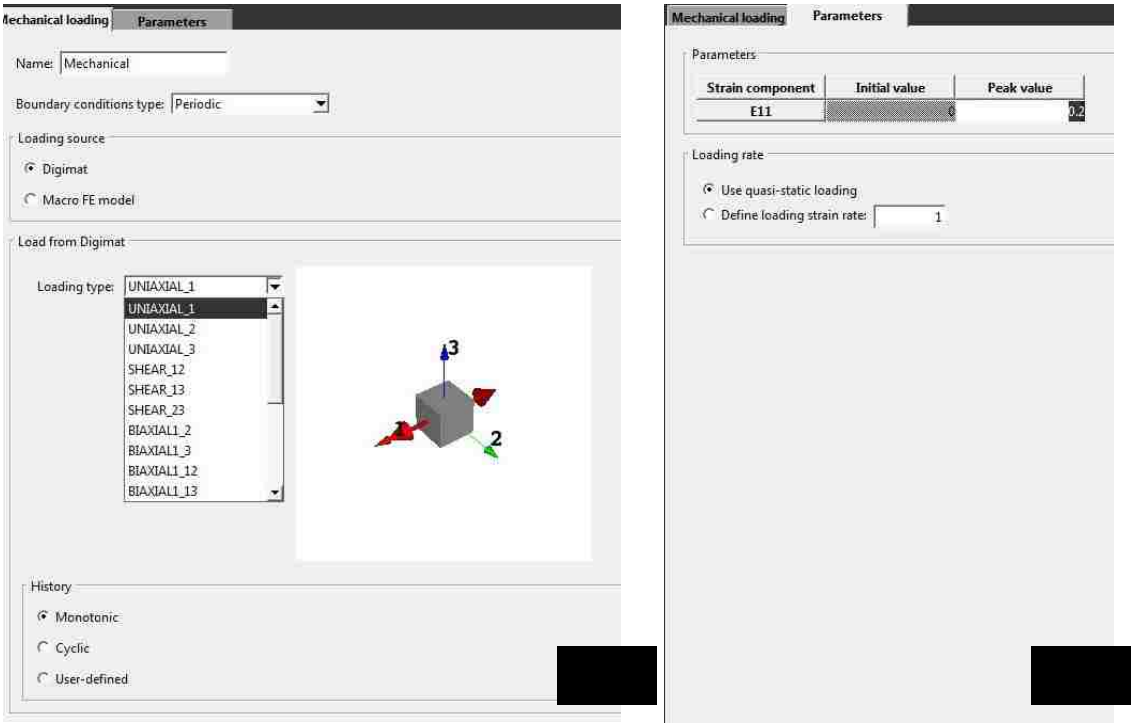

Figure 4-9 Definition of loading Digimat-FE loadings stage, a) definition of mechanical loading and boundary condition, b) definition of loading parameters.

4.5 Solving the Problem in ABAQUS and Obtaining the Flow Curve of RVE in Digimat-FE

After the loading type and boundary condition, the time step parameters, meshing settings etc. are defined in Digimat-FE, as indicated by the parameters input window in Figure 4-10. If Digimat and ABAQUS are coupled properly, the complete RVE model automatically appears in ABAQUS after it is exported. The problem is submitted in Job module in ABAQUS, and following the simulation of the tensile test, the flow behaviour of RVE is determined.

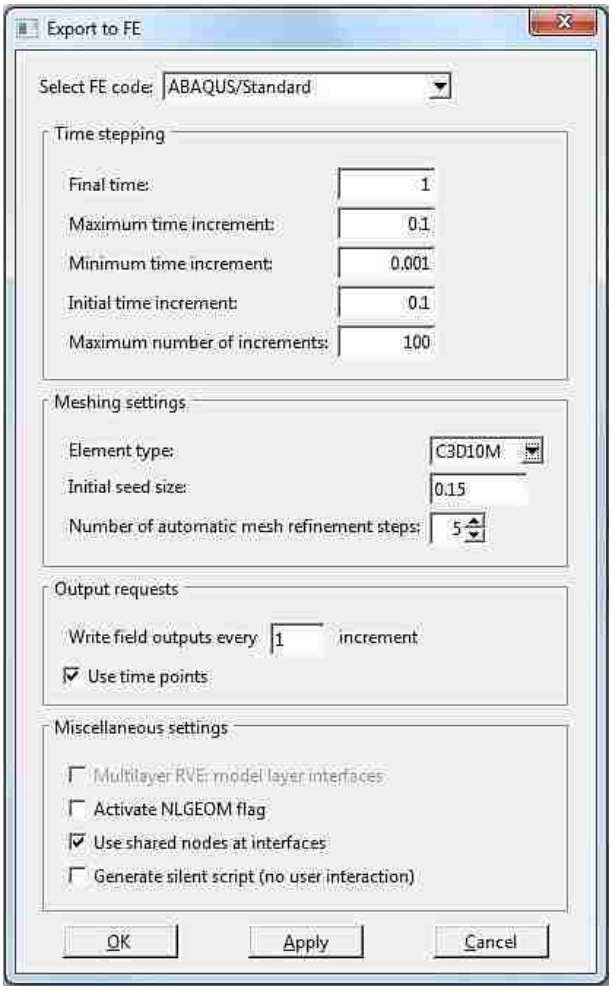

Figure 4-10 Determination of solving parameters in Digimat-FE and exporting the finite element problem to ABAQUS

Ramazani et al [40] used C3D4 elements for simulations using 3D RVEs. The element types C3D4 and C3D10 were also used for finite element analysis of 3D RVEs generated in this work. Initial seed sizes of 0.025, 0.05 and 0.075 were applied to investigate the effect of mesh size on the results.

After solving the problem in ABAQUS, post-processing analysis is carried out in Digimat-FE. This step is performed in the "Result" section in the Digimat-FE analysis tree presented in Figure 4-4. The flow curve of the RVE is the result of this step.

4.6 Homogenization in Digimat-MF

As indicated in Section 2.4.4, homogenization is carried out to relate the micro-scale flow curve of the RVE to the macro-scale flow curve of the whole material. After solving the problem in ABAQUS and post-processing in Digimat-FE to obtain the flow curve of the RVE, homogenization is performed in Digimat-MF.

Digimat-MF uses the mean-field homogenization method with the aim of predicting nonlinear constitutive behaviour of multi-phase materials. This prediction is based on the constitutive properties of each constituent and the morphology of the inclusions.

As it is shown in Figure 4-11(a), the analysis type and the homogenization technique are chosen in Digimat-MF in "General parameters" tab. Mechanical analysis and first order homogenization were applied in this research. Integration parameters are also defined in Digimat-MF. As it can be seen in Figure 4-11(b), time intervals and tolerances are determined for homogenization results.

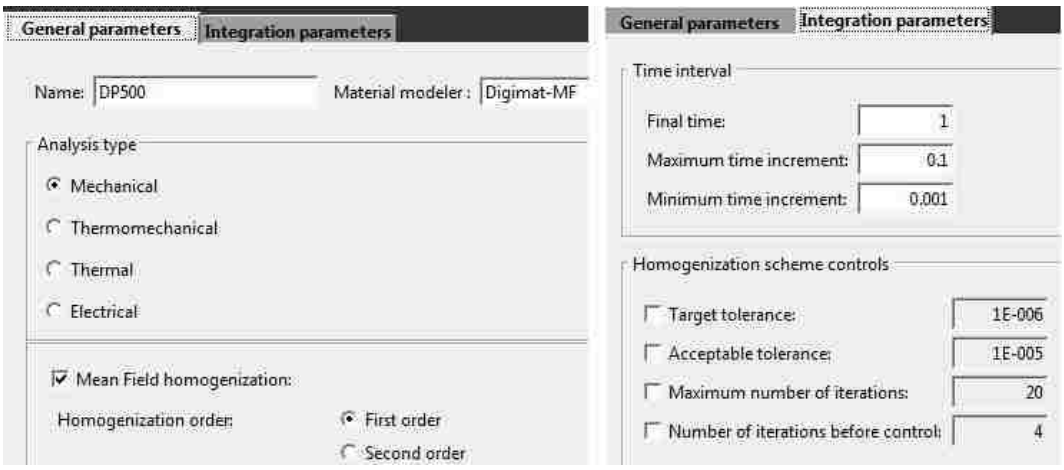

Figure 4-11 (a) General parameters and (b) integration parameters in the Digimat-MF

5 Modeling Results and Discussion

This chapter describes the results obtained from micromechanical modeling of flow curves of DP500 and DP600 steels deformed in uniaxial tension. Effects of RVE size, mesh size and element type were investigated to optimize the modeling parameters. The outcome of the model is the true flow stress as a function of true plastic strain. The goals of micromechanical modeling are to accurately predict the flow curves of the dual phase steels and to optimize modeling time (cost). In order to evaluate the accuracy of the modeling results, the predicted numerical flow curves were compared to the experimental flow curves presented in Figure 3-14 and Figure 3-15 for DP500 and DP600 steels, respectively. The modeling achievements are presented and discussed in the following.

5.1 Influence of RVE Size on Numerical Flow Curves

According to the previous reports by Uthaisangsuk et al [35], Thomser et al [36] and Ramazani et al [40], 2D RVE-based micromechanical modeling of flow behaviour of dual phase steel results in an underestimation of the flow stress. Reports indicated that, although both morphology and volume fraction of martensite were taken into account in 2D modeling only the volume fraction of martensite was considered in 3D modeling, and yet 3D modeling resulted in more accurate flow curves. Hence, this research focused on 3D modeling. As it is shown in Figure 5-1(a-c), in the previous work [35,39,40] on 3D micromechanical modeling of dual phase steels, the martensite phase was distributed randomly in the RVE cube regardless if its morphology. In this research, as it is presented in Figure 5-1(d), both the morphology and the volume fraction of martensite were considered to generate a 3D RVE which is more representative of the actual microstructure. Therefore, it is expected that the flow behaviour of the dual phase steels will be predicted more accurately in this investigation compared to the work previously reported [35,39,40].

According to the quantitative metallography results presented in Section 3.1, martensite islands were considered as ellipsoids, and the aspect ratio and size distribution of martensite islands were determined. This information was given to the Digimat software

to generate the 3D RVEs. As can be seen in Figure 5-2, after generation of an RVE, Digimat provides the size distribution of martensite in the generated RVE (Actual) and compares it with the size distribution of martensite in the actual microstructure (Reference). It is expected that more accurate modeling results will be achieved when the two size distributions are similar to each other. In order to obtain similar size distributions, the RVE size should be carefully determined.

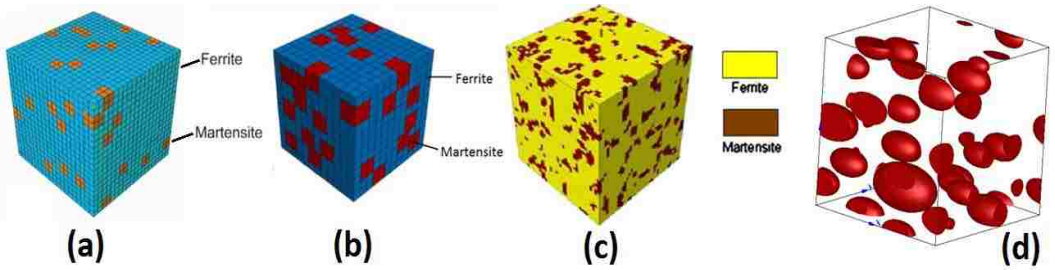

Figure 5-1 RVEs based on real microstructures generated by (a) Uthaisangsuk et al [35], (b) Paul [39], (c) Ramazani et al [40] and (d) Digimat for this research.

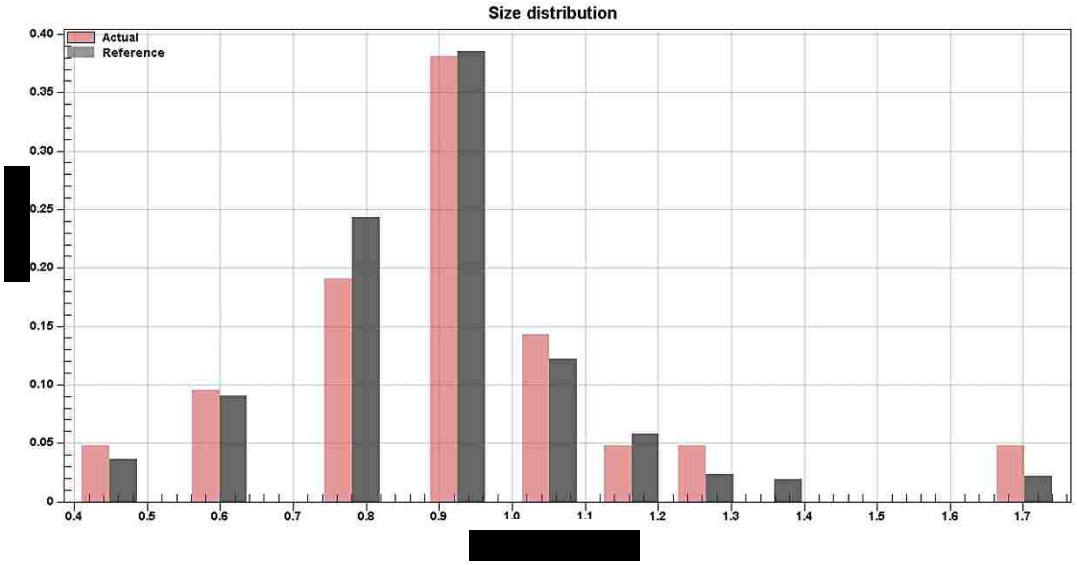

Figure 5-2 Size distribution of martensite in the RVE (Actual) and real microstructure (Reference)

Modeling results for DP500 and DP600 are presented in Sections 5.1.1 and 5.1.2, respectively. The following items are presented for each simulation:

(a) The random RVE which was generated by the Digimat-FE according to the volume fraction and morphology of martensite in the real microstructure
(b) Martensite size distribution in the generated RVE (Actual) and the actual microstructure (Reference)
(c) Distribution of von Mises stress in the RVE after simulation was accomplished in ABAQUS
(d) Distribution of equivalent strain in the RVE after simulation was accomplished in ABAQUS
(e) Flow curve of the RVE after post-processing was carried out with Digimat-FE
(f) Experimental and numerical flow curves of the steel after homogenization was completed in Digimat-MF

Distribution of von Mises stress and effective strain in the RVE is presented in Sections 5.1.1 and 5.1.2 for initial observation of stress and strain distribution in the RVE. A detailed discussion on this subject is presented in Section 5.5.

5.1.1 DP500 Dual Phase Steel

According to the quantitative metallography results, the martensite volume fraction in DP500 steel was 0.090. Based on the martensite content, the aspect ratio of martensite islands and the martensite size distribution in DP500 steel presented in Section 3.1, 6 RVEs with different sizes were generated. Table 5-1 shows the specifications of these RVEs.

Since both the morphology and the volume fraction of martensite were considered in RVE generation, all of the 6 RVEs properly presented the overall microstructural characteristics of the steel. Hence, as can be seen in Figure 5-3 to Figure 5-8, the predicted flow curves are generally very close to the experimental flow curve.

Table 5-1 Specifications of the RVEs generated for micromechanical modeling of DP500 steel

RVE Size Cube Side (μm)	Number of Martensite islands inside the RVE	Effective volume Fraction of Martensite inside the RVE	Modeling Results
9.5	11	0.090	Figure 5-3
10.3	14	0.089	Figure 5-4
11.6	20	0.091	Figure 5-5
12.7	26	0.090	Figure 5-6
13.2	29	0.090	Figure 5-7
14.2	36	0.096	Figure 5-8

As it can be seen in Figure 5-6(f), Figure 5-7(f) and Figure 5-8(f), when the number of martensite islands inside an RVE is more than 25, the numerical flow curve practically lies on the experimental flow curve. While the ultimate tensile strength (UTS) in the experimental flow curve is 648.7 MPa, the RVEs with 26, 29 and 36 martensite islands predict an ultimate tensile strength of 649.0, 649.6 and 646.8 MPa, respectively. Hence, the error is less than 0.3%.

When the number of martensite islands in the RVEs was 11, 14 and 20, the numerical flow curve underestimated the flow stress of DP500 steel. The predicted ultimate tensile strengths by the RVEs including 11, 14 and 20 martensite islands were 637.4, 647.6 and 632.1 MPa, respectively.

Compared to the RVEs with more than 25 martensite islands, since the number of martensite islands inside of RVEs with 11, 14 and 20 martensite islands was not sufficient, the size distribution of martensite in the RVE was not sufficiently similar to the size distribution of martensite in the real microstructure. Hence, these smaller RVEs could not properly represent the characteristics of the microstructure.

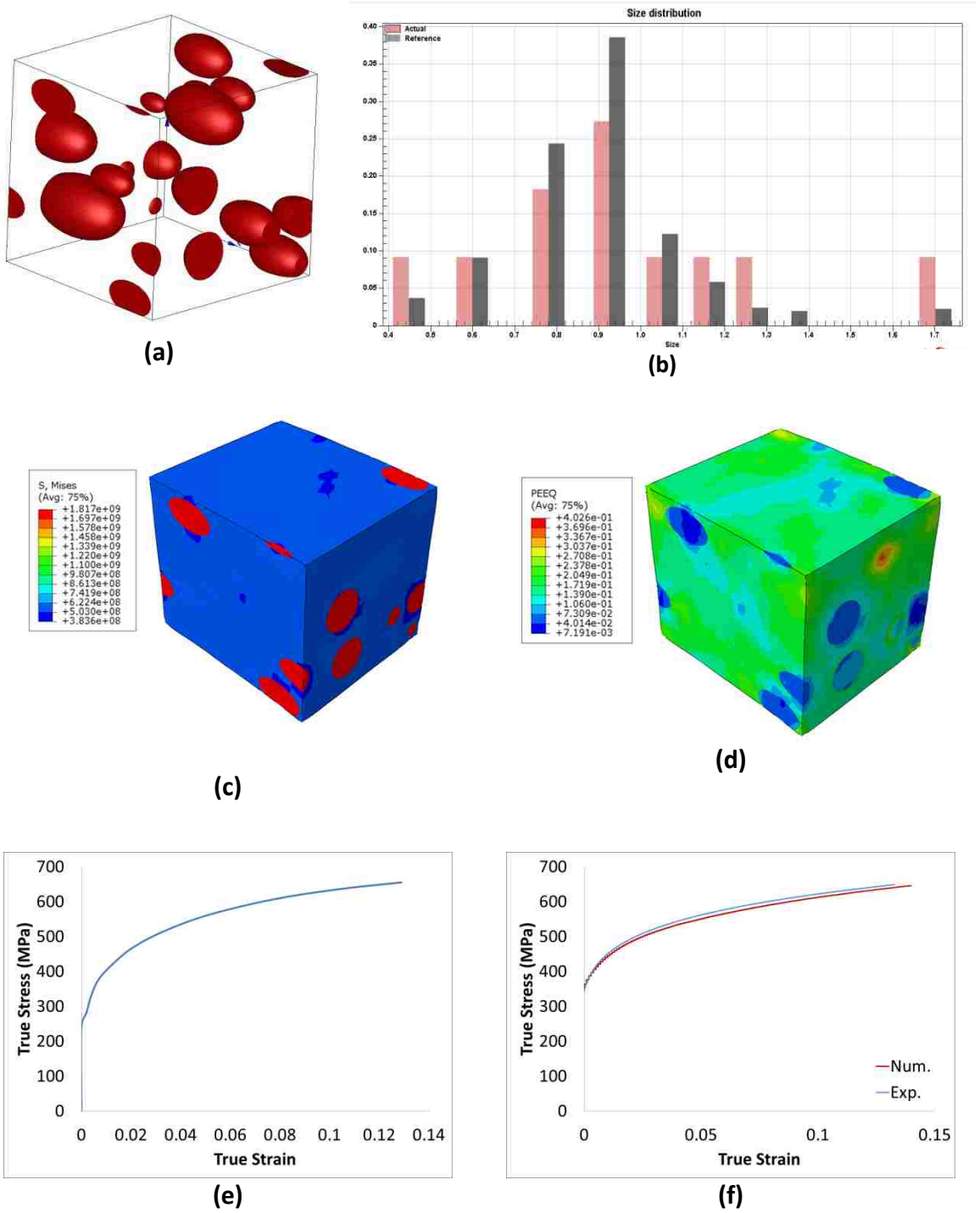

Figure 5-3 Micromechanical modeling results for DP500 steel with 11 martensite islands inside the RVE: (a) RVE, (b) distribution of martensite in the RVE, (c) distribution of von Mises stress in the RVE at ε≈0.12, (d) distribution of equivalent strain in the RVE at ε≈0.14, (e) flow curve of RVE and (f) numerical and experimental flow curves of DP500 steel.

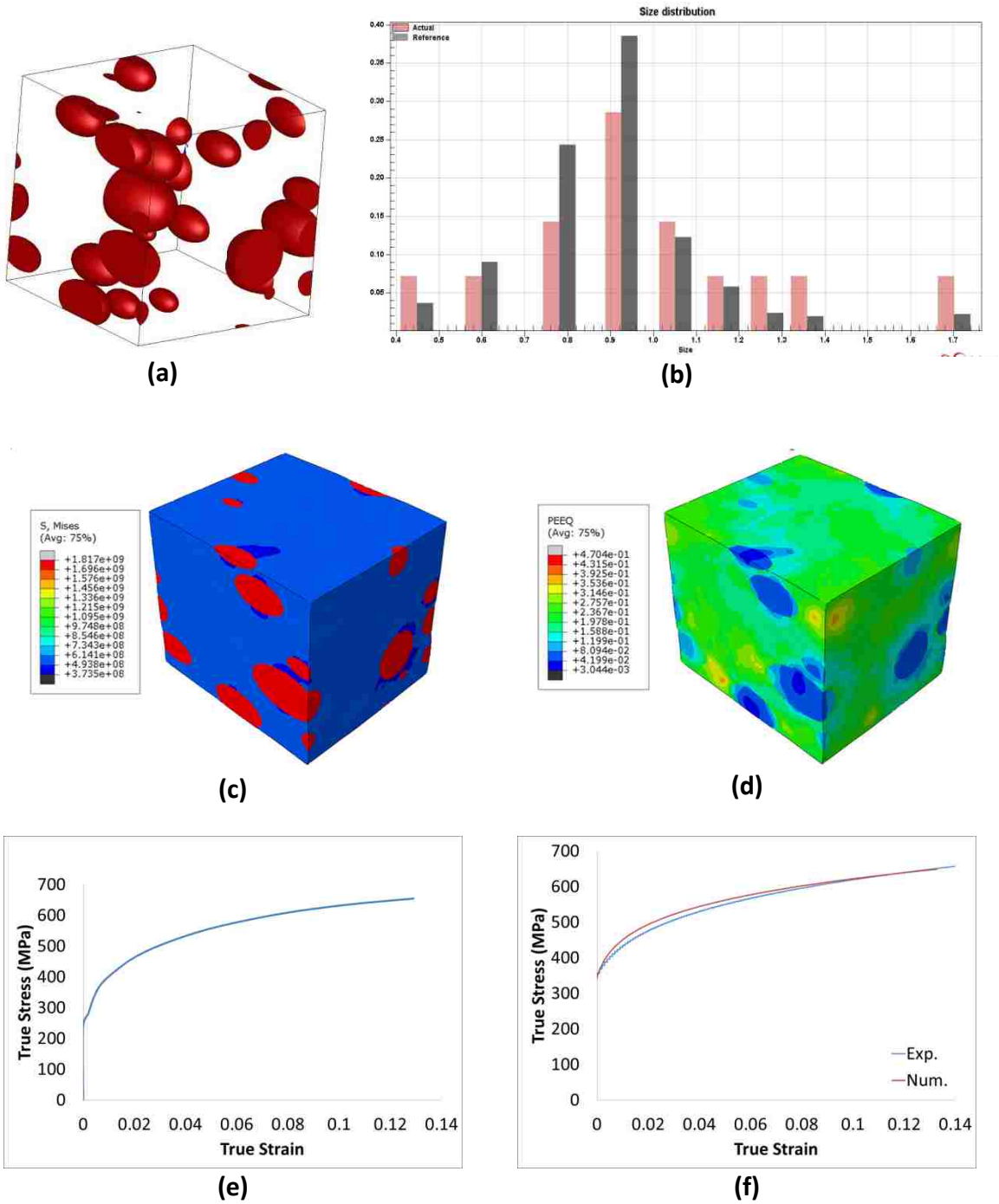

Figure 5-4 Micromechanical modeling results for DP500 steel with 14 martensite islands inside the RVE: (a) RVE, (b) distribution of martensite in the RVE, (c) distribution of von Mises stress in the RVE at ε≈0.12, (d) distribution of equivalent strain in the RVE at ε≈0.14, (e) flow curve of RVE and (f) numerical and experimental flow curves of DP500 steel.

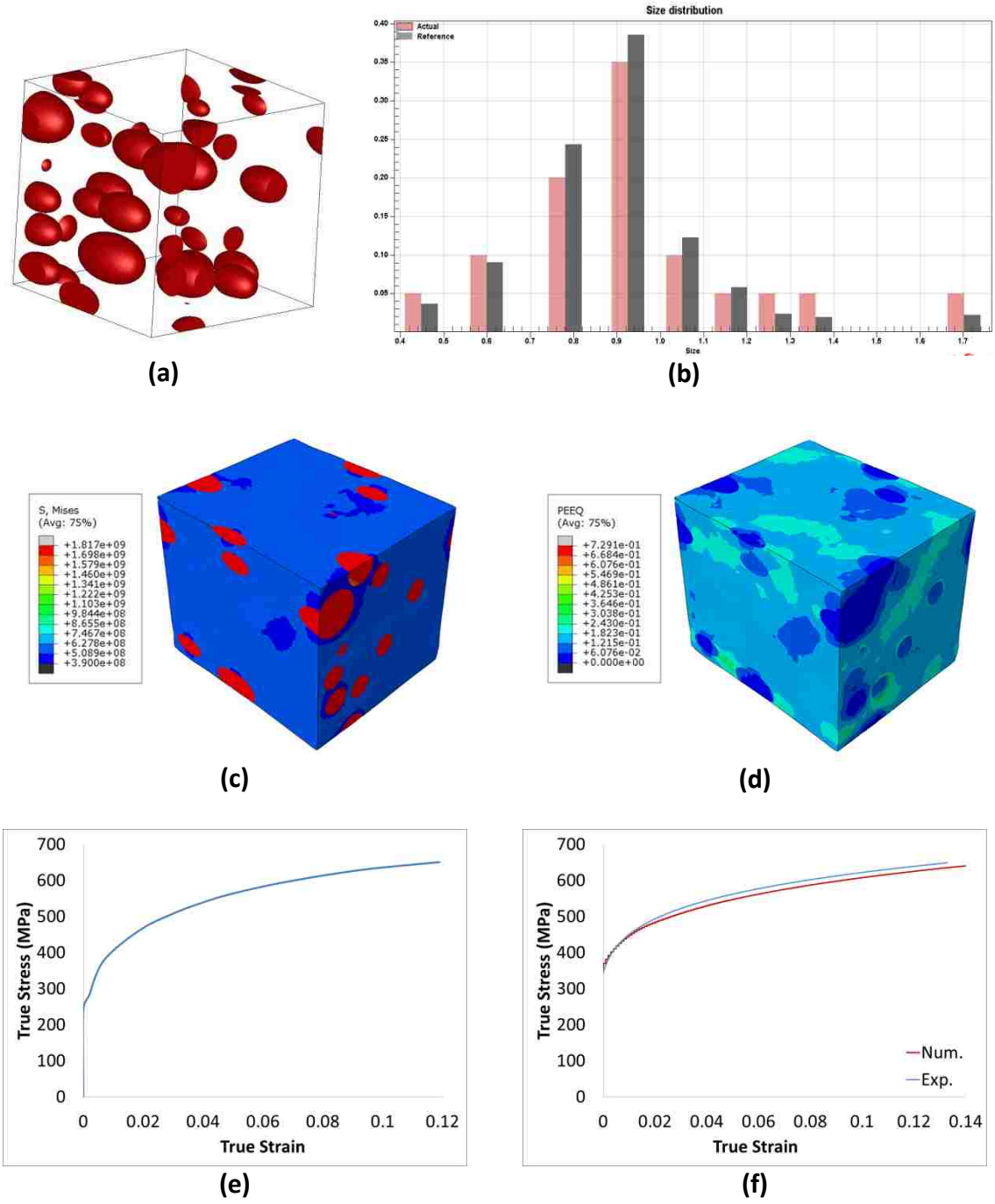

Figure 5-5 Micromechanical modeling results for DP500 steel with 20 martensite islands inside the RVE: (a) RVE, (b) distribution of martensite in the RVE, (c) distribution of von Mises stress in the RVE at ε≈0.12, (d) distribution of equivalent strain in the RVE at ε≈0.14, (e) flow curve of RVE and (f) numerical and experimental flow curves of DP500 steel.

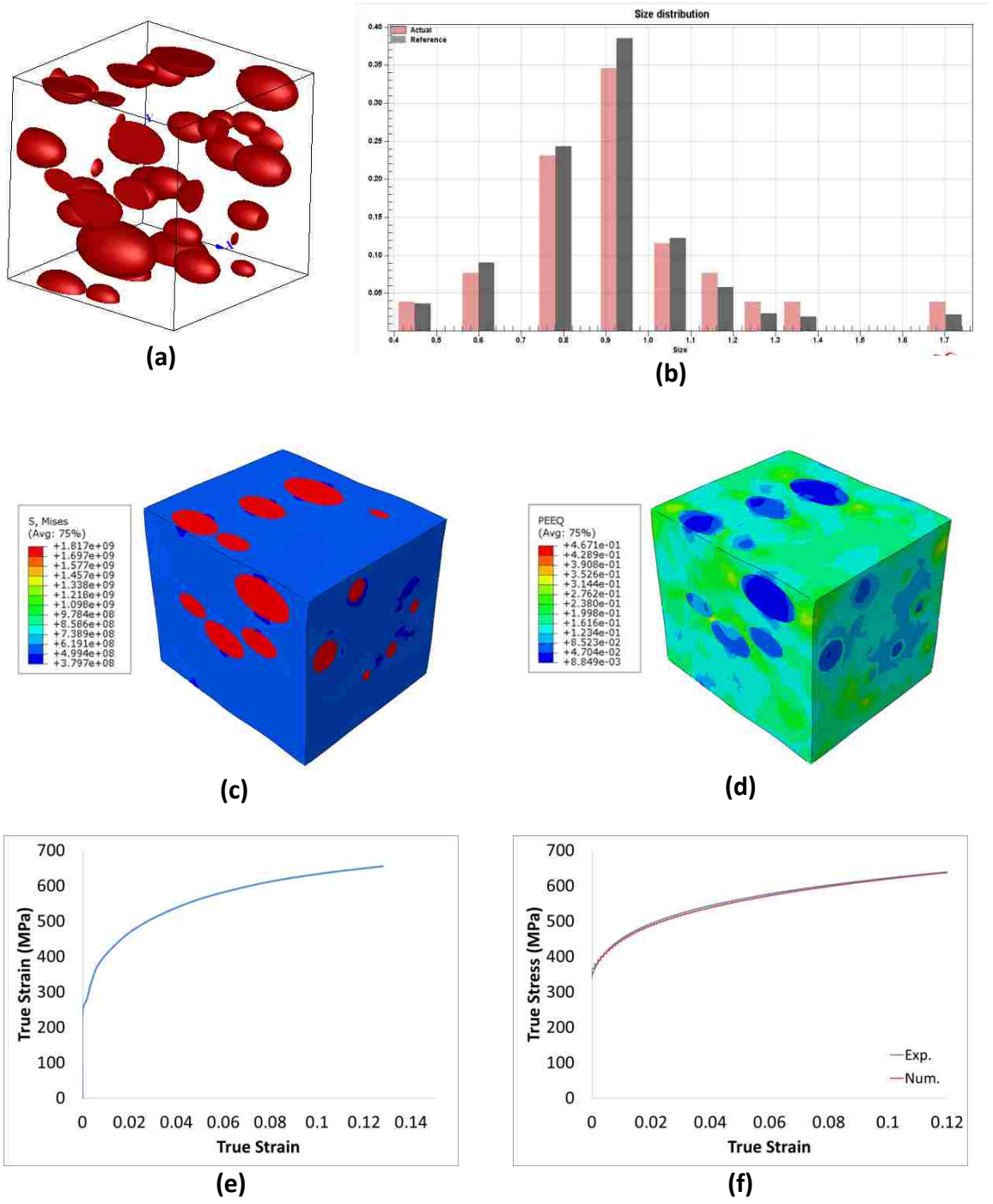

Figure 5-6 Micromechanical modeling results for DP500 steel with 26 martensite islands inside the RVE: (a) RVE, (b) distribution of martensite in the RVE, (c) distribution of von Mises stress in the RVE at ε≈0.12, (d) distribution of equivalent strain in the RVE at ε≈0.14, (e) flow curve of RVE and (f) numerical and experimental flow curves of DP500 steel.

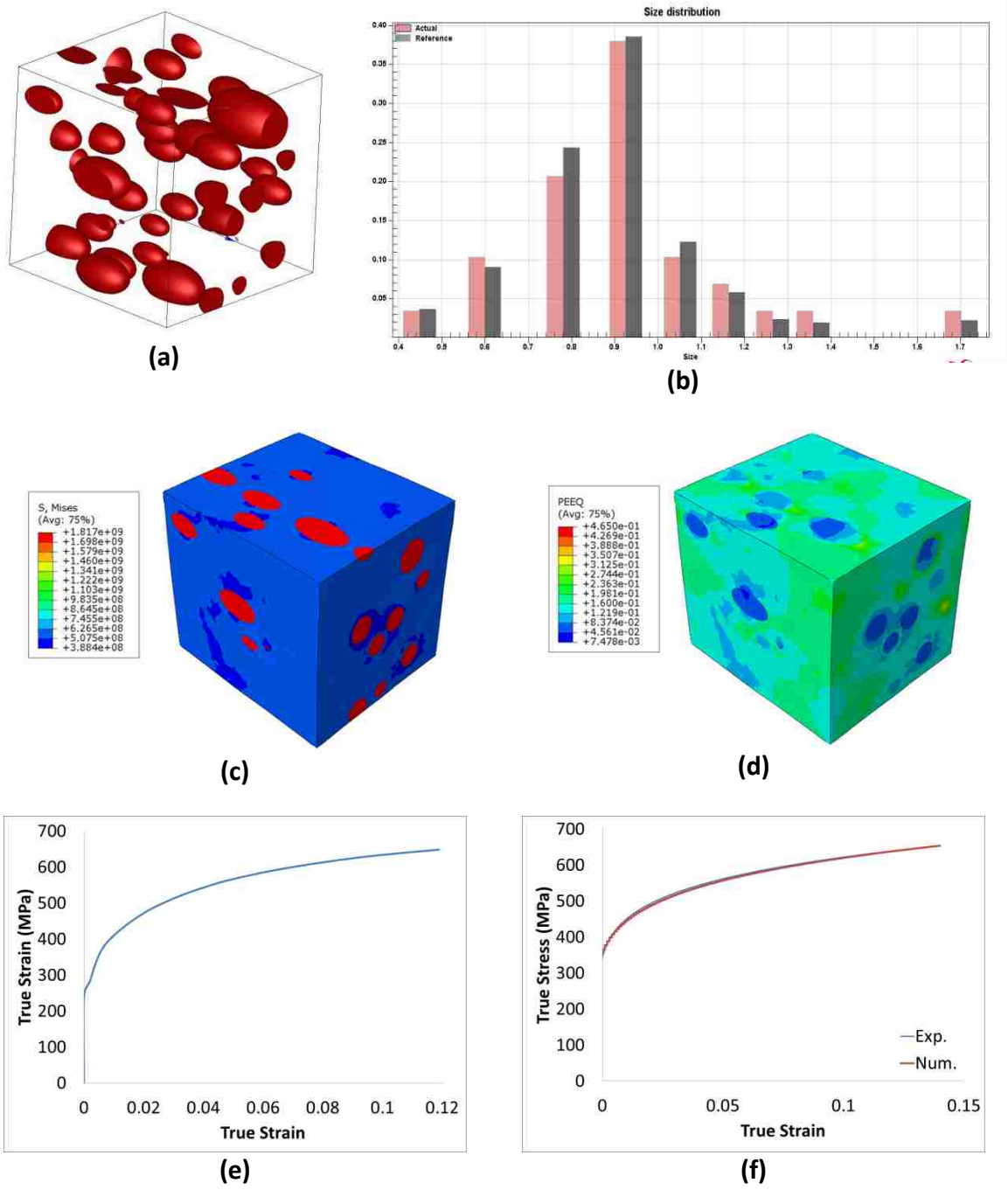

Figure 5-7 Micromechanical modeling results for DP500 steel with 29 martensite islands inside the RVE: (a) RVE, (b) distribution of martensite in the RVE, (c) distribution of von Mises stress in the RVE at ε≈0.12, (d) distribution of equivalent strain in the RVE at ε≈0.14, (e) flow curve of RVE and (f) numerical and experimental flow curves of DP500 steel.

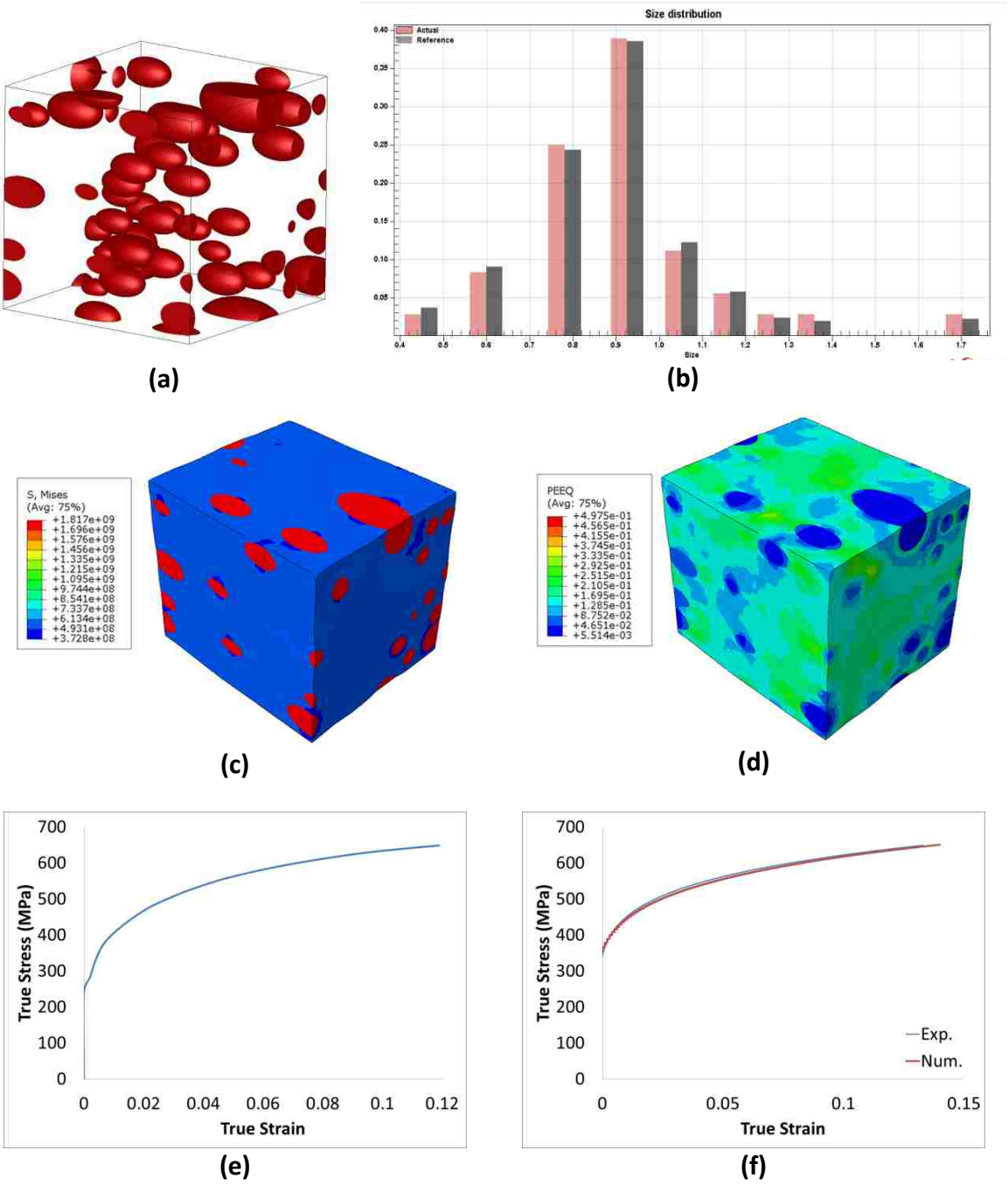

Figure 5-8 Micromechanical modeling results for DP500 steel with 36 martensite islands inside the RVE: (a) RVE, (b) distribution of martensite in the RVE, (c) distribution of von Mises stress in the RVE at ε≈0.12, (d) distribution of equivalent strain in the RVE at ε≈0.14, (e) flow curve of RVE and (f) numerical and experimental flow curves of DP500 steel.

In order to determine the accuracy of the predicted flow curves, the experimental and predicted tensile toughness of the DP500 steel, i.e. the area below the flow curves, were compared. The predicted toughness of the steel was numerically calculated using more than 2000 data points. As it is shown in Figure 5-9(a), all the RVEs predicted the toughness of the steel quite accurately. For a more precise comparison, the results of Figure 5-9(a) are shown in Figure 5-9(b) with a magnified scale. As it can be seen, the RVEs with a size of 9.5, 10.3 and 11.6 μm^3, underestimated the toughness of the steel more than the RVEs with a size of equal to or greater than 12.7 µm.

Comparing the modeling results for the DP500 flow curve, the accuracy of modeling results using RVEs with a size of 12.7, 13.2 and 14.2 μm^3 and with 26, 29 and 36 martensite islands, respectively, was almost similar; however, modeling time for the RVEs with 29 and 36 martensite islands is notably longer than the required modeling time for the RVE with 26 martensite islands. Therefore, an RVE size of 12.7x12.7x12.7 μm^3 containing 26 martensite islands is suggested as the optimum RVE size since it accurately predicted the flow curve of this DP500 steel. As can be seen in Figure 5-6(b), when the number of martensite islands was 26, it was feasible for the Digimat software to generate an RVE with a martensite size distribution similar to the martensite size distribution in the real microstructure.

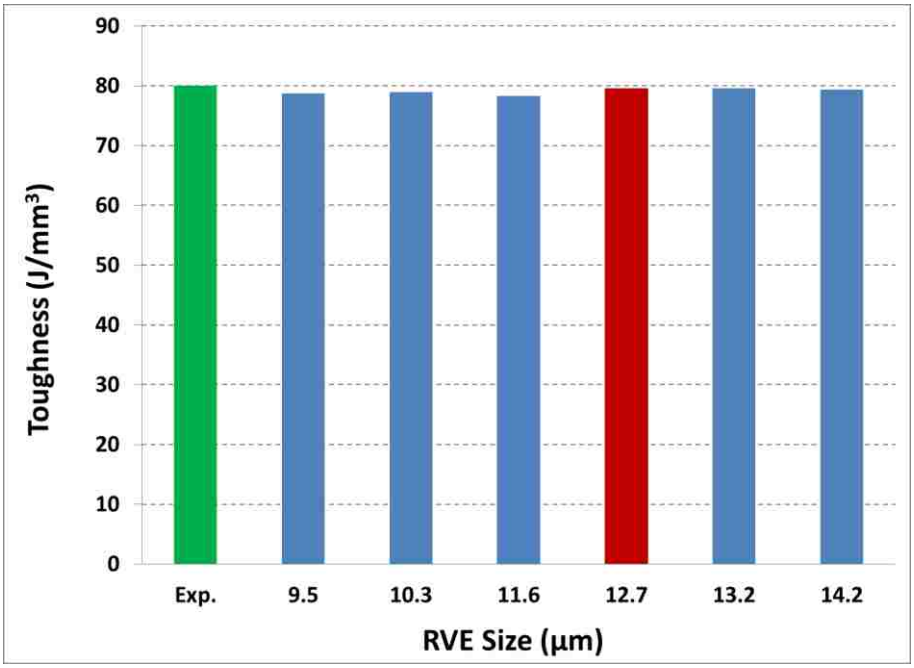

(a)

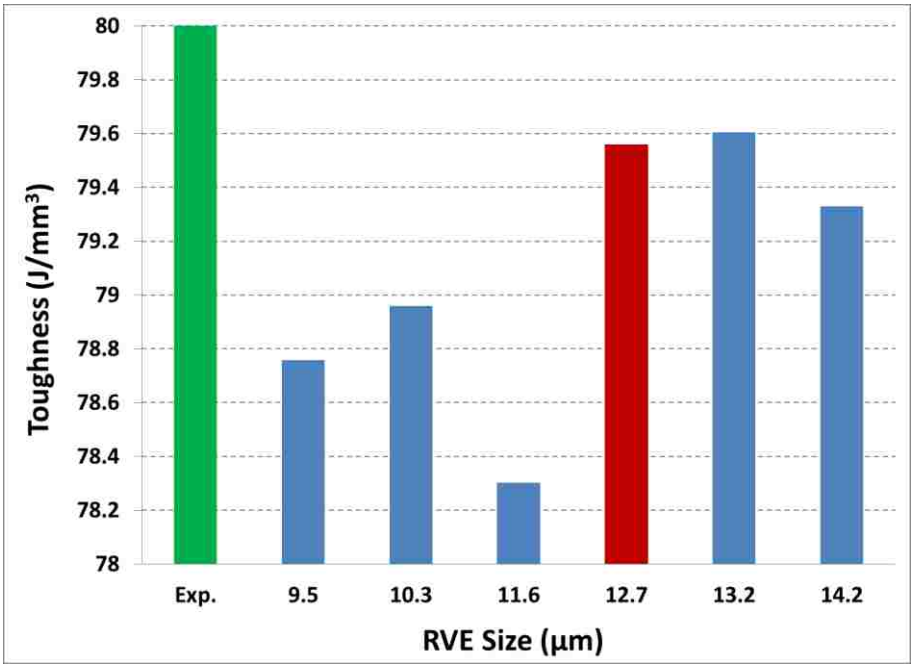

(b)

Figure 5-9 (a) Tensile toughness of the DP500 steel as measured under the experimental flow curve and predicted using RVEs of different sizes, and (b) with an enlarged scale.

5.1.2 DP600 Dual Phase Steel

According to the quantitative metallography results, the martensite volume fraction in DP600 steel was 0.047. Based on the martensite content, the martensite aspect ratio and the martensite size distribution in DP600 steel presented in Section 3.1, 6 RVEs with different sizes were generated. Table 5-2 shows the specifications of these RVEs. Modeling results for each RVE is presented in a figure as indicated in Table 5-2.

Table 5-2 Specifications of the RVEs generated for micromechanical modeling of DP600 steel

RVE Size Cube Side (μm)	Number of Martensite islands inside the RVE	Effective volume Fraction of Martensite inside the RVE	Modeling Results
6.0	11	0.047	Figure 5-10
6.5	14	0.047	Figure 5-11
7.3	20	0.048	Figure 5-12
7.9	26	0.047	Figure 5-13
8.2	32	0.047	Figure 5-14
8.8	36	0.046	Figure 5-15

As it was seen in Section 5.1.1, the experimental and numerical flow curves of DP500 steel were in good agreement and the ultimate tensile strength of steel was predicted with less than 0.3% of error. Many attempts were made to predict the flow curve of DP600 steel with a negligible deviation from the experimental flow curve similar to DP500 steel; however, as can be seen in Figure 5-10 to Figure 5-15, the prediction of the DP600 steel flow curve from the onset of plastic deformation up to uniform elongation was not as accurate as it was for DP500 steel.

When the number of martensite islands in the RVE is 11 and 14, there is a notable difference between the predicted and experimental flow curves up to a plastic strain of 0.08. At greater strains, the numerical and experimental curves almost coincided.

By increasing the RVE size to 7.9x7.9x7.9 μm^3 with 26 martensite islands inside the RVE, the predicted flow curve precisely corresponded with the flow curve of DP600 steel at

strains greater than 0.07. However, increasing the RVE size to larger than 7.9x7.9x7.9 μm^3 with more martensite islands inside the RVE increased the modeling time but did not improve the accuracy of the results. And, the deviation between the numerical and experimental flow curves up to plastic strains of 0.07 did not decrease.

While the experimental ultimate tensile strength (UTS) was 686.2 MPa, the RVEs with 11, 14, 20, 26, 32 and 36 martensite islands predicted an ultimate tensile strength of 688.4, 691.3, 685.2, 686.0, 685.3 and 687.9 MPa, respectively. Therefore, an RVE with a size of 7.9x7.9x7.9 μm^3 with 26 martensite islands resulted in the most accurate prediction of the flow curve and the predicted tensile strength of DP600 steel had a 0.03% error.

In order to determine the accuracy of the predicted flow curves, the experimental and predicted tensile toughness of the DP600 steel were compared for true plastic strains greater than 0.07. The predicted toughness of the steel was numerically calculated using more than 2000 data points. As it is shown in Figure 5-16(a), the all RVEs predicted the toughness of the steel quite accurately. For a more precise comparison, Figure 5-16(a) is enlarged in Figure 5-16(b), and it can be seen that the toughness predicted using RVEs with a size of 7.9, 8.2 and 8.8 μm^3 are similar to the experimental toughness. Since the required modeling time and resources for the RVE with a size of 7.9 μm^3 is shorter, it is suggested as the optimum RVE size.

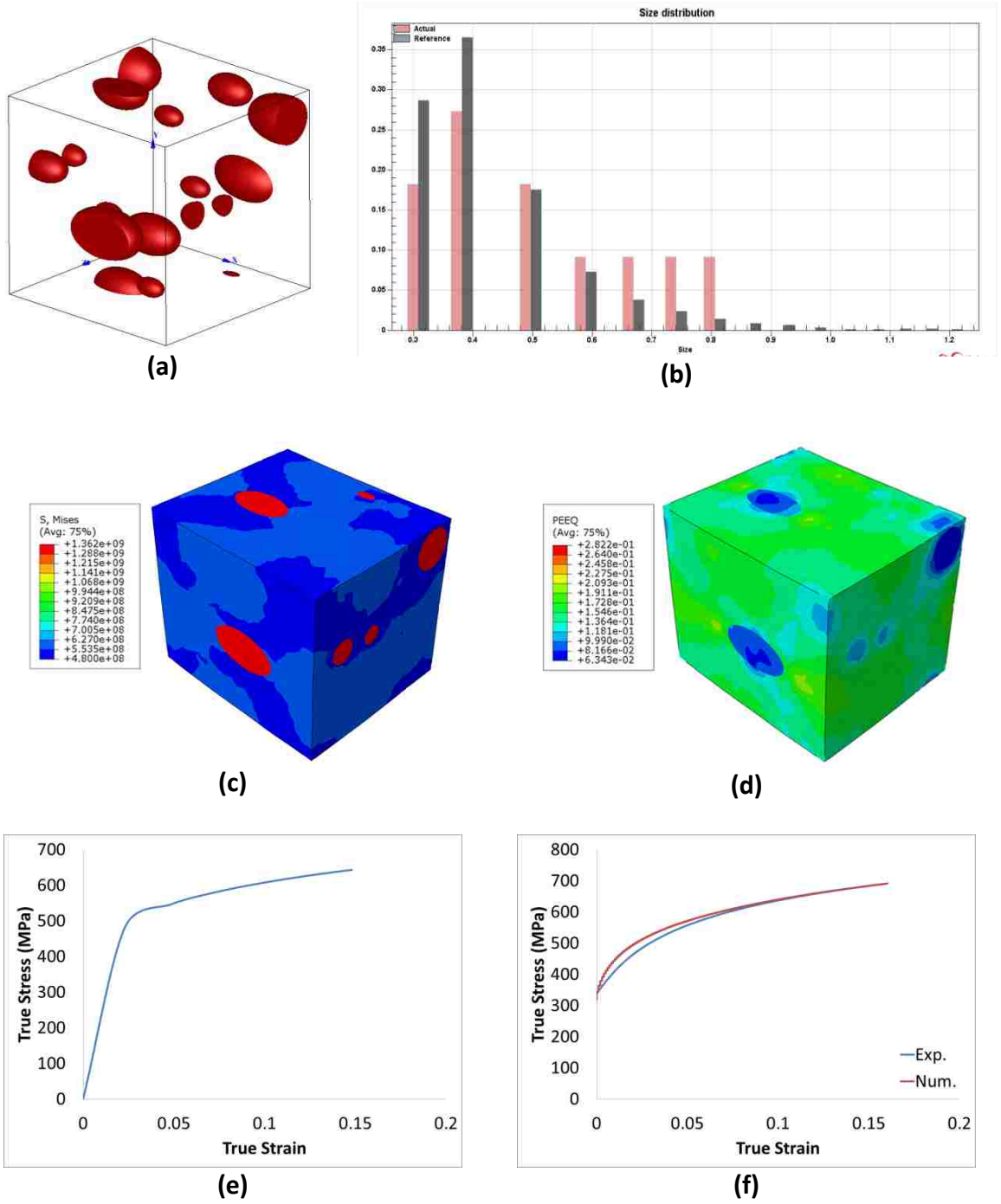

Figure 5-10 Micromechanical modeling results for DP600 steel with 11 martensite islands inside the RVE: (a) RVE, (b) distribution of martensite in the RVE, (c) distribution of von Mises stress in the RVE at ε≈0.125, (d) distribution of equivalent strain in the RVE at ε≈0.15, (e) flow curve of RVE and (f) numerical and experimental flow curves of DP600 steel.

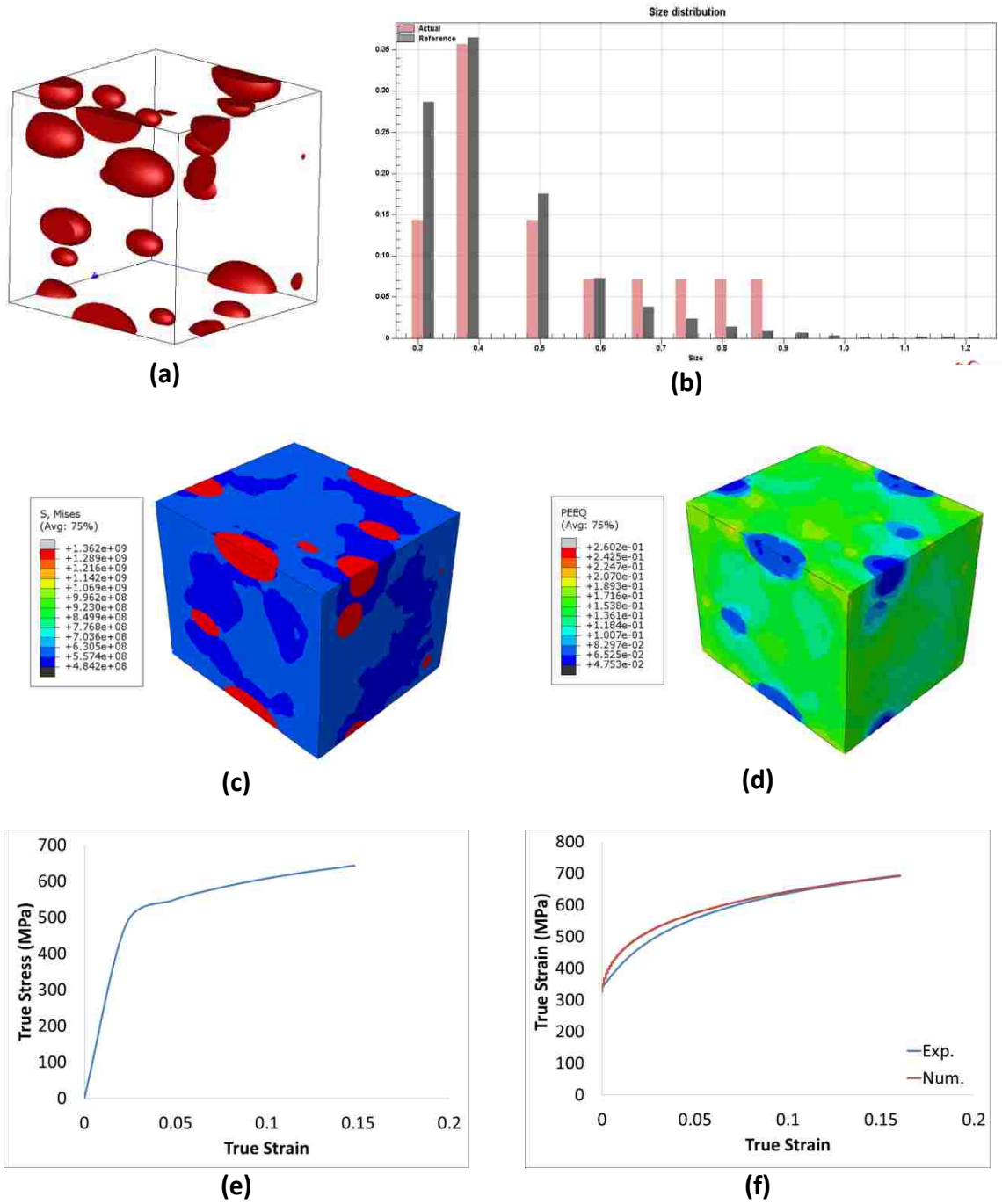

Figure 5-11 Micromechanical modeling results for DP600 steel with 14 martensite islands inside the RVE: (a) RVE, (b) distribution of martensite in the RVE, (c) distribution of von Mises stress in the RVE at ε≈0.125, (d) distribution of equivalent strain in the RVE at ε≈0.15, (e) flow curve of RVE and (f) numerical and experimental flow curves of DP600 steel.

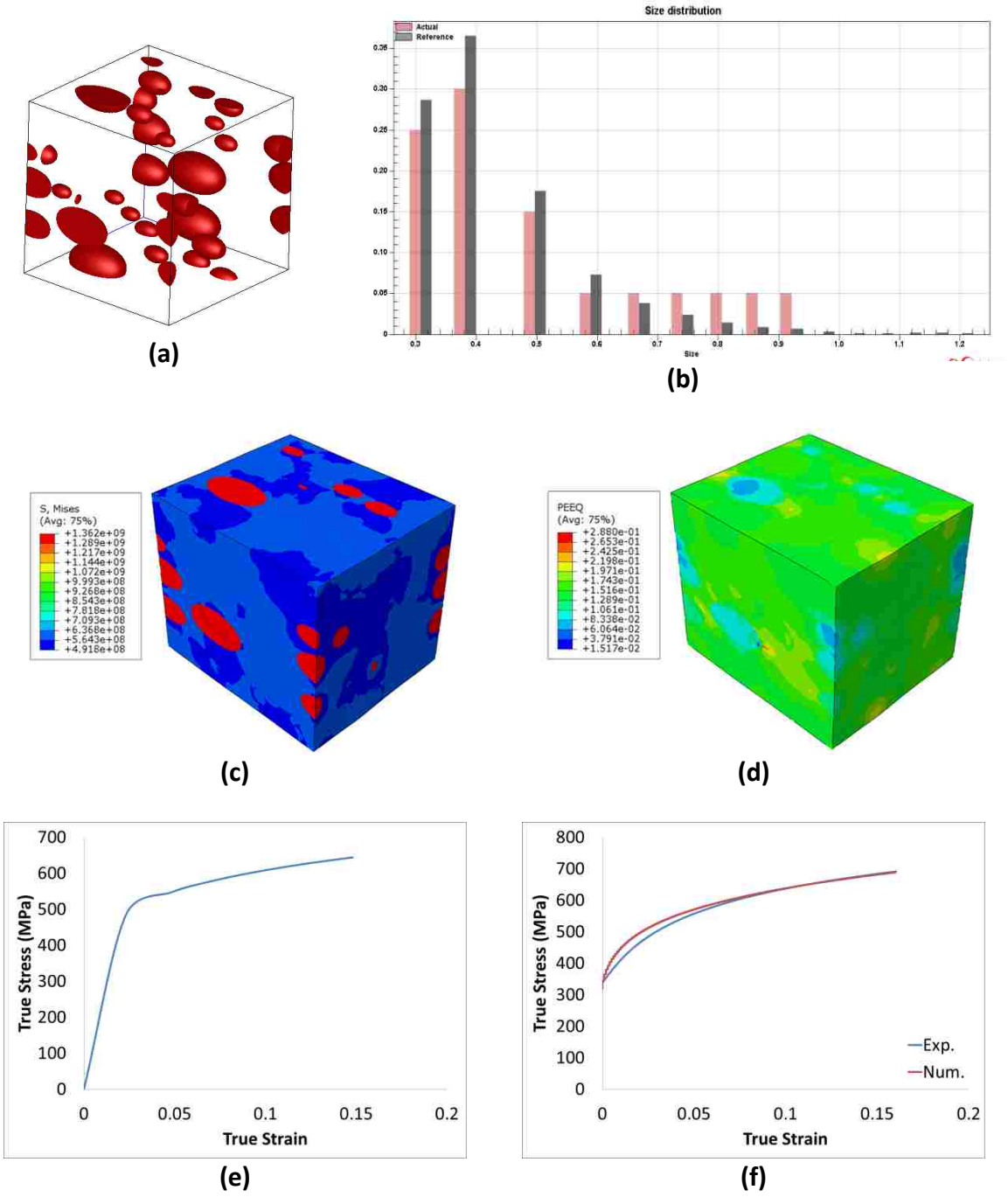

Figure 5-12 Micromechanical modeling results for DP600 steel with 20 martensite islands inside the RVE: (a) RVE, (b) distribution of martensite in the RVE, (c) distribution of von Mises stress in the RVE at ε≈0.125, (d) distribution of equivalent strain in the RVE at ε≈0.15, (e) flow curve of RVE and (f) numerical and experimental flow curves of DP600 steel.

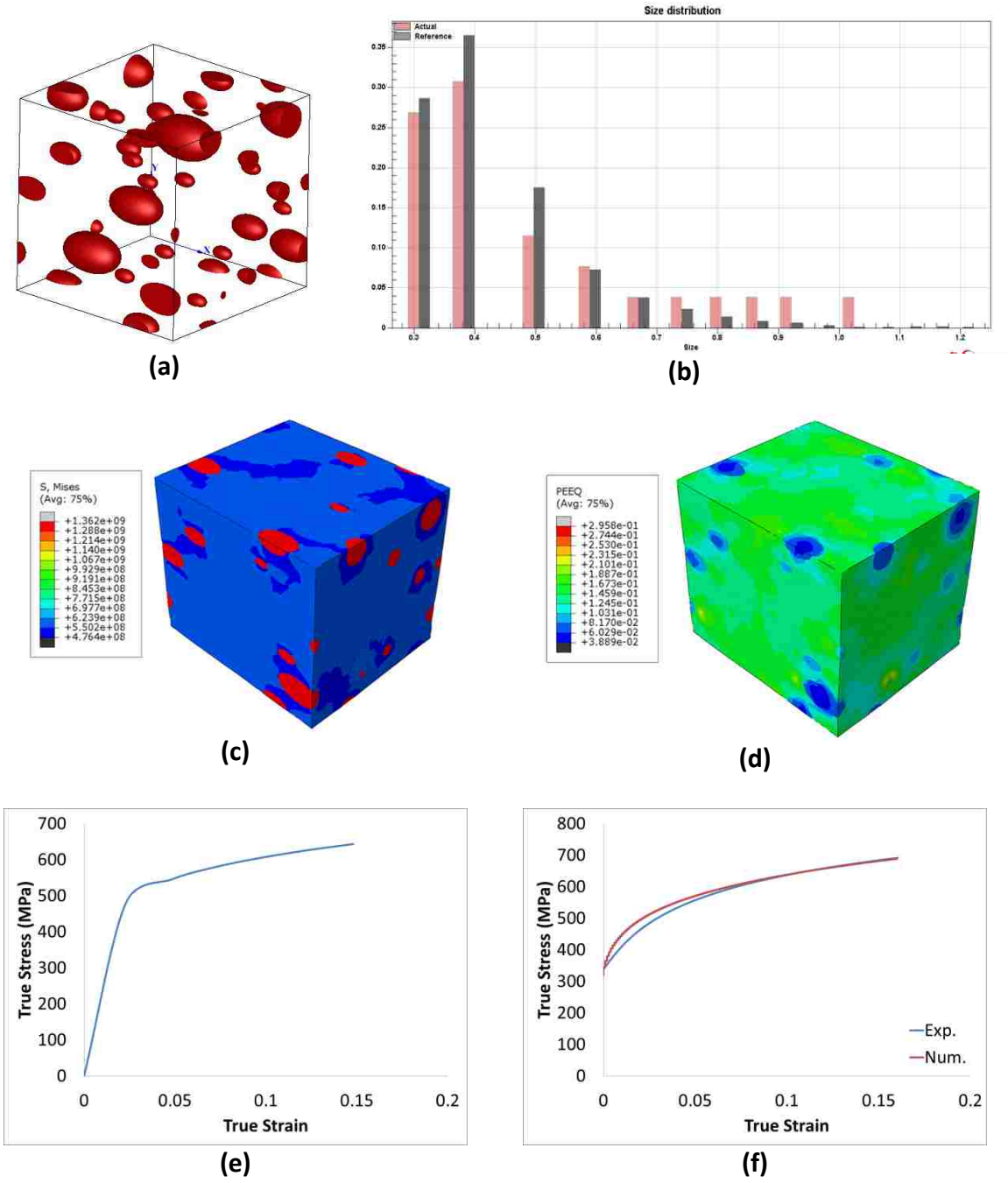

Figure 5-13 Micromechanical modeling results for DP600 steel with 26 martensite islands inside the RVE: (a) RVE, (b) distribution of martensite in the RVE, (c) distribution of von Mises stress in the RVE at ε≈0.125, (d) distribution of equivalent strain in the RVE at ε≈0.15, (e) flow curve of RVE and (f) numerical and experimental flow curves of DP600 steel.

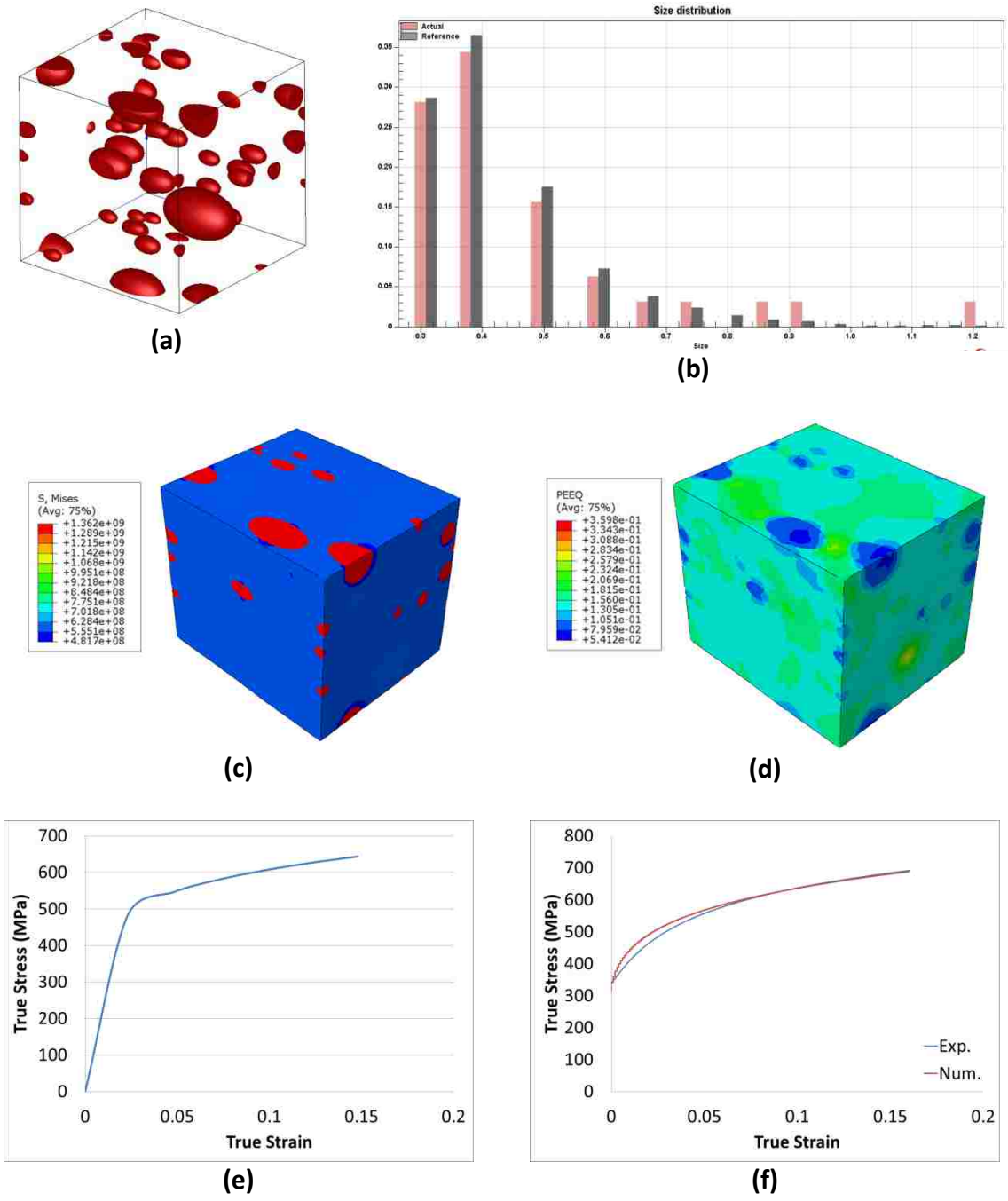

Figure 5-14 Micromechanical modeling results for DP600 steel with 32 martensite islands inside the RVE: (a) RVE, (b) distribution of martensite in the RVE, (c) distribution of von Mises stress in the RVE at ε≈0.125, (d) distribution of equivalent strain in the RVE at ε≈0.15, (e) flow curve of RVE and (f) numerical and experimental flow curves of DP600 steel.

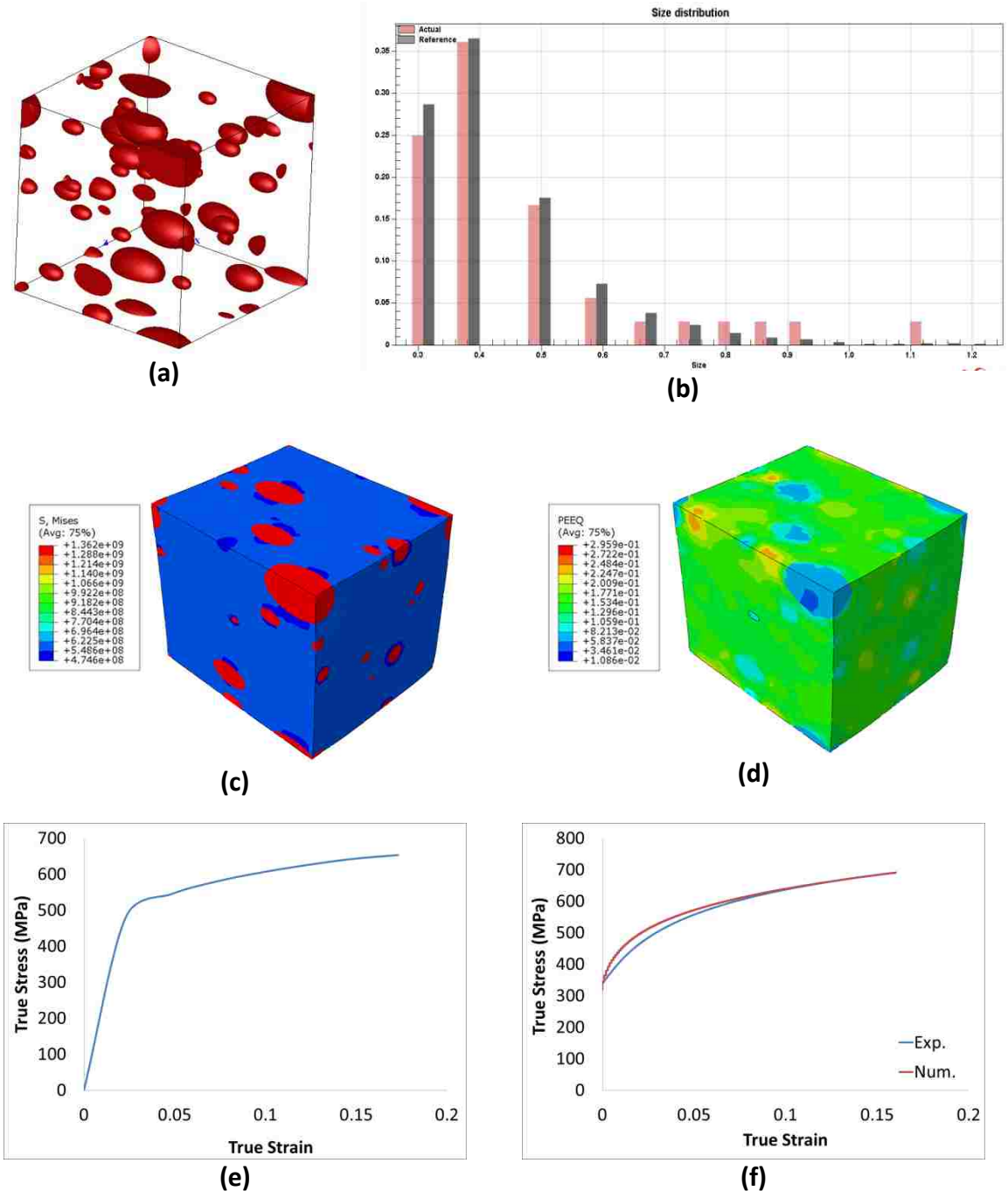

Figure 5-15 Micromechanical modeling results for DP600 steel with 36 martensite islands inside the RVE: (a) RVE, (b) distribution of martensite in the RVE, (c) distribution of von Mises stress in the RVE at ε≈0.125, (d) distribution of equivalent strain in the RVE at ε≈0.15, (e) flow curve of RVE and (f) numerical and experimental flow curves of DP600 steel.

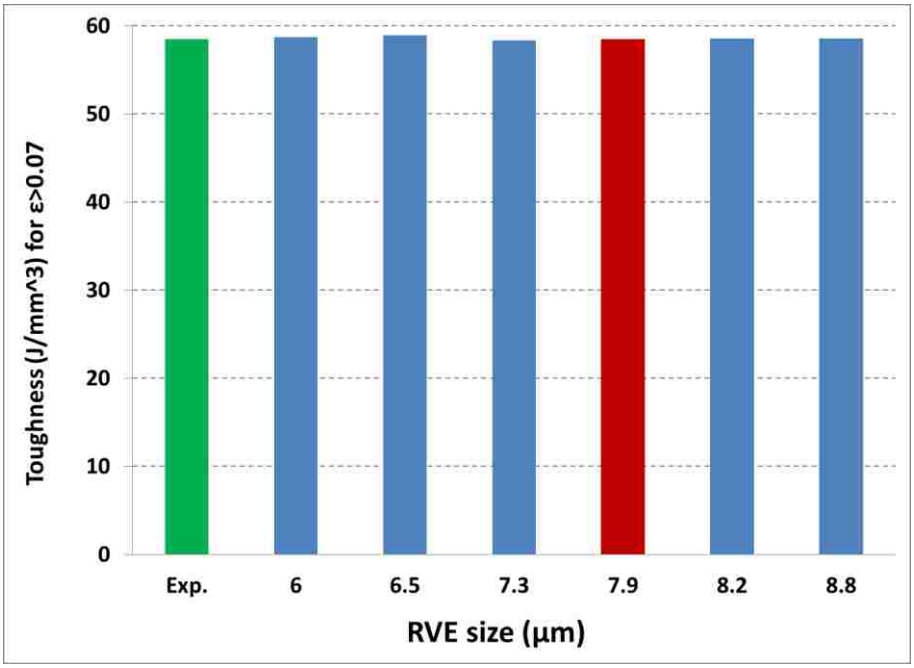

(a)

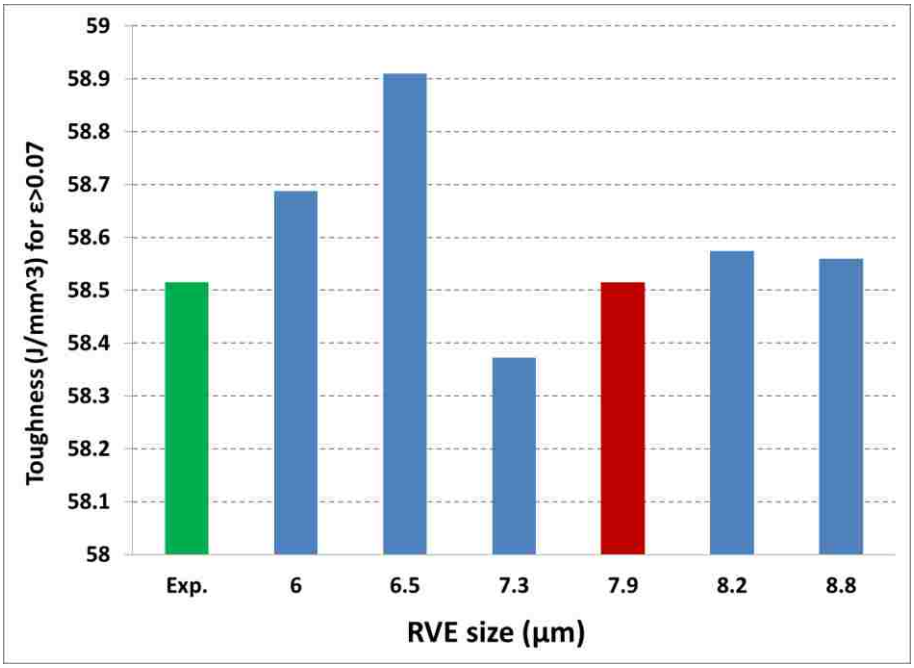

(b)

Figure 5-16 (a) Tensile toughness of the DP600 steel as measured under the experimental flow curve and predicted using RVEs of different sizes, and (b) with an enlarged scale.

The optimum RVE size for DP500 and DP600 was 12.7x12.7x12.7 μm^3 and 7.9x7.9x7.9 μm^3, respectively, with each RVE containing 26 martensite islands. It can be concluded that, the optimum RVE should be sufficiently large to accommodate at least 25 martensite islands. And thus, the size distribution of martensite in the RVEs will be sufficiently close to the size distribution of martensite in the real microstructure. Since the average martensite size in DP500 and DP600 was 0.90 and 0.56 µm, respectively, the RVE in DP500 steel with 26 martensite islands was larger than the RVE with 26 martensite islands in DP600 steel.

Considering the experimental flow curves of DP600 steel presented in Figure 3-15, the yield point phenomenon had an influence on the flow behaviour of DP600 steel. During yield point elongation, many dislocations become mobile before the steel begins to work harden. This effect was not considered in Equation **2-10**. Therefore, the constitutive behaviour of the phases in the microstructure of DP600 steel was not predicted properly. As a result, there is a deviation between the numerical and experimental flow curves of DP600 steel at lower strains. As can be seen in the numerical flow curves presented in Figure 5-10 to Figure 5-15, in all cases, the initial deviation between the numerical and experimental flow curves gradually decreases as deformation increases. Once a strain of 0.07 has been reached in the optimum RVE, the work hardening has been sufficiently increased in the microstructure of DP600 steel and the effect of yield elongation has become negligible. Therefore, Equation **2-10** is able to precisely describe flow behaviour of the constituents in the microstructure of DP600 steel. Eventually, the numerical and experimental flow curves become approximately identical.

5.2 Influence of Mesh Size on Numerical Flow Curves

To investigate the influence of mesh size on the numerical flow curves of DP500 and DP600 steel, the RVEs with optimum size were meshed with elements having a size of 0.025, 0.050 and 0.075 μm at the surfaces of the RVE cubes.

The influence of mesh size on the predicted flow curves is presented in Figure 5-17 and Figure 5-18 for DP500 and DP600 steels, respectively. As can be seen, the mesh size caused no notable difference in the flow curves. Only in the case of DP500 steel, as can be seen in Figure 5-17(b), the RVE with an element size of 0.075 μm slightly overestimated the flow curve. This result is in good agreement with the previous results reported by Uthaisangsuk et al [35]. They investigated the effects of different mesh sizes from 100×100 to 260×260 elements on the flow behaviour of RVE of DP600 steel with 27 vol% of martensite and found small discrepancies in flow behaviour of the RVEs with different mesh sizes.

In view of the overestimation made by the 0.075 μm mesh in DP500 steel and also since ABAQUS performs mesh refinement during the simulation of the RVEs with 0.075 μm mesh, 0.050 μm is suggested as the optimum element size on the surfaces of the RVEs.

The computer which was used to carry out the simulations was a Dell T3600 with Intel® Xeon® processor E5-1600 with six cores and 32 GB of 1600 MHz DDR3 memory. The modeling time for RVEs with 0.025 μm mesh size was at least 12 times more than that for the RVEs with a 0.050 μm mesh size and the accuracy of the results did not improve.

Figure 5-19 to Figure 5-24 show the discretization of the RVEs in DP500 and DP600 steels at true strains of 0.14 and 0.16, respectively. Cross sections of the RVEs are also presented at different depths.

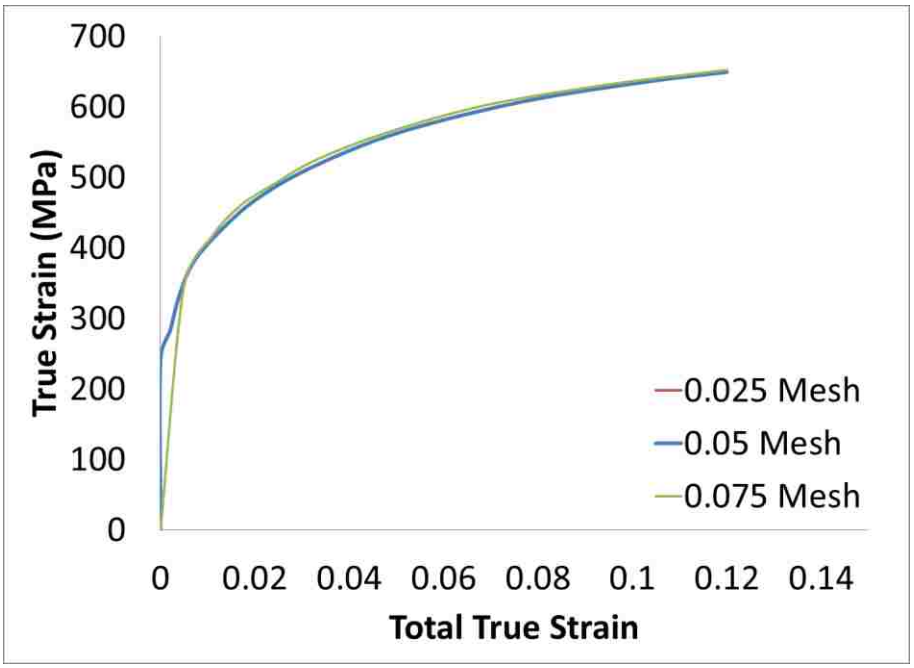

(a)

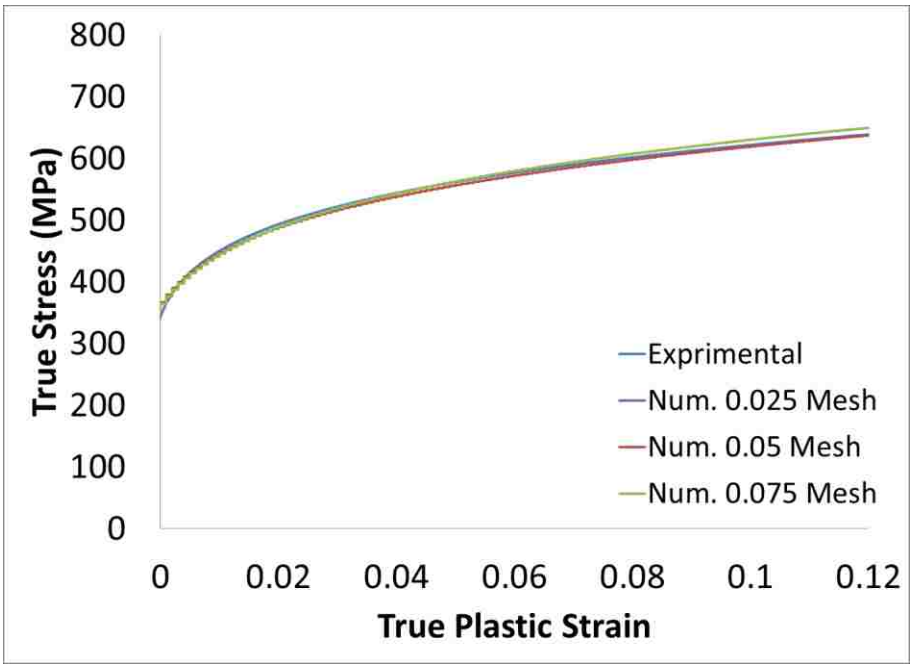

(b)

Figure 5-17 Effect of mesh size on modeling results for DP500 steel with 26 martensite islands inside the RVE: (a) flow curves of RVEs and (b) numerical and experimental flow curves of DP500 steel.

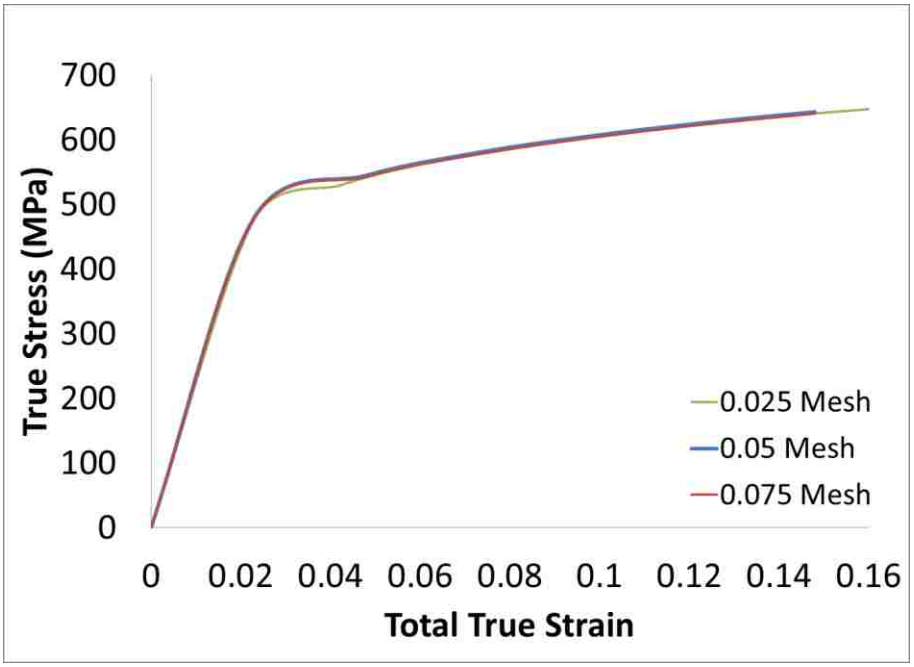

(a)

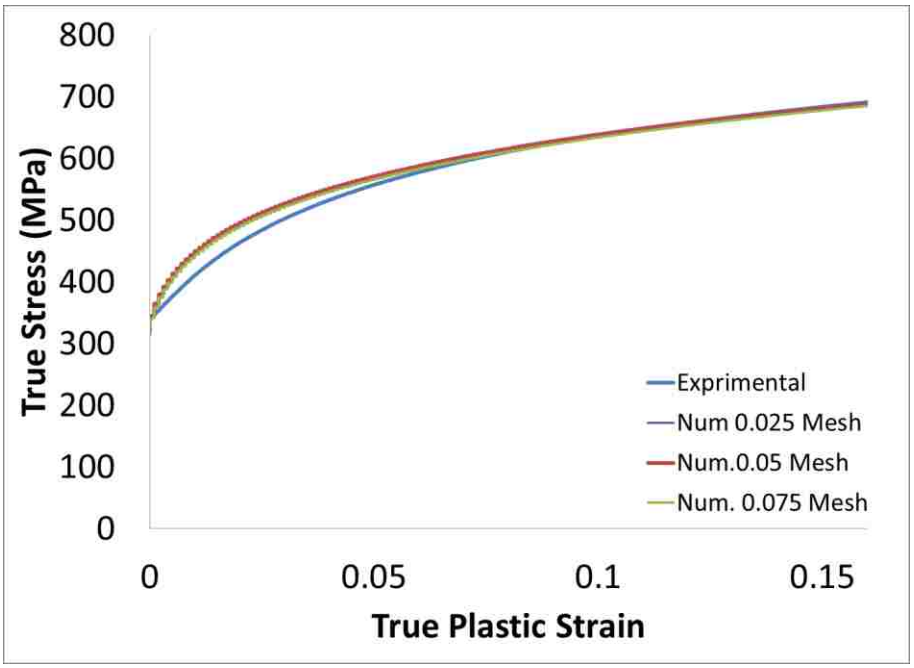

(b)

Figure 5-18 Effect of mesh size on modeling results for DP600 steel with 26 martensite islands inside the RVE: (a) flow curves of RVEs and (b) numerical and experimental flow curves of DP600 steel.

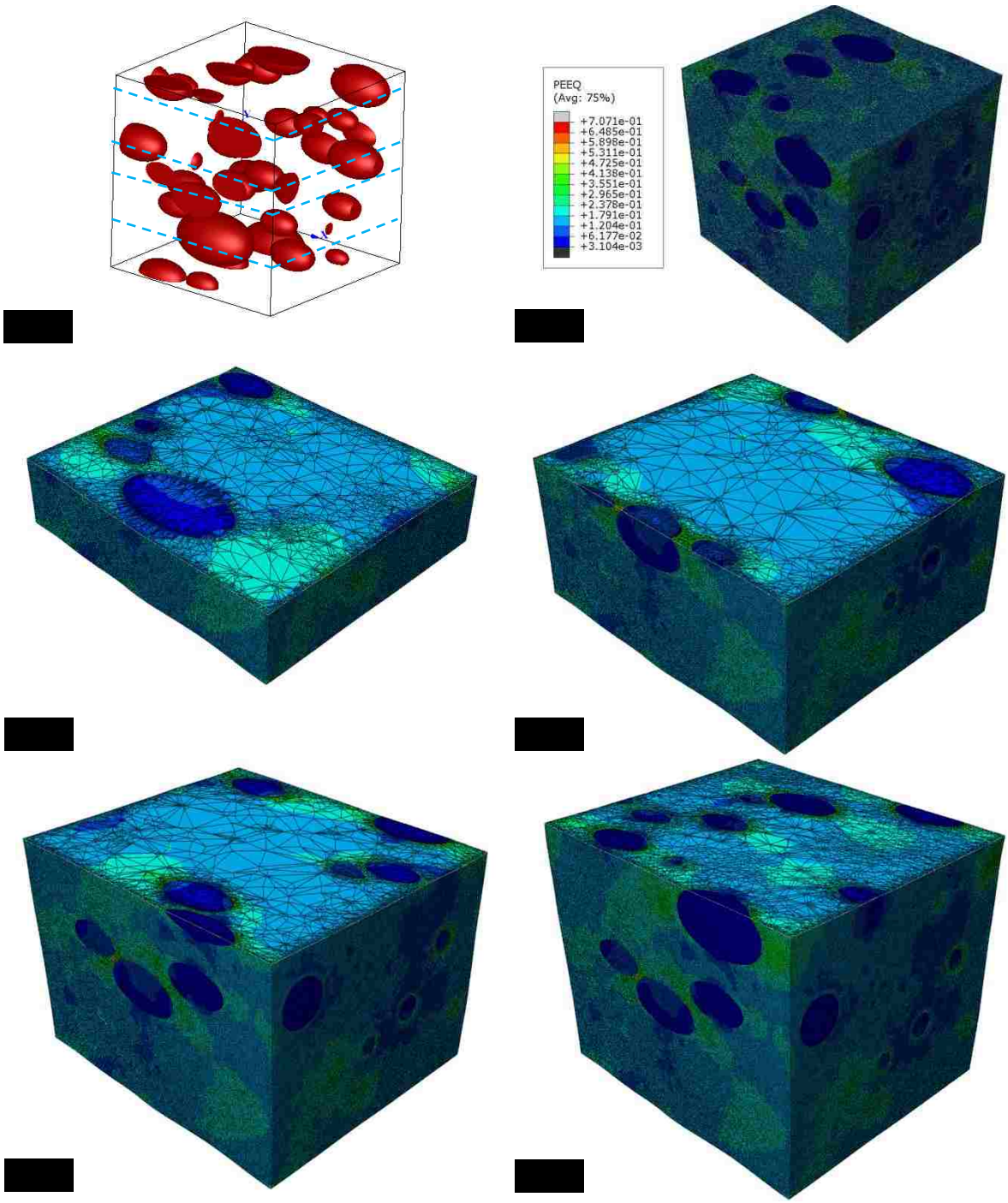

Figure 5-19 (a) RVE of DP500 with 26 martensite islands, (b) distribution of equivalent strain inside the RVE at ε=0.14 with mesh size of 0.025 µm, and (c-f) cross-sections of the RVE at different depths. The depths of sections are shown on the RVE.

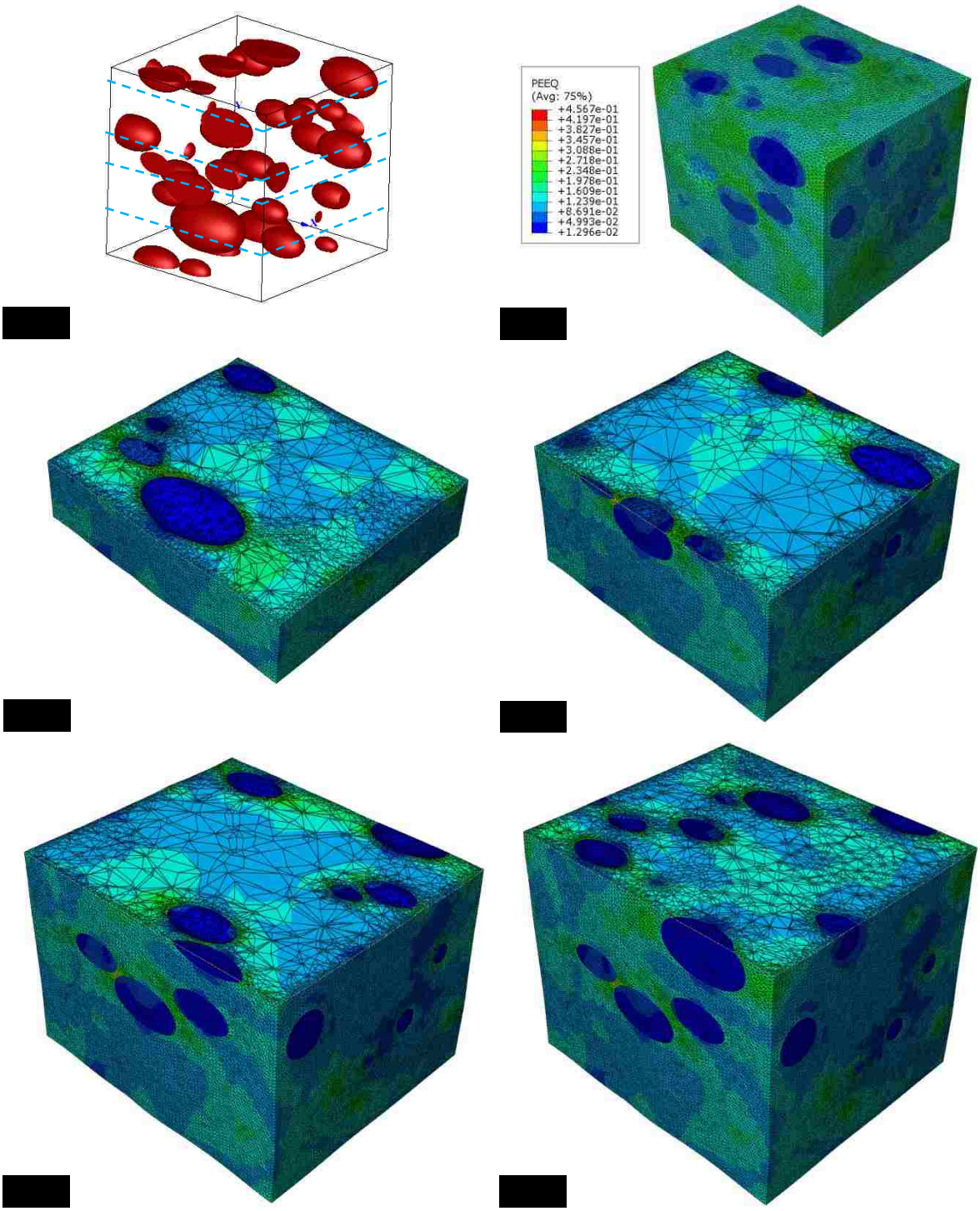

Figure 5-20 (a) RVE of DP500 with 26 martensite islands, (b) distribution of equivalent strain inside the RVE at ε=0.14 with mesh size of 0.05 µm, and (c-f) cross-sections of the RVE at different depths. The depths of sections are shown on the RVE.

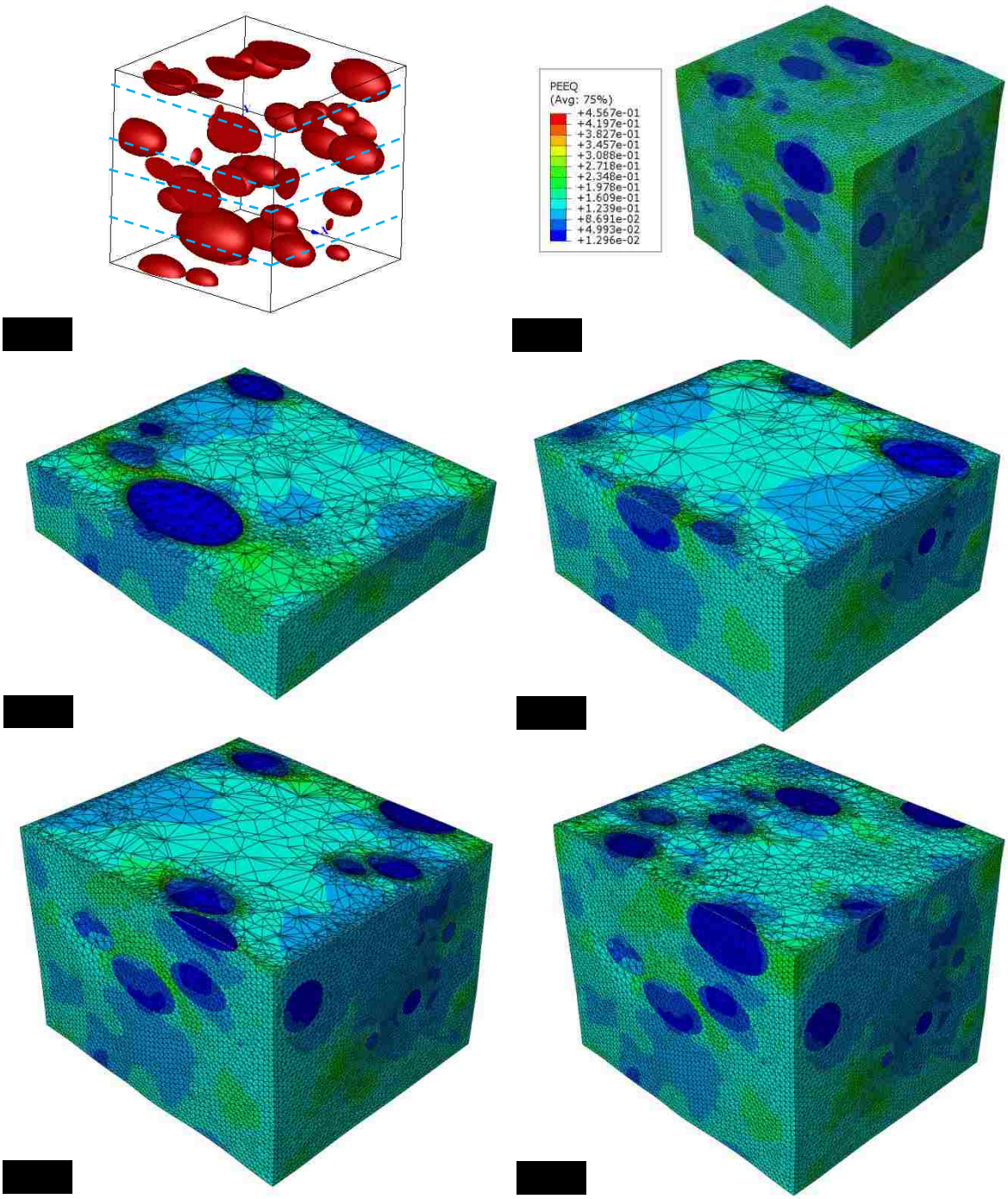

Figure 5-21 (a) RVE of DP500 with 26 martensite islands, (b) distribution of equivalent strain inside the RVE at ε=0.14 with mesh size of 0.075 µm, and (c-f) cross-sections of the RVE at different depths. The depths of sections are shown on the RVE.

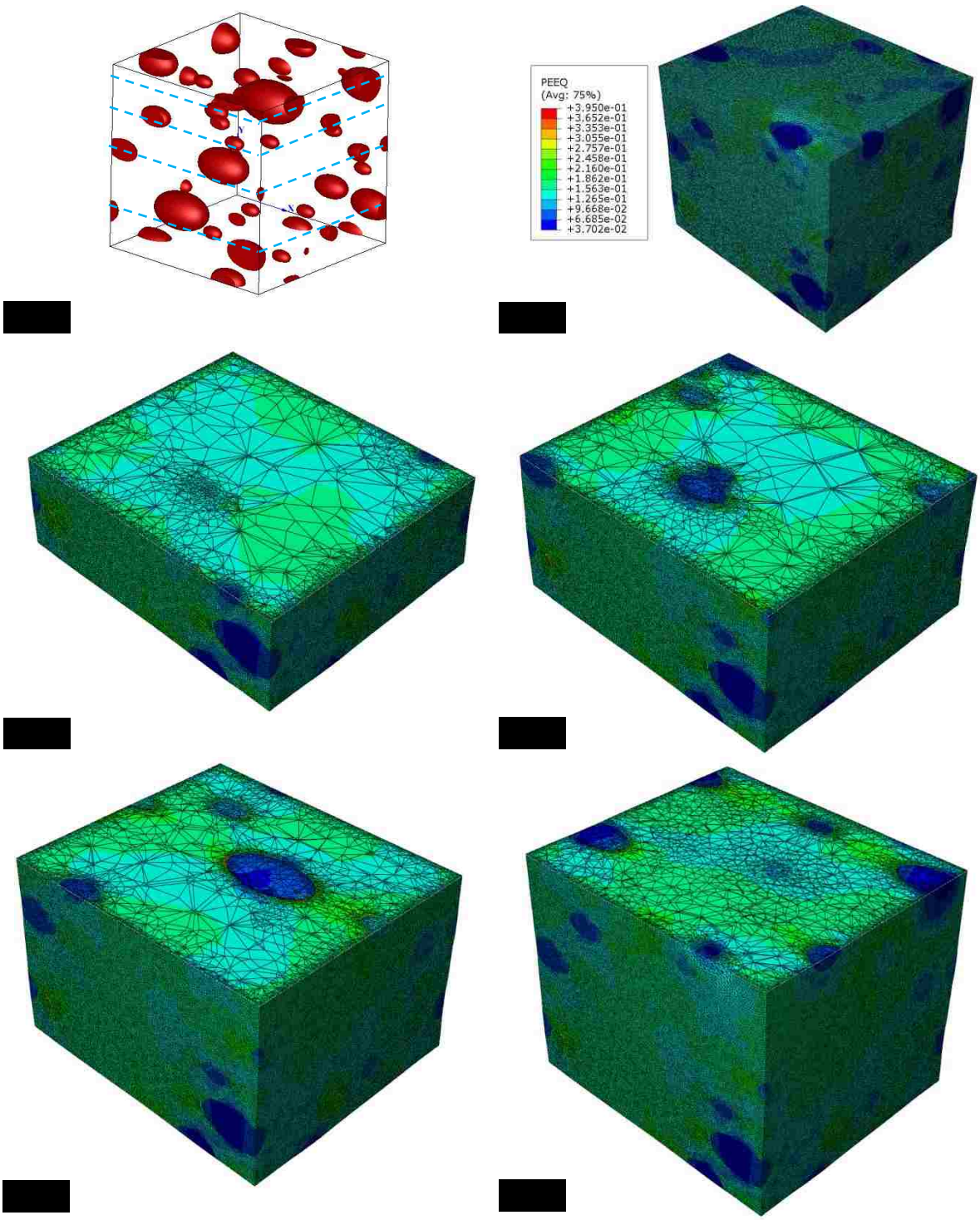

Figure 5-22 (a) RVE of DP600 with 26 martensite islands, (b) distribution of equivalent strain inside the RVE at ε=0.14 with mesh size of 0.025 µm, and (c-f) cross-sections of the RVE at different depths. The depths of sections are shown on the RVE.

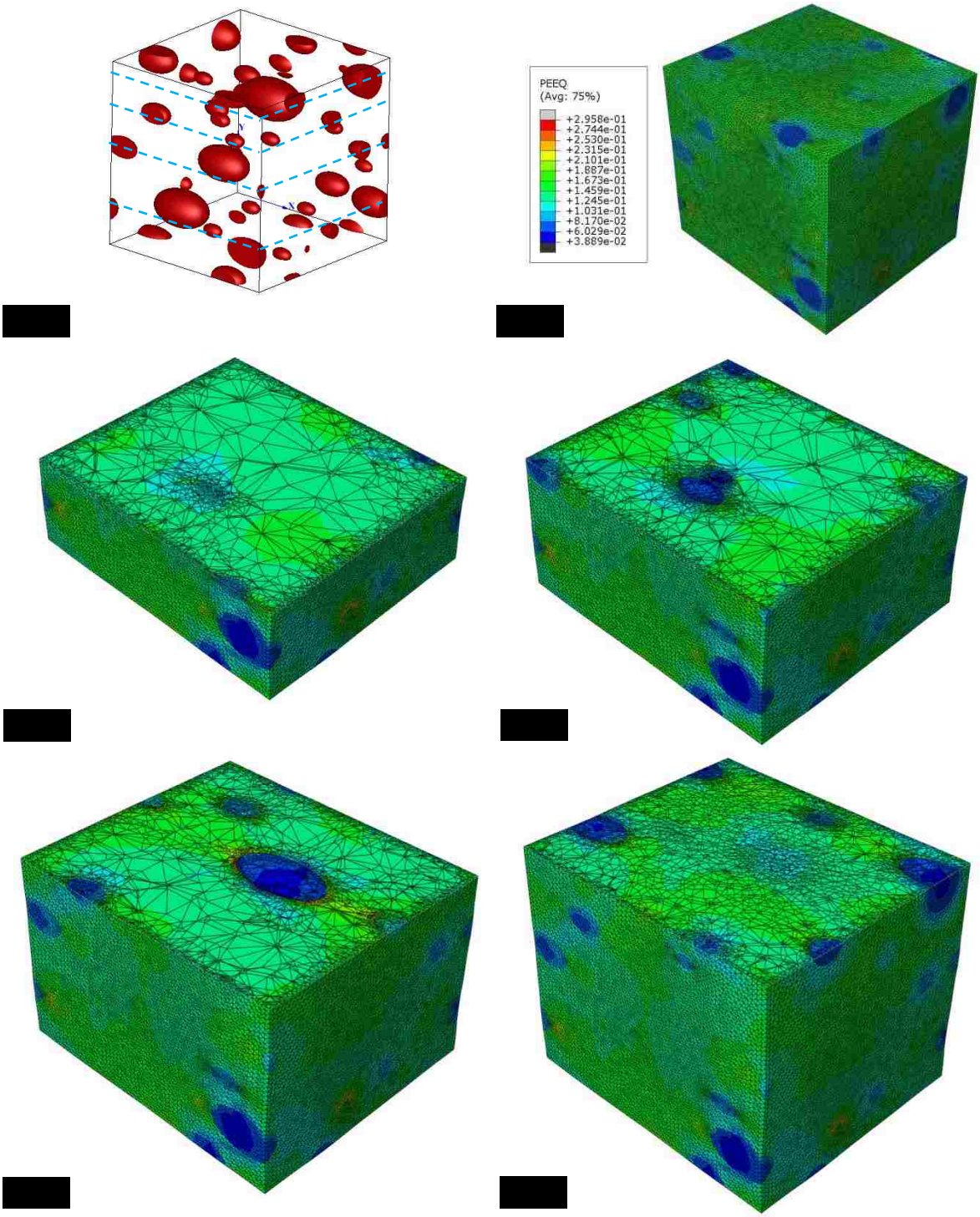

Figure 5-23 (a) RVE of DP600 with 26 martensite islands, (b) distribution of equivalent strain inside the RVE at ε=0.14 with mesh size of 0.05 µm, and (c-f) cross-sections of the RVE at different depths. The depths of sections are shown on the RVE.

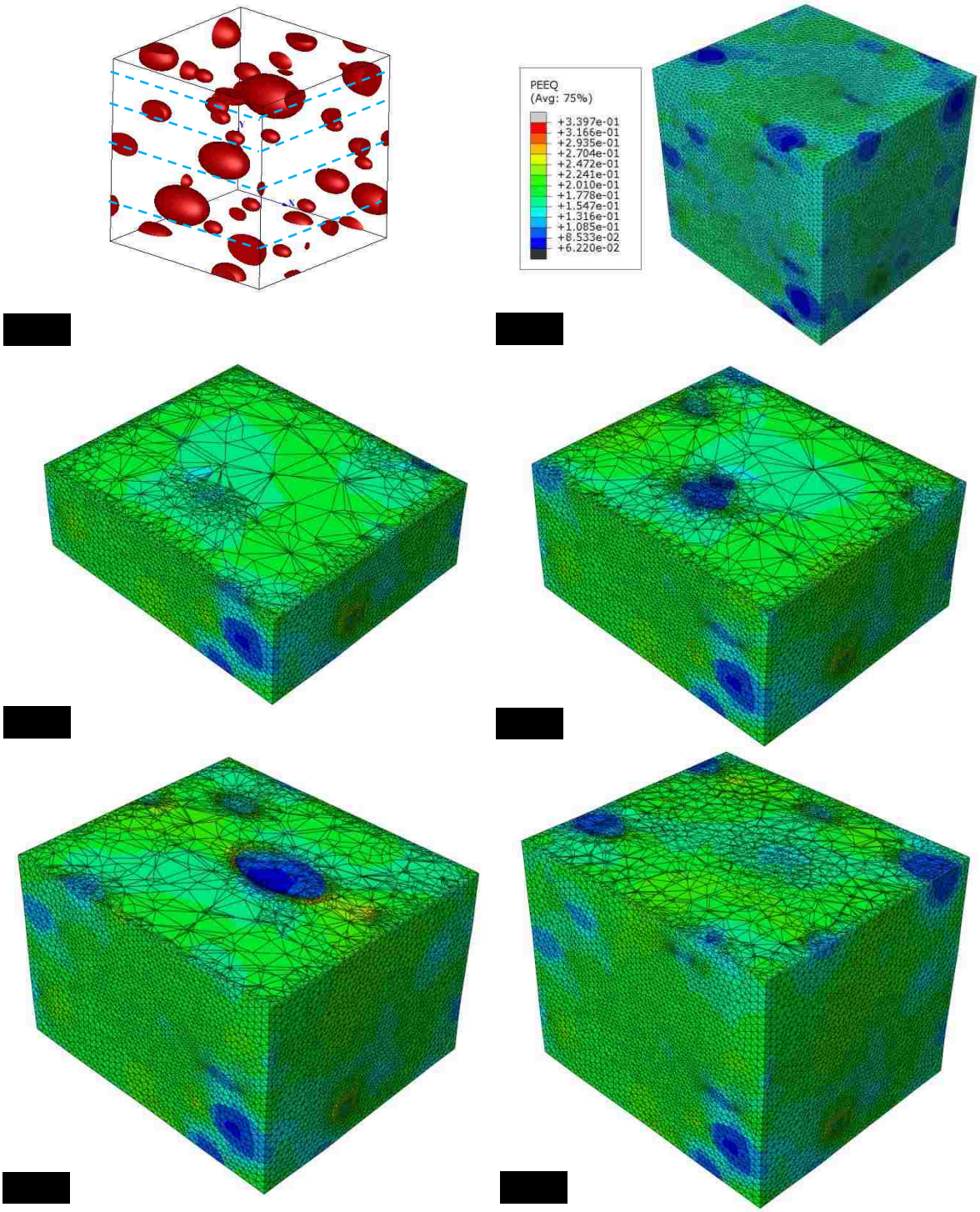

Figure 5-24 (a) RVE of DP600 with 26 martensite islands, (b) distribution of equivalent strain inside the RVE at ε=0.14 with mesh size of 0.075 µm, and (c-f) cross-sections of the RVE at different depths. The depths of sections are shown on the RVE.

5.3 Influence of Element Type on Numerical Flow Curves

C3D4 and C3D10 are the element types which are available in the Digimat software for 3D RVEs. C3D4 and C3D10 elements are shown in Figure 5-25. Both C3D4 and C3D10 are general purpose tetrahedral elements with one integration point and four integration points, respectively. The node numbering follows the convention of Figure 5-25.

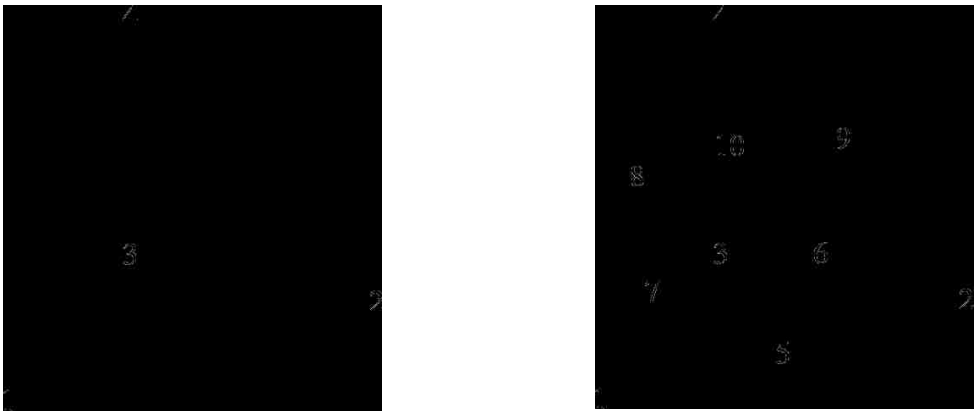

(a) **(b)**

Figure 5-25 Configuration of (a) C3D4 and (b) C3D10 elements

The effect of element type on the numerical flow curves was investigated by discretizing the DP500 and DP600 steel optimum RVEs with a mesh of either C3D4 or C3D10 elements. The flow curves that were obtained were practically identical.

The computer which was used to carry out the simulation was a Dell T3600 with Intel® Xeon® processor E5-1600 with six cores and 32 GB of 1600 MHz DDR3 memory. The modeling time when using C3D10 elements was at least 24 times greater than that when C3D4 elements were used. Modeling the DP600 RVE with 26 martensite islands using C3D10 elements and 0.050 µm mesh size required almost 99% of the computer memory; hence it was not possible to model larger RVEs with C3D10 elements since this type of element required more computer memory compared to C3D4 elements.

In conclusion, C3D4 is suggested as the best element type for the 3D RVEs. C3D4 elements were used by Ramazani et al [40] for 3D RVEs and provided accurate results.

5.4 Numerical Flow Curves of Constituents

During the micromechanical modeling of DP500 steel, ferrite was considered to be the matrix and martensite was the inclusion. In DP600 steel, the combination of ferrite and bainite was considered as the matrix and martensite islands as inclusions. The Digimat software provides separate numerical flow curves for the matrix and the inclusions in a RVE.

Figure 5-26 and Figure 5-27 show the flow curves of DP500 and DP600 steels and their constituents predicted from the optimum RVE. As it can be seen in these figures, ferrite was responsible for plastic deformation and martensite was responsible for strengthening the steel. In both steels, martensite islands generally experienced elastic deformation or small levels of plastic deformation.

As described in Section 3.4, due to stronger solid solution hardening and finer ferrite grain size, the strength of the matrix in DP600 steel was greater than the strength of the matrix in DP500 steel. Hence, as it can be seen in Figure 5-28, the flow curve of the matrix (ferrite + bainite) in DP600 steel lies above the flow curve of the matrix (ferrite) in DP500 steel. The ultimate tensile strengths of DP500 matrix and DP500 steel are 572 and 647 MPa, respectively. Also, the ultimate tensile strengths of DP600 matrix and DP600 steel are 644 and 687 MPa, respectively. It is evident that martensite had a greater contribution in strengthening the DP500 steel compared to the DP600 steel. Two reasons are attributed for the greater contribution of martensitic strengthening in DP500 steel compared to DP600 steels:

- As indicated in Table 3-4, since the carbon content of martensite in DP500 steel was 0.265 and in DP600 steel was 0.116, the strength of the martensite in DP500 steel was notably more than that in the DP600 steel.
- Since the martensite volume fraction in DP500 steel was 9.0 vol% and in DP600 steel it was only 4.7 vol%, it led to more strengthening in the DP500 steel.

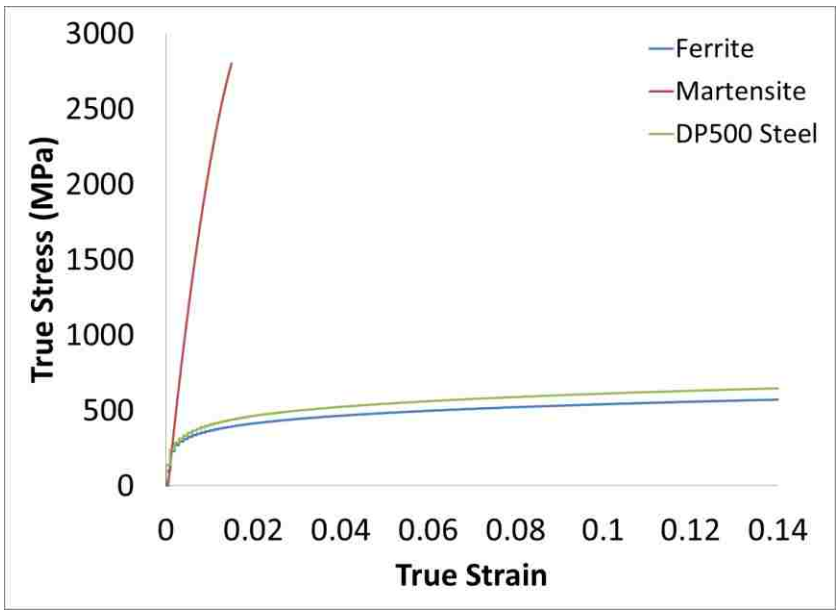

Figure 5-26 Flow curves of DP500 steel and its constituents as predicted by Digimat software

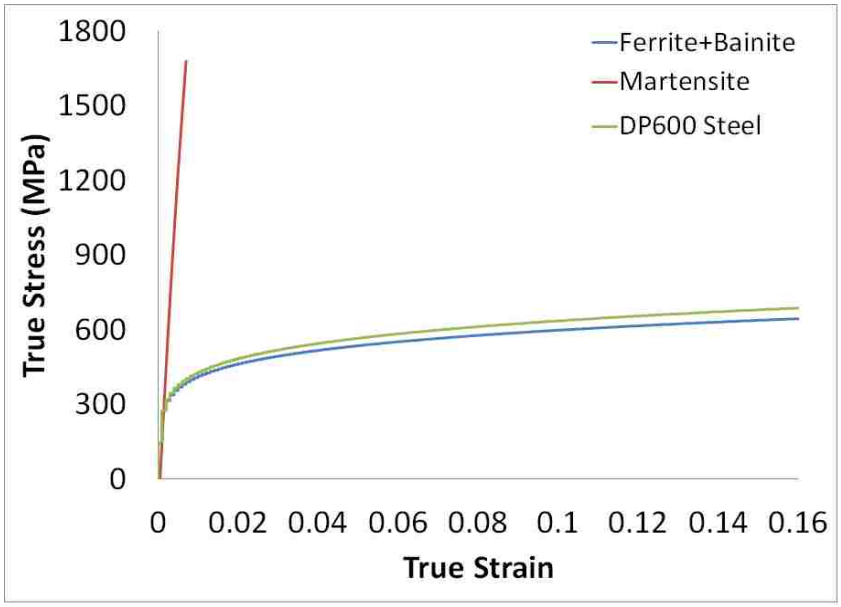

Figure 5-27 Flow curves of DP600 steel and its constituents as predicted by Digimat software

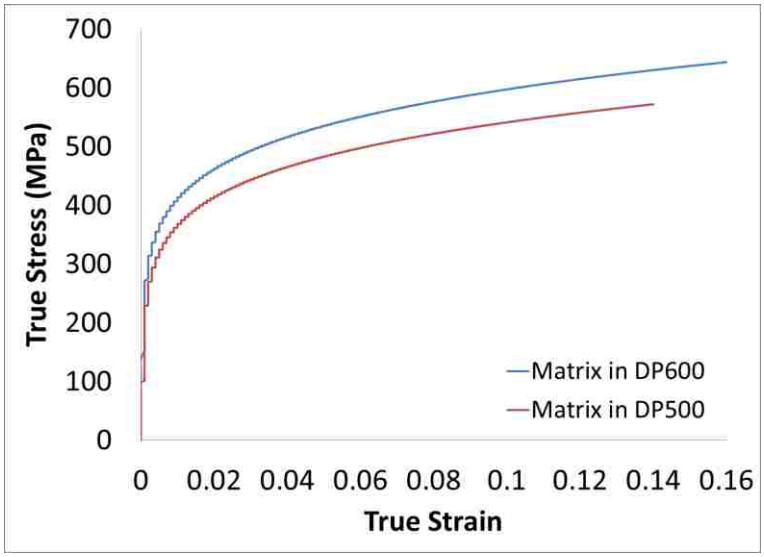

Figure 5-28 Flow curves of the matrix: ferrite in DP500 steel and ferrite + bainite in DP600 steel as predicted by Digimat software

5.5 Distribution of Stress and Strain in the Microstructure

To analyze the stress and strain distributions in the microstructures of DP500 and DP600 steels during a uniaxial tensile test, two 2D RVEs were generated in the Digimat software and a tensile test was simulated in ABAQUS. The DP500 and DP600 RVEs are shown in Figure 5-29. Simulation results are presented in Figure 5-30 for DP500 steels at true strains of 0.05, 0.09 and 0.14. Also, simulation results are presented in Figure 5-31 for DP600 steels at true strains of 0.04, 0.09 and 0.16.

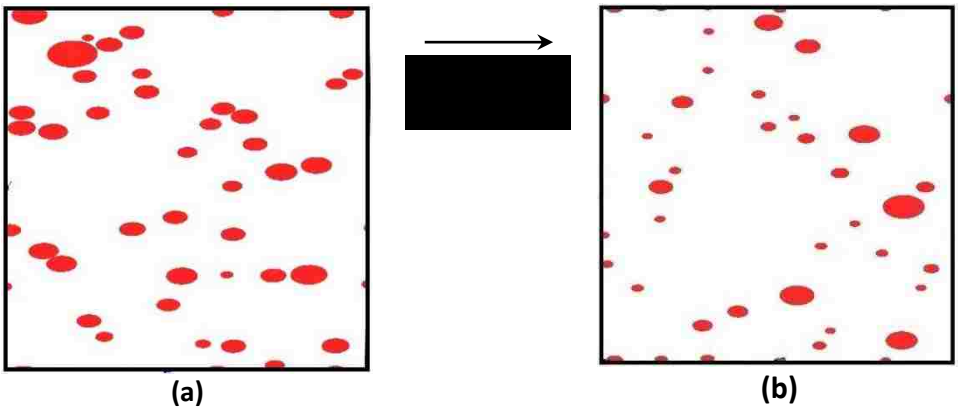

Figure 5-29 2D RVE of (a) DP500 steel contains 42 martensite islands, and (b) DP600 steel contains 37 martensite islands.

Considering the figures showing the strain distributions in the microstructures, in both DP500 and DP600 steels, the matrix deformed plastically and the martensite islands experienced elastic deformation or very small plastic strains.

As it can be seen, localization of deformation occurred due to the formation of 45° shear bands. Also, localized deformation happened at the ferrite/martensite interface. During plastic deformation, while the matrix tends to deform plastically, most of the martensite islands remain in elastic condition and resist the deformation of the matrix. Hence, work hardening increases at the interface and results in localized deformation. In terms of micromechanisms of plastic deformation, dislocations which are located inside ferrite grains move toward the grain boundaries. If a martensite island exists at the ferrite grain boundary it avoids further movement of dislocations and causes dislocation accumulation at the ferrite/martensite interface. Therefore, plastic strain localizes at the interface. As can be seen in Figure 5-26 and Figure 5-27, the difference between the mechanical properties of martensite and of the matrix is greater in DP500 steel than in DP600 steel. Hence, mechanical incompatibility of ferrite and martensite in DP500 steel is greater than in DP600 steel. This causes more localized deformation in the microstructure of DP500 steel compared to DP600 steel. According to the modeling results indicated in Figure 5-30(c) and Figure 5-31(c), the greatest localized strain in DP500 was 1.914 while it was 0.686 in DP600 steel.

Localized deformation causes microstructural damage. Since DP500 steel contains more martensite compared to DP600 steels, microstructural damage prior to necking was greater in DP500 steel. As a result, as it was indicated in Section 3.5, the void area fraction in DP500 and DP600 steels at true strain of 0.14 and 0.16 was approximately 0.18 and 0.12%, respectively.

Considering the figures showing the stress distributions in the microstructures of DP500 and DP600 steels, it can be seen that martensite islands carry the external loading. The von Mises stress in the martensite of DP500 and DP600 steels (Figure 5-30 and Figure 5-31) reached to 1.817 and 1.045 GPa, respectively. DP500 martensite islands could carry

greater stresses due to their higher strength compared to DP600 martensite. Also, the average von Mises stress in the matrix of DP500 and DP600 steels reaches 500-600 MPa and 600-700 MPa, respectively. In DP600 steel, the matrix reached greater stresses because of its greater strength compared to the DP500 matrix. Comparing the distribution of stress in DP600 steel at $\varepsilon=0.16$ and in DP500 steel at $\varepsilon=0.14$, it can be seen that the distribution of stress in the microstructure of DP600 steel is more homogenous due to better mechanical compatibility of the matrix and the martensite.

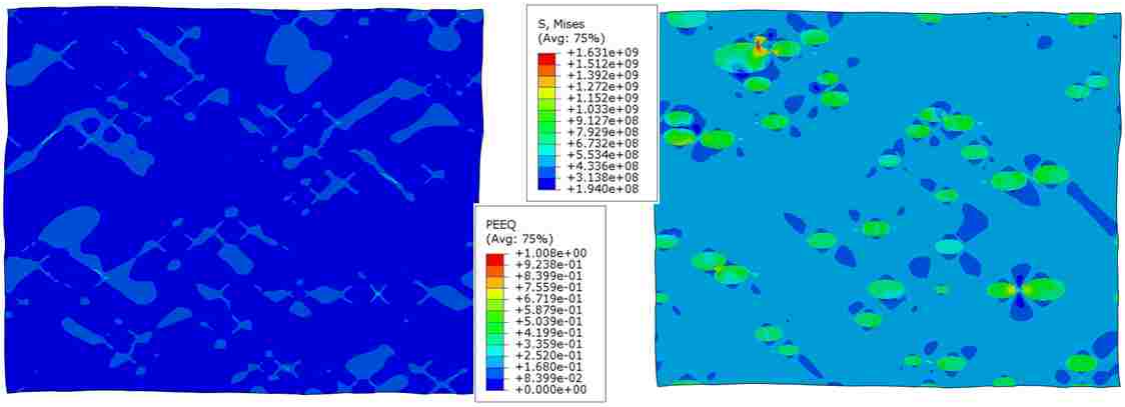

(a)

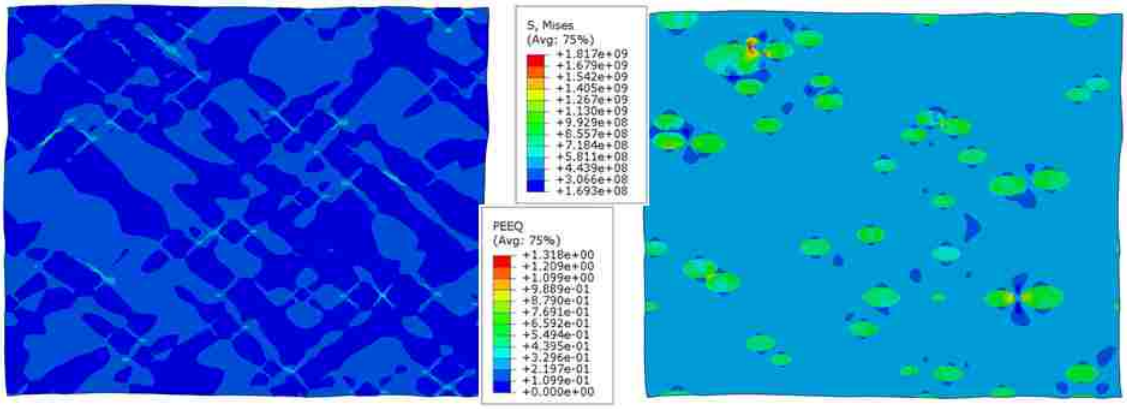

(b)

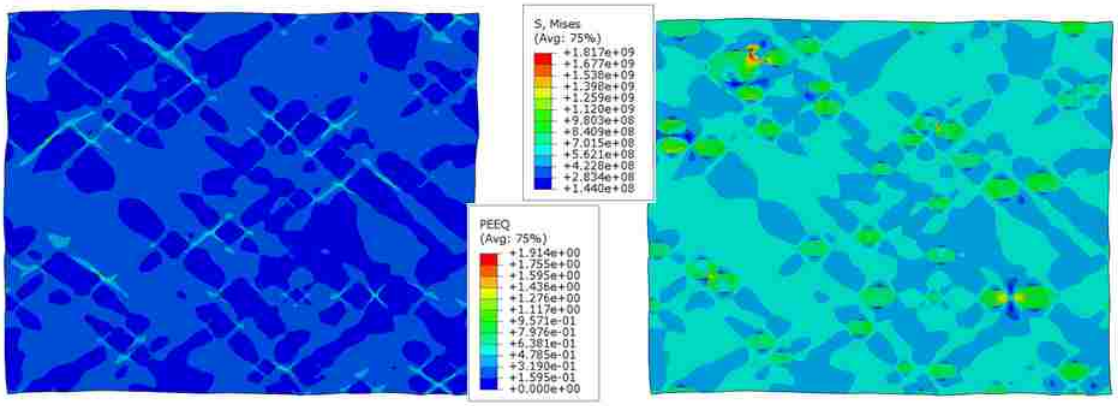

(c)

Figure 5-30 Distribution of strain (left) and stress (right) in DP500 RVE presented in Figure 5-29(a) at true strains of (a) 0.05, (b) 0.09, and (c) 0.14.

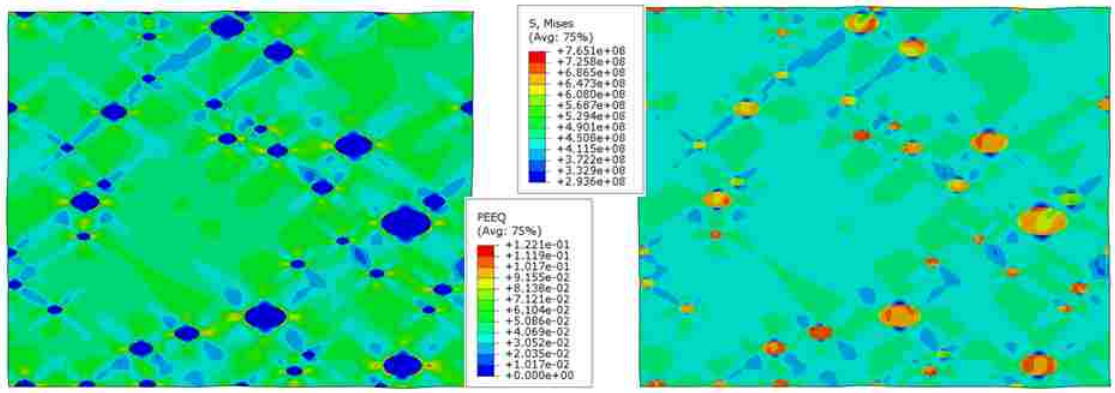

(a)

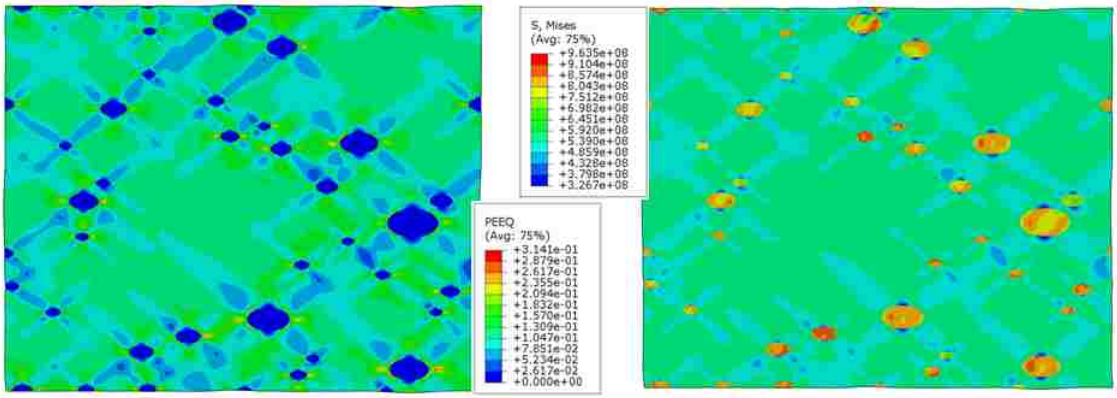

(b)

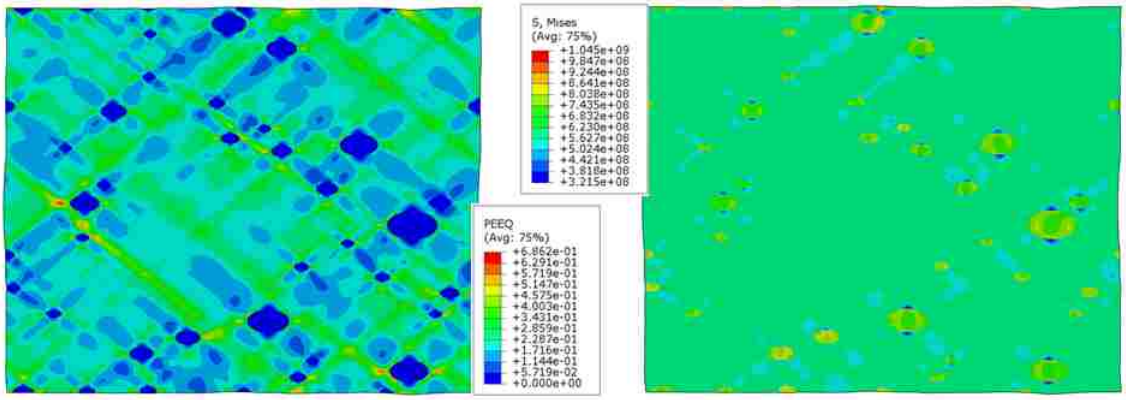

(c)

Figure 5-31 Distribution of strain (left) and stress (right) in DP600 RVE presented in Figure 5-29(b) at strains of (a) 0.04, (b) 0.09, and (c) 0.16.

When some martensite islands are located close to each other, as it can be seen in Figure 5-32(a), it causes stress concentration. Such localized stress occurred more frequently in DP500 steel compared to DP600 steel due to the greater martensite content. As it is shown in Figure 5-32(b) and (c) this can lead to the nucleation of voids inside the martensite islands or in the matrix.

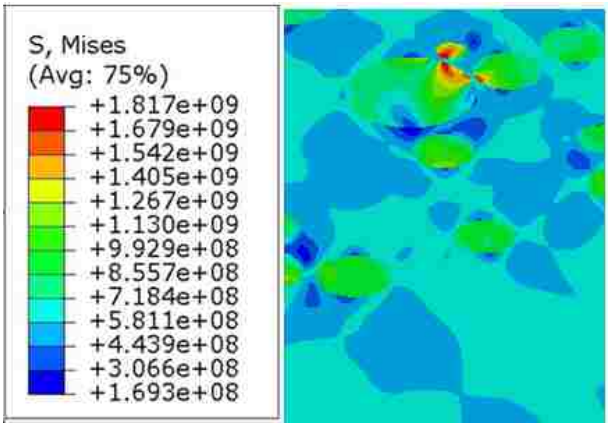

(a)

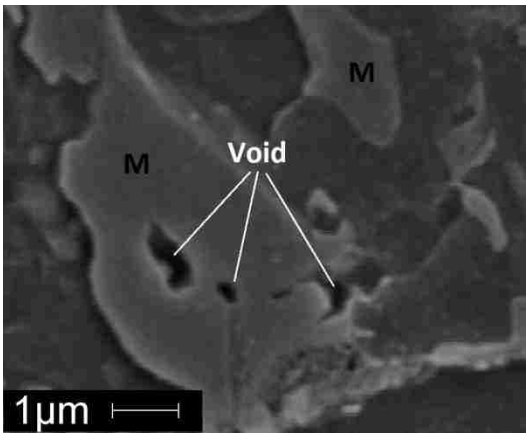

(b)

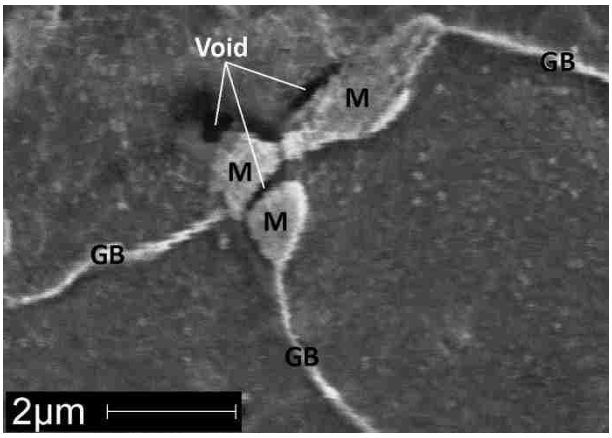

(c)

Figure 5-32 (a) Stress concentration in the RVE of DP500 steel where martensite islands lie close to each other, and nucleation of voids in the microstructure of DP500 steel (b) inside a single martensite island and (c) in the vicinity of three martensite islands. M and GB indicate martensite particles and grain boundaries, respectively.

6 Conclusions and Recommendations for Future Work

In this research, 3D RVE-based micromechanical modeling was carried out and the flow curves of DP500 and DP600 dual phase steels in uniaxial tension, were accurately predicted. Modeling was carried out up to the onset of necking.

RVEs were generated using the Digimat-FE software based on characteristics of real microstructures obtained from quantitative metallography. Since distributions of alloying element in the microstructure were approximately homogeneous and since void area fractions in the microstructure of the steels were negligible, the constitutive behaviour of each phase/constituent of DP500 and DP600 steels could be determined using Equation **2-10**. Application of boundary conditions and loading were carried out in Digimat-FE and the simulation of a tensile test on the RVE was performed in ABAQUS. To obtain numerical flow curves of the dual phase steels, first-order homogenization was carried out in Digimat-MF. The effects of RVE size and element type and size on the accuracy of modeling results were investigated. The following conclusions can be drawn from this research:

- The flow curve of DP500 steel was accurately predicted up to the onset of macroscopic plastic instability and the ultimate tensile strength of the steel was predicted with less than 0.3% error.
- In the case of DP600 steel, the numerical model accurately predicted the experimental flow curve of steel after a strain of 0.07. Since this DP600 steel exhibited yield point elongation but this was not considered in the constitutive behaviour of the individual constituents, it was not possible to accurately predict the flow curve of the steel at lower strains. However, at higher strain levels, the effect of yield phenomenon became negligible and the flow curve of DP600 steel was accurately predicted.
- The RVE sizes of 12.7x12.7x12.7 μm^3 and 7.9x7.9x7.9 μm^3 were found to be the optimum RVE sizes for DP500 and DP600 steel, respectively, and precisely predicted the flow curves of the steels.

- For both predicted flow curves of DP500 and DP600 steels, the optimum RVEs contained 26 martensite islands. The size distributions of martensite particles in these RVEs were very similar to those in the actual microstructures of DP500 and DP600 steels.
- The numerical simulation required that each RVE be discretized into a 3D finite element mesh. It was found that the optimum element size on the surface of RVE is 0.050 μm both in terms of the accuracy of the predicted results and in terms of minimizing the computation time.
- Both C3D4 and C3D10 element types led to similar accuracy of results. However, C3D10 elements significantly increased the computation time (at least 24 times more) and required more computational resources. Therefore, C3D4 elements are recommended as the most suitable element type.
- 2D RVE-based models showed that the matrix in DP500 and DP600 steels is responsible for plastic deformation and the martensite islands are responsible for carrying external loads. This is consistent with the mechanical metallurgy of dual phase steels.
- The distribution of stress was more homogenous in the microstructure of DP600 steel compared to DP500 steel due to greater mechanical compatibility of phases in the microstructure of DP600 steel.
- It was observed that localization of deformation occurred in the microstructures of DP500 and DP600 steels due to the formation of shear bands and mechanical incompatibility of ferrite and martensite. Interfacial localized deformation was greater in DP500 steel since mechanical incompatibility of ferrite and martensite was greater in DP500 steel compared to DP600 steel.
- Localized deformation also occurred in the microstructure of steels when martensite islands were located near to each other. This might cause nucleation of voids inside the martensite islands or in the matrix.

This research had made several contributions to the micromechanical modeling of dual phase steels. Nevertheless, further work is recommended in the following areas:

- The methodology presented in this thesis can be used to predict flow curves of dual phase steels with martensite contents less than 10 vol%. In higher strength grades of dual phase steels such as DP780 and DP980 steels, the volume fraction of martensite may reach 35 vol%. As it was shown in Figure 2-1, in this case the martensite is not separated into isolated islands but it rather form a continuous network throughout the microstructure. Hence, the quantitative metallography procedure which was used in this research, i.e. determination of the aspect ratio and size distribution of martensite islands, is not applicable to the morphology of martensite in the microstructure of DP780 and DP980 steels. Therefore, it is recommended that a quantitative method which can determine the morphological features of martensite in higher grades of dual phase steel be investigated in order to generate RVEs similar to the actual microstructures of these grades of steel.
- Another recommendation for further studies is to investigate the effect of yield point phenomenon on the constitutive behaviour of ferrite, bainite and martensite in dual phase steels.
- The parameters in Equation **2-10** can be determined without ambiguity. Therefore it is a suitable constitutive equation for predicting flow curves of the different phases under quasi-static forming conditions. For industrial metal forming processes that are carried out at higher strain rates, it is recommended to develop a similar equation that is dependent on strain rate. Hence, it will be applied more precisely for forming processes such as electrohydraulic forming.

References

[1] Committee on International Iron & Steel Institute Committee on Automotive Applications, 2006, “Advanced high strength steel (AHSS) application guidelines”, Available: http://autotechnika.hu/archiv/AHSS.pdf, DOA: 11/30/2014.

[2] Kren, L., “Developments in Making GigaPascal-Strength Steels”. Available: http://www.metalformingfacts.com/industry-news/developments-gigapascal-strength-steels.html, DOA: 11/30/2014.

[3] Pareige, P., 2013, “Irradiation effects in structural components of nuclear reactor: an experimental nanoscale point of view”. Available: http://mecamat2013.lmgc.univ-montp2.fr/presentations.htm, DOA: 11/30/2014.

[4] Williams, E. W., and Davies, L. K., 1963, “Recent developments in annealing”, ISI Spec. Rep. 79.

[5] Samei, J., 2013, “Multi-scale Characterization of Hyperplasticity and Failure in Dual Phase Steels Subject to Electrohydraulic Forming”, PhD Dissertation, University of Windsor.

[6] Rashid, M. S., 1981, “Dual Phase Steels”, Annu. Rev. Mater. Sci., **11**(1), pp. 245–266.

[7] Llewellyn, D. T., and Hudd, R. C., 1998, Steels : Metallurgy and Applications, Reed Educational and Professional Publishing Ltd., London, UK.

[8] Waterschoot, T., Cooman, B. C., and Vanderschueren, D., 2001, “Influence of run-out table cooling patterns on transformation and mechanical properties of high strength dual phase and ferrite–bainite steels", Ironmaking and steelmaking, **28**(1), p. 185-190.

[9] Zeytin, H. K., Kubilay, C., and Aydin, H., 2008, “Investigation of dual phase transformation of commercial low alloy steels: Effect of holding time at low inter-critical annealing temperatures”, Mater. Lett., **62**(17-18), pp. 2651–2653.

[10] Balliger, N.K., Gladman, T., 1981. Work hardening of dual-phase steels. Met. Sci., **15**(3), 95–108.

[11] Smallman, R. E., and Bishop, R. J., 1999, Modern Physical Metallurgy and Materials Engineering, Butterworth-Heinemann, Oxford, UK.

[12] Hall, E. O., 1951, “The Deformation and Ageing of Mild Steel: III Discussion of Results”, Proc. Phys. Soc. Sect. B, **64**(9), pp. 747–753.

[13] Petch, N. J., 1953, “The cleavage strength of polycrystals”, J. Iron Steel Inst., **174**, pp. 25-28

[14] Pickering, F. B., 1978, Physical Metallurgy and the Design of Steels, Applied Science Publishers LTD, London.

[15] Gladman, T., 1997, The Physical Metallurgy of Microalloyed Steels, The Institute of Materials,The University Press, Cambridge, London.

[16] Krauss, G., 1978, “Martensitic Transformation, Structure and Properties in Hardenable Steels”, Hardenability Concepts With Applications to Steel, D.V. Doane and J.S. Kirkaldy, eds., AIME, Warrendale, PA, pp. 229–248.

[17] Leslie, W. C., 1991, The physical metallurgy of steels, TechBooks, Herndon, Virginia, US.

[18] Kim, S., and Lee, S., 2000, “Effects of martensite morphology and volume fraction on quasi-static and dynamic deformation behavior of dual- phase steels”, Metall. Mater. Trans. A, **31**(7), pp. 1753–1760.

[19] Hwang, B.-C., Cao, T.-Y., Shin, S. Y., Kim, S.-H., Lee, S.-H., and Kim, S.-J., 2005, “Effects of ferrite grain size and martensite volume fraction on dynamic deformation behaviour of 0·15C–2·0Mn–0·2Si dual phase steels”, Mater. Sci. Technol., **21**(8), pp. 967–975.

[20] Bag, A., Ray, K. K., and Dwarakadasa, E. S., 1999, “Influence of martensite content and morphology on tensile and impact properties of high-martensite dual-phase steels”, Metall. Mater. Trans. A, **30**(5), pp. 1193–1202.

[21] Byun, T. S., and Kim, I. S., 1993, “Tensile properties and inhomogeneous deformation of ferrite-martensite dual-phase steels”, J. Mater. Sci., **28**(11), pp. 2923–2932.

[22] Gündüz, S., 2009, “Effect of chemical composition, martensite volume fraction and tempering on tensile behaviour of dual phase steels”, Mater. Lett., **63**(27), pp. 2381–2383.

[23] Kang, S.-M., and Kwon, H., 1987, “fracture behavior of intercritically treated complex structure in medium-carbon 6Ni steel”, Metall. Trans. A, **18**(9), pp. 1587–1592.

[24] Ajmal, M., Tindyala, M. A., and Priestner, R., 2009, “Effect of controlled rolling on the martensitic hardenability of dual phase steel”, Int. J. Miner. Metall. Mater., **16**(2), pp. 165–169.

[25] Spiech, G. R., and Wadimont, H., 1968, “Yield Strength and Transformation Substructure of Low-Carbon Martensite”, Iron Steel Inst., **206**, pp. 385–392.

[26] Winchell, P. G., and Cohen, M., 1962, “The Strength of Martensite”, Trans. ASM, **33**, pp. 347–361.

[27] Speich, G. ., and Miller, R. L., 1979, “Mechanical Properties of Ferrite-Martensite Steels”, Structure and Properties of Dual-Phase Steels, R.A. Kot, and I. Morris, eds., TMS-AIME, New York, pp. 145–182.

[28] Durand-Charre, M., 2004, Microstructure of Steels & Cast Irons (Engineering Materials and Processes), Springer, Berlin, Germany.

[29] Bhadeshia, H. K. D., 2001, Bainite in steels, transformation, microstructure and properties, Institute of Materials, London, UK.

[30] Bhadeshia, H. K. D. H., 1990, “Model for transition from upper to lower bainite”, Materials Science and Technology, **6**, pp. 592–603.

[31] Bourell, D. L., and Rizk, a., 1983, “Influence of martensite transformation strain on the ductility of dual-phase steels”, Acta Metall., **31**(4), pp. 609–617.

[32] Liedl, U., Traint, S., and Werner, E. a., 2002, “An unexpected feature of the stress–strain diagram of dual-phase steel”, Comput. Mater. Sci., **25**(1-2), pp. 122–128.

[33] Balliger, N. K., and Gladman, T., 1981, “Work hardening of dual-phase steels”, Met. Sci., **15**, pp. 95–108.

[34] Speich, G. R., and Miller, R. L., 1979, “Mechanical properties of ferrite-martensite steels”, in Structure and properties of dual-phase steels, American Institute of Mining, Metallurgical, and Petroleum Engineers, pp. 145–182.

[35] Uthaisangsuk, V., Prahl, U., and Bleck, W., 2011, “Modelling of damage and failure in multiphase high strength DP and TRIP steels”, Eng. Fract. Mech., **78**(3), pp. 469–486.

[36] Thomser, C., Uthaisangsuk, V., and Bleck, W., 2009, “Influence of martensite distribution on the mechanical properties of dual phase steels: experiments and simulation”, Steel Research International, **80**(8), pp. 582-587.

[37] Ramazani, A., Mukherjee, K., Abdurakhmanov, A., Prahl, U., Schleser, M., Reisgen, U., and Bleck, W., 2014, “Micro–macro-characterisation and modelling of mechanical properties of gas metal arc welded (GMAW) DP600 steel,” Mater. Sci. Eng. A, **589**, pp. 1–14.

[38] Al-Abbasi, F., 2004, "Micromechanical Modeling of Dual Phase Steels", PhD Dissertation, McGill University.

[39] Paul, S. K., 2013, “Effect of material inhomogeneity on the cyclic plastic deformation behavior at the microstructural level: micromechanics-based modeling of dual-phase steel,” Model. Simul. Mater. Sci. Eng., **21**(5), p. 055001.

[40] Ramazani, A., Mukherjee, K., Quade, H., Prahl, U., and Bleck, W., 2013, “Correlation between 2D and 3D flow curve modelling of DP steels using a microstructure-based RVE approach,” Mater. Sci. Eng. A, **560**, pp. 129–139.

[41] Mori, T., and Tanaka, K., 1973, “Average stress in matrix and avegare elastic energy of materials with misfitting inclusions,” Acta Metall., **21**, pp. 571–574.

[42] Lewis, A. C., and Geltmacher, A. B., 2006, “Image-based modeling of the response of experimental 3D microstructures to mechanical loading,” Scr. Mater., **55**(1), pp. 81–85.

[43] Brands, D., Schröder, J., Balzani, D., Dmitrieva, O., and Raabe, D., 2011, "On the Reconstruction and Computation of Dual-Phase Steel Microstructures Based on 3D EBSD Data," Proc. Appl. Math. Mech., **11**(1), pp. 503–504.

[44] Rodriguez, R., and Gutierrez, I., 2003, "Unified formulation to predict the tensile curves of steels with different microstructures," Mater. Sci. Forum, **426-432**(5), pp. 4525–4530.

[45] Paul, S. K., and Kumar, A., 2012, "Micromechanics based modeling to predict flow behavior and plastic strain localization of dual phase steels," Comput. Mater. Sci., **63**, pp. 66–74.

[46] Ramazani, A., Pinard, P. T., Richter, S., Schwedt, A., and Prahl, U., 2013, "Characterisation of microstructure and modelling of flow behaviour of bainite-aided dual-phase steel," Comput. Mater. Sci., **80**, pp. 134–141.

[47] Sodjit, S., and Uthaisangsuk, V., 2011, "High Strength Dual Phase Steels and Flow Curve Modeling Approach," The Second TSME International Conference on Mechanical Engineering, Krabi, Thailand.

[48] Sodjit, S., and Uthaisangsuk, V., 2012, "A micromechanical flow curve model for dual phase steels," J. Met. Mater. Miner., **22**(1), pp. 87–97.

[49] Ramazani, a., Mukherjee, K., Prahl, U., and Bleck, W., 2012, "Modelling the effect of microstructural banding on the flow curve behaviour of dual-phase (DP) steels," Comput. Mater. Sci., **52**(1), pp. 46–54.

[50] Gil Sevillano, J., 1993, "Flow stress and work hardening," Plastic Deformation of Materials, H. Mughrabi, ed., Weinheim (FRG), pp. 19–88.

[51] Buessler, P., 1999, ECSC steel RTD first report.

[52] Bergstrom, Y., 1970, "A dislocation model for the stress-strain behaviour of polycrystalline α-Fe with special emphasis on the variation of the densities of mobile and immobile dislocations," Materials Science and Engineering, **5**(4), pp. 193–200.

[53] Bouaziz, O., Irsid, P. B., Group, U., and Usinor, G., 2002, "Mechanical behaviour of multiphase materials : an intermediate mixture law without fitting parameter," pp. 71–77.

[54] Kouznetsova, V., 2002, "Computational homogenization for the multi-scale analysis of multi-phase materials," Eindhoven University of Technology, The Netherlands.

[55] Terada, K., Hori, M., Kyoya, T., and Kikuchi, N., 2000, "Simulation of the multi-scale convergence in computational homogenization approaches," Int. J. Solids Struct., **37**(16), pp. 2285–2311.

[56] Sluis, O. Van Der, Schreurs, P. J. G., Brekelmans, W. A. M., and Meijer, H. E. H., 2000, "Overall behaviour of heterogeneous elastoviscoplastic materials: effect of microstructural modelling," Mechanics of Materials, **32**, pp. 449-462.

[57] Kouznetsova, V., Geers, M. G. D., and Brekelmans, W. a. M., 2002, “Multi-scale constitutive modelling of heterogeneous materials with a gradient-enhanced computational homogenization scheme,” Int. J. Numer. Methods Eng., **54**(8), pp. 1235–1260.

[58] Hill, R., 1963, “Elastic properties of reinforced solids: some theoretical principles,” J. Mech. Phys. Solids, **11**, pp. 357–372.

[59] Hill, R., 1984, “On macroscopic effects of heterogeneity in elastoplastic media at finite strain,” Math. Proc. Cambridge Philos. Soc., **95**, pp. 481–494.

[60] Nemat-Nasser, S., 1999, “Averaging theorems in finite deformation plasticity,” Mech. Mater., **31**, pp. 493–523.

[61] Huper, T., Shigeru, E., Nobuyuki, I., and Kiochi, O., 1999, “Effect of volume fraction of constituent phases on the stress-strain relationship of dual phase steels,” ISIJ Int., **39**(3), pp. 288–294.

[62] Ishikawa, N., Parks, D. M., Socrate, S., and Kurihara, M., 2000, “Micromechanical modeling of ferrite-pearlite steels using finite element unit cell models,” ISIJ Int., **40**(11), pp. 1170–1179.

[63] Al-Abbasi, F. M., and Nemes, J. A., 2003, “Micromechanical modeling of dual phase steels,” Int. J. Mech. Sci., **45**(9), pp. 1449–1465.

[64] Al-Abbasi, F. M., and Nemes, J. A., 2003, “Micromechanical modeling of the effect of particle size difference in dual phase steels,” Int. J. Solids Struct., **40**(13-14), pp. 3379–3391.

[65] Marvi-Mashhadi, M., Mazinani, M., and Rezaee-Bazzaz, A., 2012, “FEM modeling of the flow curves and failure modes of dual phase steels with different martensite volume fractions using actual microstructure as the representative volume,” Comput. Mater. Sci., **65**, pp. 197–202.

[66] Sodjit, S., and Uthaisangsuk, V., 2012, “Microstructure based prediction of strain hardening behavior of dual phase steels,” Mater. Des., **41**, pp. 370–379.

[67] Paul, S. K., 2013, “Real microstructure based micromechanical model to simulate microstructural level deformation behavior and failure initiation in DP 590 steel,” Mater. Des., **44**, pp. 397–406.

[68] ASTM E112, 2013, Standard Test Methods for Determining Average Grain Size.

[69] Abbaschian, R., Abbaschian, L., and Reed-Hill, R. E., 2008, Physical metallurgy principles, Cengage Learning, Stamford, CT, US.

[70] ASTM E8/E8M, 2013, Standard Test Methods for Tension Testing of Metallic Materials.

[71] Kumar, A., Singh, S. B., and Ray, K. K., 2008, “Influence of bainite/martensite-content on the tensile properties of low carbon dual-phase steels,” Mater. Sci. Eng. A, **474**(1-2), pp. 270–282.

[72] Mazinani, M., and Poole, W. J., 2007, “Effect of Martensite Plasticity on the Deformation Behavior of a Low-Carbon Dual-Phase Steel,” Metall. Mater. Trans. A, **38**(2), pp. 328–339.

[73] Hollomon, J. H., 1945, “Tensile Deformation,” Trans. AIME, **162**, pp. 269–290.

Appendix A

Calculation of the flow behaviour of ferrite, martensite and bainite in DP500 and DP600 steels is presented in the following. Results are used in Section 4.1.

A1. Flow Behaviour of Ferrite in DP500 Steel

$$\sigma_0 = 77+80(1.83)+60(0.02)+45(0.01)+60(0.03)+11(0.01)=226.96 \text{ (MPa)}$$

$$\Delta\sigma_c^f = 5000\times 0.007 = 35 \text{ (MPa)}$$

$$\sigma = 226.96+35+0.33\times 3\times 80000\times \sqrt{2.5x10^{-10}} \times \sqrt{\frac{1-\exp(-3\times(10^{-5}/5.54\times10^{-6})\times\varepsilon)}{(10^{-5}/5.54\times10^{-6})\times(5.54\times10^{-6})}} =$$

$$= 261.96+1.25\sqrt{\frac{1-\exp(-5.41\varepsilon)}{10^{-5}}}$$

A2. Flow Behaviour of Martensite in DP500 Steel

$$\sigma_0 = 77+80(1.83)+60(0.02)+45(0.01)+60(0.03)+11(0.01)=226.96 \text{ (MPa)}$$

$$\Delta\sigma_c^m = 3065\times 0.265-161 = 651.23 \text{ (MPa)}$$

$$\sigma = 226.96+651.23+0.33\times 3\times 80000\times \sqrt{2.5x10^{-10}} \times \sqrt{\frac{1-\exp(-3\times 41\times\varepsilon)}{41\times(3.8\times10^{-8})}} =$$

$$= 878.19+1.25\sqrt{\frac{1-\exp(-123\varepsilon)}{10^{-5}}}$$

A3. Flow Behaviour of Ferrite in DP600 Steel

$$\sigma_0 = 77+80(1.497)+60(0.175)+80(0.057)+45(0.015)+60(0.181)+11(0.214)=225.71 \text{ (MPa)}$$

$$\Delta\sigma_c^f = 5000\times 0.006 = 30 \text{ (MPa)}$$

$$\sigma = 225.71 + 30 + 0.33 \times 3 \times 80000 \times \sqrt{2.5x10^{-10}} \times \sqrt{\frac{1 - \exp(-3 \times (10^{-5} / 4.0 \times 10^{-6}) \times \varepsilon)}{(10^{-5} / 4.0 \times 10^{-6}) \times (4.0 \times 10^{-6})}} =$$

$$= 225.71 + 1.25\sqrt{\frac{1 - \exp(-7.5\varepsilon)}{10^{-5}}}$$

A4. Flow Behaviour of Martensite in DP600 Steel

$$\sigma_0 = 77 + 80(1.497) + 60(0.175) + 80(0.057) + 45(0.015) + 60(0.181) + 11(0.214) = 225.71 \text{ (MPa)}$$

$$\Delta\sigma_c^m = 3065 \times 0.116 - 161 = 194.54 \text{ (MPa)}$$

$$\sigma = 225.71 + 194.54 + 0.33 \times 3 \times 80000 \times \sqrt{2.5x10^{-10}} \times \sqrt{\frac{1 - \exp(-3 \times 41 \times \varepsilon)}{41 \times (3.8 \times 10^{-8})}} =$$

$$= 420.25 + 1.25\sqrt{\frac{1 - \exp(-123\varepsilon)}{1.56 \times 10^{-6}}}$$

A5. Flow Behaviour of Bainite in DP600 Steel

$$\sigma_0 = 77 + 80(1.497) + 60(0.175) + 80(0.057) + 45(0.015) + 60(0.181) + 11(0.214) = 225.71 \text{ (MPa)}$$

$$\Delta\sigma_c^b = \Delta\sigma_c^f V_f + \Delta\sigma_c^m V_m = 30 \times 0.92 + 194.54 \times 0.047 = 36.74 \text{ (MPa)}$$

$$\sigma = 225.71 + 36.74 + 0.33 \times 3 \times 80000 \times \sqrt{2.5x10^{-10}} \times \sqrt{\frac{1 - \exp(-3 \times (10^{-5} / 2.56 \times 10^{-6}) \times \varepsilon)}{(10^{-5} / 2.56 \times 10^{-6}) \times (2.0 \times 10^{-7})}} =$$

$$= 262.45 + 1.25\sqrt{\frac{1 - \exp(-11.72\varepsilon)}{7.81 \times 10^{-7}}}$$

VITA AUCTORIS

NAME	Maedeh Amirmaleki
PLACE OF BIRTH	Esfahan, Iran
YEAR OF BIRTH	1986
EDUCATION	B.Sc. Materials Engineering: Ceramics Iran University of Science and Technology 2009 M.Sc. Materials Science and Engineering University of Kiel - Christian-Albrechts-Universität 2011 M.A.Sc. Mechanical Engineering University of Windsor 2014